HIGH-ORDER FINITE-DIFFERENCE METHODS FOR PHOTONIC DEVICES

HIGH-ORDER FINITE-DIFFERENCE METHODS FOR MODELING AND SIMULATION OF HIGH-INDEX-CONTRAST PHOTONIC INTEGRATED DEVICES

By

HUA ZHANG, B.ENG., M.Sc.

A Thesis

Submitted to the School of Graduate Studies

in Partial Fulfilment of the Requirements

for the Degree

Doctor of Philosophy

McMaster University

DOCTOR OF PHILOSOPHY (2007) McMaster University

(Electrical and Computer Engineering) Hamilton, Ontario

TITLE: High-Order Finite-Difference Methods for Modeling and Simulation of High-Index-Contrast Photonic Integrated Devices

AUTHOR: Hua Zhang

B.ENG., M.Sc. (Jilin University, China)

SUPERVISOR: Dr. Wei-Ping Huang

Professor, Department of Electrical and Computer Engineering

NUMBER OF PAGES: xiv, 181

Abstract

High index contrast optical waveguides have recently attracted much attention as a promising platform for ultradense photonic integrated circuits. The vector nature and fine geometry of such waveguiding structures impose new challenges for numerical modeling. By introducing the high-order finite-difference method, highly accurate and efficient modeling techniques have been developed in this thesis for simulation and design of high index contrast waveguiding structures with compact size.

High-order mode solving techniques are first presented for modal analyses. Their advantages in accuracy have been demonstrated for high index contrast optical waveguides and bent waveguides with small bending radius.

Later, a class of high-order propagation algorithms, including the paraxial and wide-angle beam propagation methods, reflective operator method and bidirectional beam propagation method, have been developed for modeling longitudinally slow-varying structures, single waveguide discontinuity and piecewise z-invariant structures, respectively. All the proposed propagation algorithms have been shown to provide significant improvement in accuracy and efficiency in comparison with conventional methods, especially when simulating high index contrast structures with small feature size.

Accurate modeling of evanescent waves is critical for the simulation of strongly reflecting structures with high longitudinal index contrast. Various rational approximations to square root operators used in the bidirectional beam propagation

method have been comprehensively assessed. Useful guidelines for accurate modeling of evanescent and propagating modes are provided.

Finally, the efficient high-order bidirectional beam propagation method is introduced for the design of Bragg gratings on high index contrast and plasmonic waveguides. Good performance is achieved.

Acknowledgements

I would like to express my sincere gratitude to my supervisor, Dr. Wei-Ping Huang, for his excellent guidance, and constant support and encouragement throughout the entire course of my Ph.D program. The doctoral training I received from him not only helped me establish creativity and rigorousness in scientific research, but also will benefit me in various aspects of my life.

I greatly appreciate Dr. Xun Li, Dr. Shiva Kumar and Dr. A. P. Knights, members of my supervisory committee, for their valuable advice and fruitful discussions in my study. I am also very grateful to Dr. Chenglin Xu and Dr. Ning-Ning Feng, my former colleagues, for their directions and inspiration in the early stages of my program.

I also thank my colleagues, Dr. Dong Zhou, Dr. Dimitri Labukhin, Yu Chen, Minhui Yan, Yanping Xi, Jianwei Mu, Lei Zhao and Qingyi Guo for their useful discussions in research and various assistances in daily life. I would like to thank Ms. Cheryl Gies, Ms. Helen Jachna, Mr. Terry Greenlay and Mr. Cosmin Coroiu for their administrative and technical support.

I would like to give special thanks to my wife, Ruixue Chen, for her love, support, encouragement and patience in everyday life. Last but not least, I would like to express most sincere gratitude to my parents and my sister for their love and lifelong care.

Contents

Abstract ..... **iii**

Acknowledgements ..... **v**

Contents ..... **vi**

List of Figures ..... **ix**

List of Tables ..... **xiv**

Chapter 1 Introduction **1**

1.1 Background of the Research 1

1.1.1 Computer-Aided Design (CAD) for Photonic Devices 2

1.1.2 Mode Solving Techniques 3

1.1.3 Modeling Techniques for Wave Propagation 5

1.2 Motivation of the Research 8

1.3 Outline of the Theses 10

Chapter 2 Fundamental Equations **12**

2.1 Introduction 12

2.2 Maxwell's Equations 13

2.3 Wave Equations 15

2.3.1 Wave Equation for Electric Field 16

2.3.2 Wave Equation for Magnetic Field 18

2.4 Boundary Conditions for Electromagnetic Fields 20

2.5 Summary 22

Chapter 3 Finite-Difference Methods **23**

3.1 Introduction 23

3.2 Derivations of Various FD Formulas 26

3.2.1 Central Difference Scheme 26

3.2.2 Scalar Fourth-Order FD Formula 29

3.2.3 Vectorial Fourth-Order FD Formula 30

3.2.4 Vectorial Second-Order FD Formula 34
3.3 Evaluations of Various FD Formulas 34
3.4 Summary 38
Chapter 4 High-Order Mode Solving Techniques 39
4.1 Introduction 39
4.2 One-Dimensional (1D) Wave Equation 41
4.3 Analytical Methods 44
4.3.1 Symmetric Three-Layer Slab Waveguides 44
4.3.2 Asymmetric Three-Layer Slab Waveguides 48
4.3.3 Thin Metal Film Embedded in Dielectric 52
4.4 Numerical Methods 53
4.4.1 Implementation 54
4.4.2 Numerical Results 58
4.5 High-Order Mode Solving Techniques for Bent Waveguides 60
4.5.1 Conformal Transformation Method 61
4.5.2 Numerical Results 62
4.6 Summary 69
Chapter 5 High-Order Finite-Difference Beam Propagation Method (BPM) 70
5.1 Introduction 70
5.2 One-Way Wave Equations 72
5.2.1 Paraxial Wave Equations 73
5.2.2 Wide-Angle Wave Equations 74
5.3 Numerical Examples 76
5.3.1 Radiation of Line Source 76
5.3.2 Step-Index Slab Waveguide with High Index Contrast 80
5.4 Summary 88
Chapter 6 High-Order Reflective Operator Method (ROM) 89
6.1 Introduction 89
6.2 Iterative Scheme for Reflection and Transmission Formulas 91

6.3 Numerical Results and Discussion 95
6.4 Summary 105
Chapter 7 High-Order Bidirectional Beam Propagation Method (BiBPM) 106
7.1 Introduction 106
7.2 Scattering Operator Formulation 111
7.3 Assessment of Various Rational Approximations 116
7.4 Assessment of High-Order BiBPM 128
7.5 Summary 139
Chapter 8 Design of Bragg Gratings on High Index Contrast and Surface Plasmonic Waveguides by High-Order BiBPM 141
8.1 Introduction 141
8.2 Design of Bragg Gratings with Strong Index Corrugations 144
8.2.1 Conventional Design Method 144
8.2.2 Iteration Method 147
8.3 Design of Bragg Grating on Surface Plasmonic Waveguides 151
8.3.1 Characteristics of LR-SPP Mode 151
8.3.2 Analysis of LR-SPP Based Bragg Gratings 153
8.4 Summary 157
Chapter 9 Conclusions and Suggestions for Future Research 158
9.1 Summary of Contributions 158
9.2 Suggestions for Future Research 160
Bibliography 162
Appendix A Coefficients Used in Finite-Difference Formulas 175
Appendix B Finite-Difference Form of One-Way Wave Equations 177
Appendix C Finite-Difference Form of Reflective Operator Scheme 179
Appendix D List of Publications 180

List of Figures

Figure 2.1 Discontinuity in a medium. 21
Figure 3.1 Schematics of three consecutive grid points 27
Figure 3.2 Schematics of grid points with discontinuities. 31
Figure 3.3 Relative error in the transverse wave number as a function of mesh size: without index discontinuity. Legends vectorial FD4, vectorial FD2, CD and scalar FD4 represent vectorial four-order FD formula, vectorial second-order FD formula, central difference scheme and scalar fourth-order FD formula, respectively. 37
Figure 3.4 Relative error in the transverse wave number as a function of mesh size: with index discontinuity. The legend is the same with Figure 3.3 37
Figure 4.1 Schematics of one-dimensional waveguide 42
Figure 4.2 Schematics of symmetric three-layer slab waveguide 45
Figure 4.3 Schematics of asymmetric three-layer slab waveguide. 49
Figure 4.4 Schematics of thin metal film embedded in dielectric. 52
Figure 4.5 Uniform discretization for the FDM 55
Figure 4.6 General form of tridiagonal matrix 55
Figure 4.7 Relative error in the propagation constant as a function of mesh size. (a) TE; (b) TM. "conventional FD" represents the conventional central difference scheme and "4th FD" represents the vectorial fourth-order FD formula. 59
Figure 4.8 Relative L2-norm errors of the calculated fields as a function of mesh size. (a) TE; (b) TM. "conventional FD" represents the conventional central difference scheme and "4th FD" represents the vectorial fourth-order FD formula 60
Figure 4.9 (a) A waveguide bend with step-index distribution; (b) its transformation. 61

Figure 4.10 Single mode condition for symmetric slab waveguides. n-av. represents $\bar{n}$ 63

Figure 4.11 Minimum bending radius and maximum core width as a function of refractive index contrast for $\bar{n} = 1.0$, 2.0, and 3.0. (a) TE; (b) TM..... 65

Figure 4.12 Confinement factor and minimum bending radius as a function of refractive index contrast for $\bar{n} = 1.0$, 2.0, and 3.0. (a) TE; (b) TM..... 67

Figure 4.13 Polarization effects as a function of refractive index contrast for $\bar{n} = 1.0$, 2.0, and 3.0. 68

Figure 5.1 Field distributions of the radiation from a line source obtained by the paraxial BPM. (a) CD in coarse mesh; (b) FD4 in coarse mesh; (c) CD in fine mesh; (d) FD4 in fine mesh. Coarse mesh $\Delta x = 0.4$ μm, fine mesh: $\Delta x = 0.05$ μm, and longitudinal step-size: $\Delta z = 0.05$ μm..... 78

Figure 5.2 Field distributions of line source obtained by Padé (11,11) wide-angle BPM. (a) CD in coarse mesh; (b) FD4 in coarse mesh; (c) CD in fine mesh; (d) FD4 in fine mesh. The other parameters are the same as in Figure 5.1. 79

Figure 5.3 The comparison of CD and FD4 for coarse and fine meshes, respectively. (a) The relative error for the intensity; (b) The relative error for the phase. 80

Figure 5.4 Effect of the variation in the reference index on the relative error of the propagation constant. (a) TE mode; (b) TM mode. 83

Figure 5.5 Relative error in the propagation constant as a function of the transverse step size (a) TE mode; (b) TM mode. 84

Figure 5.6 Relative error in the propagation constant as a function of the transverse step size for quasi-FD4 and true FD4. (a) TE mode; (b) TM mode..... 85

Figure 5.7 The mode-mismatch loss as a function of relative refractive index difference for quasi-FD4 and true FD4. (a) TE mode; (b) TM mode..... 87

Figure 6.1 Schematic diagrams of waveguide facet (a) and partially etched waveguide (b)..... 96

Figure 6.2 Variation of the power reflectivity with the Padé order using the CD and FD4 formulas for a waveguide facet. 97
Figure 6.3 Power reflectivity as a function of mesh size Δx with CD and FD4 formulas for a waveguide facet. (a) TE mode; (b) TM mode. 99
Figure 6.4 Power reflectivity as a function of refractive index contrast Δ with CD and FD4 formulas for a waveguide facet. 101
Figure 6.5 Power reflectivity versus core width d with CD and FD4 formulas for a waveguide facet. (a) TE mode; (b) TM mode. 103
Figure 6.6 Power reflectivity versus etching depth h using CD and FD4 formulas with coarse and fine meshes, respectively, for a partially etched waveguide. (a) TE mode; (b) TM mode 104
Figure 7.1 Schematic structure for assessment. 116
Figure 7.2 Relative L2-norm errors of the calculated fields obtained from different Padé approximations to the propagation operator. The transition operator is approximated by rotated branch cut Padé (8, 8) with $\alpha = \pi/2$ in all simulations. (a) TE; (b) TM. 119
Figure 7.3 Relative L2-norm errors of the calculated fields obtained from complex coefficient Padé (8, 8) approximations with different β. (a) TE; (b) TM. 121
Figure 7.4 Relative L2-norm errors of the calculated fields obtained from rotated branch cut Padé (8, 8) approximations with different rotation angles α. (a) TE; (b) TM. 122
Figure 7.5 Relative L2-norm errors of the calculated fields obtained from various Padé-type approximations. (a) reflected field for TE; (b) transmitted field for TE; (c) reflected field for TM; (d) transmitted field for TM. 125
Figure 7.6 Field patterns obtained from various Padé-type approximations. (a) the reflected field for TE; (b) the transmitted field for TE; (c) the reflected field for TM; (d) the transmitted field for TM. "Complex Padé" and "MMM" represent complex coefficient Padé and the mode matching

method, respectively. The Padé order (6, 6) is employed in all calculations. The field patterns obtained from the complex coefficient Padé with rotated branch cut coincide with that of the rotated branch cut Padé and are omitted here. 126
Figure 7.7 Relative L2-norm errors of transmitted fields obtained from various Padé-type approximations for different longitudinal index contrasts. (a) TE; (b) TM. 128
Figure 7.8 Schematic diagram of 1D photonic crystal slab waveguide (PCSW). 129
Figure 7.9 Transmission of the fundamental TE mode calculated by FD2- and FD4-BiBPMs employing different mesh sizes. (a) $\Delta x = 0.025$ μm; (b) $\Delta x = 0.0625$ μm; (c) $\Delta x = 0.125$ μm. 132
Figure 7.10 Central wavelengths calculated by FD2 and FD4 methods for TE as a function of mesh size. 133
Figure 7.11 Total electric field distribution through the 1D PCS structure at central wavelength 1.544 μm. (a) FD2 with $\Delta x = 0.125$ μm; (b) FD4 with $\Delta x = 0.125$ μm; (c) FD4 with $\Delta x = 0.025$ μm. The horizontal and vertical white lines indicate cladding-core interfaces and edges of the middle defect, respectively. The color bar is the same for all the plots. 134
Figure 7.12 Reflection of the fundamental TM mode calculated by FD2- and FD4-BiBPMs employing different mesh sizes. (a) $\Delta x = 0.025$ μm; (b) $\Delta x = 0.0625$ μm and MMM using the same mesh size; (c) $\Delta x = 0.125$ μm and MMM using the same mesh size. 138
Figure 7.13 Central wavelengths calculated by FD2 and FD4 methods for TM as a function of mesh size. 139
Figure 8.1 A typical Bragg grating structure consisting of two-element unit cells. 144
Figure 8.2 Reflection and transmission spectra of the fundamental TE mode. 146
Figure 8.3 A flow chart for the iteration method in design of deep gratings. 147
Figure 8.4 Reflection and transmission spectra of the fundamental TE mode. 149
Figure 8.5 Schematic diagram of 1D photonic crystal slab waveguide. 149

Figure 8.6 Reflection and transmission spectra of the fundamental TM mode. (a) iteration 1; (b) iteration 2; (c) iteration 3; (d) iteration 4. 150
Figure 8.7 Schematic diagram of thin metal film embedded in dielectric. 151
Figure 8.8 Complex effective index of the LR-SPP mode as a function of film thickness for symmetric structure with $n_1 = n_3 = 1.543$ and $n_M = 0.55 - 11.5j$ at wavelength of 1.55 μm. (a) real part; (b) imaginary part 152
Figure 8.9 Field distributions of the LR-SPP mode supported by the gold film with $d = 15$ nm and $d = 60$ nm. 153
Figure 8.10 Schematic diagram of Bragg grating based on LR-SPP 154
Figure 8.11 Reflection and transmission spectra of the LR-SPP grating. (a) $N = 160$; (b) $N = 256$ 155
Figure 8.12 Field distributions through the first ten periods for the grating with ridge height $h = 10$ nm and $N = 160$ periods. (a) $\lambda = 1.53$ μm; (b) $\lambda = 1.545$ μm; (c) $\lambda = 1.57$ μm. The color bar is the same for all the plots. 157

List of Tables

Table 3.1 Values of θ 32
Table 6.1 Grid points for TE. 100
Table 6.2 Grid points for TM. 100
Table 7.1 Comparison of the computational cost for FD2- and FD4- BiBPM. 135

Chapter 1
Introduction

1.1 Background of the Research

Fiber-optic communication systems built from optical fibers and a variety of optical components have dominated long-haul communication networks in the last two decades of the twentieth century. In recent years, the demand for increasing transmission bandwidth at lower cost is growing rapidly, mainly due to the widespread use of the Internet. The broadband network requires the development of advanced optical components which are the foundations of fiber-optic communication systems. Integrated optical devices based on planar lightwave circuits provide a good solution to meet the ever-increasing bandwidth requirements.

The term "integrated photonics" was proposed as early as in 1969 by S. E. Miller [1], which refers to the fabrication and integration of multiple photonic components on a single substrate. These components usually include light sources, beam splitters, gratings, couplers, polarizers, detectors, etc. All of these components are combined and interconnected by small transmission lines called optical waveguides, creating integrated photonic circuits. Integrated photonic circuits can not only meet the high performance required by broadband optical systems but also allow the miniaturisation of optical systems. Moreover, the integration of multiple functions on a single chip leads to cost

reduction which is extremely significant for both manufactures and consumers. Therefore, integrated photonics has been a promising technology for of the entire fiber-optic communication network.

1.1.1 Computer-Aided Design (CAD) for Photonic Devices

It is widely recognized that the major contributors to the advances of integrated photonics have been the development of new device concepts and the tremendous improvement of the fabrication and processing technologies. It should be noted, however, that the computer-aided design (CAD) has been playing a critical role in the advancement of novel integrated optical devices. The significance of photonics CAD lies in its ability to lower product development costs and to greatly shorten design cycle. Specifically, photonics CAD tools manifest their role in the evaluation of new device concepts and optimization of current designs.

The widespread use of commercialized photonics CAD tools in the design of optical devices relies on the availability of modeling techniques and powerful personal computers. Exploring for novel theoretical approaches for modeling optical devices has been constantly attracting much attention in the area of integrated photonics. All of the developed theoretical approaches can be classified into analytical, semi-analytical and numerical methods. Analytical methods provide exact solutions but are severely restricted in a few simple structures such as slab or circularly symmetric step-index waveguides, limiting their use in the analysis of complex structures. Consequently, in practice, more attention has been paid on semi-analytical and numerical methods. Semi-analytical

methods typically involve much physical concepts and mathematical derivations in which approximation is often made by taking advantage of the feature of structures. The competitive advantage of semi-analytical methods is the high efficiency in terms of computational time and memory requirements, because they avoid to directly solve the full-wave equations. In contrast, numerical methods usually solve directly Maxwell's equations or reduced vectorial or scalar wave equations and thus are more numerically intensive. In turn, numerical methods are conceptually simpler and less problem dependent, which are preferred by general designers.

The family of photonics CAD tools can facilitate different stages of the entire optical system design. They can simulate and optimize factors such as the bending loss of optical waveguides, the spectral bandwidth of waveguide gratings, and the performance of complex optical networks. Since optical waveguides are the key element of integrated photonic circuits that perform not only guiding, but also coupling, switching and splitting optical signals, the design of various optical waveguides using CAD tools is the fundamental step necessary for the optical system design. The design of optical waveguides involves two main issues: mode solving techniques for the waveguide cross section and modeling techniques for lightwave propagation in longitudinally varying waveguides. These two issues will be briefly discussed in the following sections.

1.1.2 Mode Solving Techniques

Optical modes are defined as the solutions to the eigenvalue problems for longitudinally-invariant waveguides. Mode solving is the basis for analysis and design of

optical waveguides. The task of modal analysis is to determine the propagation constant and the corresponding mode profile for a given waveguide cross-section and a fixed wavelength. Mode solving techniques could be analytical, semi-analytical or numerical, depending on the geometry of cross-section and the requirement for accuracy. In analytical methods, the propagation constant for a particular guide section is first obtained by solving the transcendental equation, and then the mode profile can be found by substituting the propagation constant to the field expression in an analytical form. Analytical solutions of waveguide modes are only available in a few simple structures. The semi-analytical methods such as effective index method [2][3], spectral index method [4][5] and variational method [6][7] are usually efficient, but they may not be accurate enough for more complex waveguide structures. In this respect, numerical methods are highly desired for solving the modes of most practical waveguides.

Numerical methods directly solve the wave equation derived from Maxwell's equations. According to the form of wave equations, numerical mode solvers can be classified into scalar, semi-vectorial and full-vectorial solvers. Scalar wave equations are exact in a uniform region of space; semi-vectorial and full-vectorial formulations are more accurate for waveguide structures with transverse piecewise constant refractive index profiles. In comparison with semi-vectorial ones, full-vectorial formulations consider the coupling effect between two components of the fields. The second-order wave equation is then discretized, resulting in an eigenvalue matrix equation. One of the most popular discretization methods is the finite-difference method (FDM) which utilizes the rectangular discretization grid [8][9]. The resulting eigenvalue problem can be solved

by iterative solvers or sparse matrix routines to obtain the propagation constants (eigenvalues) and the corresponding mode profiles (eigenvectors).

1.1.3 Modeling Techniques for Wave Propagation

Modal analysis only provides information to straight waveguides with uniform cross section. In practice, more general wave-guiding structures involve optical waveguides that are non-uniform along the propagation direction, such as bending waveguides, *Y*-branch waveguides and waveguide gratings. Modeling techniques for handling the lightwave propagation in those longitudinally varying structures are more important for the design of photonic devices. The available propagation techniques range from approximate analytical or semi-analytical methods, such as the coupled-mode theory (CMT) [10][11] and the mode-matching method (MMM) [12], to numerical approaches, such as the beam propagation method (BPM) [13][14], the method of lines (MoL) [15][16] and the finite-difference time-domain method (FDTD) [17]-[21].

Among these techniques, the BPM is one of the most popular methods for simulation of wave propagation in optical waveguides and photonic integrated circuits, and is widely used in commercial photonic CAD software. The popularity of BPM is mainly attributed to its conceptual simplicity which allows the rapid implementation of the basic technique and the easy usage of the software for a nonexpert in numerical methods. Additionally, in comparison with other numerical techniques such as the FDTD method, the BPM is much more efficient and yet offers a good accuracy for most practical structures. Another attractive feature of the BPM is that both the guided and the

radiative waves are included in the analysis. As long as the incident field is given, the BPM is capable of tracing the wave propagation in the given structure.

Since 1978, when Feit and Fleck [13] first introduced the BPM into fiber optics to calculate the mode properties of optical fibers, various kinds of BPM techniques [22]-[34] have been proposed to extend the range of its application and to include more complex physical effects in the analysis. The accuracy, efficiency and stability of various BPMs have been greatly improved with the development of advanced numerical algorithms. The evolution of BPM techniques is briefly reviewed as follows.

Paraxial BPM. For slowly varying guided-wave structures, the electromagnetic field propagates primarily along the guiding axis (z). The fast-oscillating phase term can be factored out of the field, leading to a so-called slowly varying field. The variation of the slowly varying field with z is sufficiently slow so that the second-order derivative with respect to z in the Helmholtz equation can be neglected. Thus, the boundary value problem has been reformulated as initial value problems which can be solved much more efficiently. However, the slowly varying envelope approximation limits consideration to paraxial propagation and imposes restrictions on the longitudinal index contrast.

Wide-angle BPM. The limitations of the paraxial BPM can be removed by introducing the wide-angle BPM. The key idea is to incorporate the second-order derivative with respect to z which is neglected in the paraxial BPM into the Helmholtz equation. Ignoring the backward field yields the one-way Helmholtz equation involving the square root of the differential operator. Different approaches have been developed to evaluate this square root operator. The most popular method is the multistep Padé-based

wide-angle technique [31]. The wide-angle BPM is able to accurately model the waves propagating at large angles with the waveguide axis. Furthermore, the dependence on the proper choice of the reference refractive index which is required in the paraxial algorithm can be alleviated to some extent. Nevertheless, the wide-angle BPM cannot handle the abrupt discontinuities along the waveguide axis due to ignoring the backward propagating fields.

Reflective operator method. The conventional BPM deals with one-way propagation only and thus is not capable of simulating reflection from waveguide discontinuities. The reflective operator method includes both the backward and forward fields in the formulation and can give accurate predictions for power reflection and transmission. Two important numerical techniques needed for this method are the evaluation of the square root operator and the solution algorithm for the linear system derived from the reflection and transmission formulas.

Bi-directional BPM (BiBPM). As an extension of the reflective operator method which deals with single waveguide discontinuity, the BiBPM aims at simulating structures with multiple discontinuity interfaces. Several BiBPMs [35]-[41] have been proposed to improve the accuracy and stability. All the bi-directional algorithms can be classified into two categories: iterative and noniterative methods. The iterative method propagates the field back and forth many times until a convergence is reached, and the noniterative method involves direct manipulations of operators. No matter what method is used, the complex representation of the square root operator is required for accurate modeling of evanescent and propagating waves.

1.2 Motivation of the Research

Various BPM techniques rely on a discretization scheme to convert differential wave equations to standard matrix equations that can be solved with an appropriate matrix solution algorithm. Such discretization schemes include the finite-difference method (FDM) and the finite-element method (FEM) [42][43]. The FDM is the primary interest of this thesis because of its relative ease of mesh generation. Although the FEM is more versatile to accommodate irregular geometries, the rectangular shape characterized by most integrated optical devices leads to the widespread usage of the FDM in the photonic CAD. On the other hand, the FDM lends itself easily to Taylor series analysis of truncation errors by virtue of which more advanced high-order schemes can be developed.

Finite difference methods have been long used to approximate the solution of ordinary or partial differential equations. These methods involve discretizing the domain of interest into a structured mesh of grid points and approximating derivatives by differencing schemes. At each grid point, the values of the desired function are treated as unknowns, and the governing differential equation is approximated by a sparse system of algebraic equations. The efficiency and accuracy of the FDM are highly dependent on its finite-difference formulas.

Most of the conventional finite-difference based BPM techniques employ the well-known central difference scheme which is derived from the scalar approximation and is second-order accurate for homogeneous medium [44]. In the modeling of

structures with graded index or low index contrast, an improved FD formula [8] roughly considering the transverse index discontinuity is widely used in various BPM techniques. Both of the above mentioned FD formulas are derived by assuming that the second derivatives are continuous. This approximation is no longer valid for step-index structures with high index contrast [45]-[48], and therefore the accuracy of these FD formulas are severely decreased. One plausible solution is to use finer discretization. However, finer discretizations demand larger memory and longer computational time. The increase in the computational effort becomes more significant for nanostructures where the guiding layer is typically in nanometer scale, because a very fine mesh is needed in order to capture the detailed feature of those structures. Consequently, mesh refinement is not an efficient solution to accurate modeling of step-index structures and sometimes is not even possible. Thus, it is highly desirable to employ a class of high-order FD formulas that are both accurate and efficient in the beam propagation analysis.

High-order FD formulas can be derived by the rigorous treatment of dielectric interface conditions between different refractive indexes and by inclusion of additional high-order terms in the Taylor series expansion to second-order differential derivatives. Several high-order FD formulas have been developed for optical waveguides mode solving techniques [49]-[53]. It is noted, however, that propagation techniques based on high-order FD schemes have received less attention in literature. Since most practical photonic devices involve propagation in longitudinally varying structures, propagation solvers that allow designers to simulate light passage through any waveguide path both accurately and efficiently are highly desirable. Aiming at this goal, this thesis is devoted

to developing various high-order BPM techniques with special emphasis on the simulation and design of high index contrast waveguides.

1.3 Outline of the Theses

This thesis is organized as follows.

Chapter 1 starts with the introduction to the necessity of photonic CAD. A brief review of various modeling techniques for optical waveguide devices is then presented, with a particular emphasis on beam propagation method techniques. Finally, the motivation of this thesis is outlined aimed at addressing the new challenges in numerical modeling of optical waveguide devices.

In chapter 2, vectorial wave equations and boundary conditions are derived from the Maxwell's equations for fully describing the light wave propagation in optical waveguides. Other governing equations that will be used in the following chapters can be further derived by applying certain approximations.

Chapter 3 first describes the basic idea of the finite-difference method. A comprehensive review of various frequently used FD formulas and their derivations are then presented. The accuracy of these FD formulas is comparatively evaluated by an analytical method.

In chapter 4, high-order mode solving techniques are developed for both the dielectric waveguides and plasmonic waveguides. The characteristics of bent waveguides with high index contrast are also investigated by the high-order mode solver.

Chapter 5 is devoted to the development of high-order one-way beam propagation methods. The vectorial fourth-order FD formula is introduced to both the paraxial and wide-angle algorithms to efficiently simulate wave propagation in longitudinally slow-varying structures.

Chapter 6 focuses on the analysis of waveguide discontinuity problem. A high-order reflective operator scheme is developed in order to accurately and efficiently analyze waveguide discontinuities

Chapter 7 is concerned with the numerical techniques for modeling of wave propagation in piecewise z-invariant structures. A stable high-order bidirectional beam propagation method is developed to improve the efficiency of the scattering operator formulation which is more dependent on the number of grid points. With the help of the new method, guidelines for accurately modeling of evanescent and propagating modes in strongly reflective structures are provided.

As the applications of the high-order bidirectional beam propagation method, the design of Bragg gratings on high index contrast and surface plasmonic waveguides is presented in chapter 8.

Chapter 9 summarizes the major contributions made in this thesis and lists suggestions for future work.

Chapter 2
Fundamental Equations

2.1 Introduction

This thesis focuses on the study of the propagation of electromagnetic waves in optical waveguides. Since the dimension of optical waveguides is comparable to the wavelength of the optical wave used in integrated photonic devices, the well-known ray optics approach is not sufficient for fully describing the performance of these devices. The light must be treated as electromagnetic waves. Therefore, the electromagnetic theory of light is necessary to properly describe the behaviour of optical waveguides. In this chapter, we first introduce the rigorous Maxwell's equations which can describe the propagation of electromagnetic waves in any medium. Considering the fact that most optical waveguides are composed of source-free, linear, isotropic, non-conductive and non-magnetic medium, a set of simplified Maxwell's equations are derived based on some assumptions.

For time-harmonic waves, the rigorous vectorial wave equations for both electric fields and magnetic fields are derived starting from Maxwell's equations. For longitudinally invariant or slowly varying structures, the transverse components of the electric or magnetic fields are sufficient to describe the propagation of lightwave. Thus, we derive the vectorial wave equations in terms of transverse components. The modal

equations and one-way wave equations can be further derived from the vectorial wave equations by applying appropriate assumptions. The boundary conditions for electromagnetic fields are also presented in this chapter. For structures involving longitudinal abrupt discontinuities, reflection and transmission formulas can be derived from wave equations in conjunction with boundary conditions. Therefore, wave equations and boundary conditions for electromagnetic fields form the foundation of this thesis.

2.2 Maxwell's Equations

Optical fields are time-dependent fields and their behaviour is fully described by the set of Maxwell's equations. The Maxwell's equations in their differential form are given as

$$\nabla \times \vec{E} = -\frac{\partial \vec{B}}{\partial t} \tag{2.1}$$

$$\nabla \times \vec{H} = \frac{\partial \vec{D}}{\partial t} + \vec{J} \tag{2.2}$$

$$\nabla \cdot \vec{D} = \rho \tag{2.3}$$

$$\nabla \cdot \vec{B} = 0 \tag{2.4}$$

where $\vec{E}$ is the electric field, $\vec{H}$ is the magnetic field, $\vec{B}$ is the magnetic flux density, $\vec{D}$ is the electric flux density, $\vec{J}$ is the electrical current density, ρ is the volume charge density and t is the time.

For a source-free, linear, isotropic, non-conductive and non-magnetic medium, we have

$$\vec{J} = 0 \tag{2.5}$$

$$\rho = 0 \tag{2.6}$$

$$\vec{D} = \varepsilon \vec{E} \tag{2.7}$$

$$\vec{B} = \mu \vec{H} \tag{2.8}$$

where the permittivity ε and the permeability μ describe the electromagnetic properties of the medium and are defined as

$$\varepsilon = \varepsilon_0 \varepsilon_r \tag{2.9}$$

$$\mu = \mu_0 \mu_r \,. \tag{2.10}$$

Here, ε_0 and μ_0 are the permittivity and permeability of a vacuum, respectively, ε_r and μ_r are the relative permittivity and permeability of the material, respectively. Since only non-magnetic materials are considered, it is assumed $\mu_r = 1$ throughout this thesis. When analysing the optical properties of a material, the refractive index n, which is defined as $n = \sqrt{\mu_r \varepsilon_r}$, is frequently used throughout this thesis.

Considering Eqs. (2.5) - (2.10), the Maxwell's equations are rewritten as

$$\nabla \times \vec{E} = -\mu_0 \frac{\partial \vec{H}}{\partial t} \tag{2.11}$$

$$\nabla \times \vec{H} = n^2 \varepsilon_0 \frac{\partial \vec{E}}{\partial t} \tag{2.12}$$

$$\nabla \cdot (n^2 \vec{E}) = 0 \tag{2.13}$$

$$\nabla \cdot \vec{H} = 0 \tag{2.14}$$

2.3 Wave Equations

The wave equation is a second-order partial differential equation that describes the propagation of the electromagnetic fields. The wave equation is derived from the Maxwell's equations by assuming that the fields oscillate at a single angular frequency ω, expressed as

$$\vec{A}(r,t) = \mathrm{Re}\{A(r)\exp(j\omega t)\} \tag{2.15}$$

where the vector $\vec{A}$ designates the electromagnetic fields. Using this form, we can write the following phasor expressions for the electric field $\vec{E}$, the magnetic field $\vec{H}$, the magnetic flux density $\vec{B}$ and the electric flux density $\vec{D}$

$$\vec{E}(r,t) = \mathrm{Re}\{E(r)\exp(j\omega t)\} \tag{2.16}$$

$$\vec{H}(r,t) = \mathrm{Re}\{H(r)\exp(j\omega t)\} \tag{2.17}$$

$$\vec{B}(r,t) = \mathrm{Re}\{B(r)\exp(j\omega t)\} \tag{2.18}$$

$$\vec{D}(r,t) = \mathrm{Re}\{D(r)\exp(j\omega t)\} \tag{2.19}$$

where the complex vectors E, H, B and D represent the amplitudes of the time-varying vectors. Substituting Eqs. (2.16) - (2.19) into Eqs. (2.11) - (2.14) gives

$$\nabla \times E = -j\omega\mu_0 H \tag{2.20}$$

$$\nabla \times H = j\omega n^2 \varepsilon_0 E \tag{2.21}$$

$$\nabla \cdot (n^2 E) = 0 \tag{2.22}$$

$$\nabla \cdot H = 0 \tag{2.23}$$

2.3.1 Wave Equation for Electric Field

The full-vectorial wave equation based on electric fields can be derived from Maxwell's equations. By taking the curl of Eq. (2.20) and using Eq. (2.21), we have

$$\nabla \times (\nabla \times E) = k_0^2 n^2 E \tag{2.24}$$

where $k_0 = \dfrac{\omega}{c_0}$ is the wave number of free space and $c_0 = \dfrac{1}{\sqrt{\mu_0 \varepsilon_0}}$ is the velocity of light in free space. By using the vector identity

$$\nabla \times \nabla \times = \nabla(\nabla \cdot) - \nabla^2 \tag{2.25}$$

Eq. (2.24) becomes

$$\nabla(\nabla \cdot E) - \nabla^2 E = k_0^2 n^2 E . \tag{2.26}$$

The symbol ∇^2 is a Laplacian defined as

$$\nabla^2 = \frac{\partial^2}{\partial x^2} + \frac{\partial^2}{\partial y^2} + \frac{\partial^2}{\partial z^2} . \tag{2.27}$$

Since Eq. (2.22) can be rewritten as

$$\nabla \cdot (n^2 E) = \nabla n^2 \cdot E + n^2 \nabla \cdot E \tag{2.28}$$

we obtain

$$\nabla \cdot E = -\frac{\nabla n^2}{n^2} \cdot E . \tag{2.29}$$

By substituting Eq. (2.29) into Eq. (2.26), the vectorial wave equation for the electric field E is obtained as

$$\nabla^2 E + \nabla\left(\frac{\nabla n^2}{n^2}\cdot E\right) + k_0^2 n^2 E = 0. \tag{2.30}$$

Further simplification can be introduced by assuming that waveguides are z-invariant i.e., $\frac{\partial n^2}{\partial z} = 0$, which is the case in most practical structures. In this case, the total field can be expressed in terms of transverse components of electric field or magnetic field. The longitudinal component may be readily obtained by using the zero divergence constraint Eqs. (2.22) and (2.23).

By making use of $\frac{\partial n^2}{\partial z} = 0$, the second term in Eq. (2.30) can be written as

$$\nabla\left(\frac{\nabla n^2}{n^2}\cdot E\right) = \nabla\left(\frac{1}{n^2}\frac{\partial n^2}{\partial x}E_x + \frac{1}{n^2}\frac{\partial n^2}{\partial y}E_y\right). \tag{2.31}$$

After substituting Eq. (2.31) into Eq. (2.30) and decomposing Eq. (2.30) into the x and y components, we obtain the vectorial wave equation in terms of transverse electric fields.

$$\frac{\partial^2 E_x}{\partial x^2} + \frac{\partial}{\partial x}\left(\frac{1}{n^2}\frac{\partial n^2}{\partial x}E_x\right) + \frac{\partial^2 E_x}{\partial y^2} + \frac{\partial^2 E_x}{\partial z^2} + k_o^2 n^2 E_x + \frac{\partial}{\partial x}\left(\frac{1}{n^2}\frac{\partial n^2}{\partial y}E_y\right) = 0 \tag{2.32}$$

$$\frac{\partial^2 E_y}{\partial x^2} + \frac{\partial^2 E_y}{\partial y^2} + \frac{\partial}{\partial y}\left(\frac{1}{n^2}\frac{\partial n^2}{\partial y}E_y\right) + \frac{\partial^2 E_y}{\partial z^2} + k_o^2 n^2 E_y + \frac{\partial}{\partial y}\left(\frac{1}{n^2}\frac{\partial n^2}{\partial x}E_x\right) = 0. \tag{2.33}$$

Because of

$$\frac{\partial}{\partial x}\left[\frac{1}{n^2}\frac{\partial}{\partial x}\left(n^2 E_x\right)\right] = \frac{\partial^2 E_x}{\partial x^2} + \frac{\partial}{\partial x}\left(\frac{1}{n^2}\frac{\partial n^2}{\partial x}E_x\right) \tag{2.34}$$

and

$$\frac{\partial}{\partial y}\left[\frac{1}{n^2}\frac{\partial}{\partial y}\left(n^2E_y\right)\right]=\frac{\partial^2E_y}{\partial y^2}+\frac{\partial}{\partial y}\left(\frac{1}{n^2}\frac{\partial n^2}{\partial y}E_y\right), \tag{2.35}$$

Eqs. (2.32) and (2.33) can be rewritten as

$$\frac{\partial}{\partial x}\left[\frac{1}{n^2}\frac{\partial}{\partial x}\left(n^2E_x\right)\right]+\frac{\partial^2E_x}{\partial y^2}+\frac{\partial^2E_x}{\partial z^2}+k_o^2n^2E_x+\frac{\partial}{\partial x}\left(\frac{1}{n^2}\frac{\partial n^2}{\partial y}E_y\right)=0 \tag{2.36}$$

$$\frac{\partial^2E_y}{\partial x^2}+\frac{\partial}{\partial y}\left[\frac{1}{n^2}\frac{\partial}{\partial y}\left(n^2E_y\right)\right]+\frac{\partial^2E_y}{\partial z^2}+k_o^2n^2E_y+\frac{\partial}{\partial y}\left(\frac{1}{n^2}\frac{\partial n^2}{\partial x}E_x\right)=0. \tag{2.37}$$

For a two-dimensional (2D) structure, we assume that the waveguide is infinite in the y direction and the confinement is along the x direction. The refractive index n and the electric fields supported by the structure are therefore independent of y. Thus, we obtain the Helmholtz equation for the transverse electric (TE) polarization

$$\frac{\partial^2E_y}{\partial z^2}+\frac{\partial^2E_y}{\partial x^2}+k_0^2n^2E_y=0. \tag{2.38}$$

2.3.2 Wave Equation for Magnetic Field

By taking the curl of Eq. (2.21), we have

$$\nabla\times\left(\nabla\times H\right)=j\omega\varepsilon_0\nabla\times\left(n^2E\right). \tag{2.39}$$

By using the vector identity and Eq. (2.20), Eq. (2.39) becomes

$$\nabla\left(\nabla\cdot H\right)-\nabla^2H=j\omega\varepsilon_0\left(\nabla n^2\times E+n^2\nabla\times E\right)=j\omega\varepsilon_0\left(\nabla n^2\times E\right)+k_0^2n^2H. \tag{2.40}$$

From Eq. (2.21), we have

$$E = \frac{1}{j\omega\varepsilon_0 n^2}\nabla\times H\,. \tag{2.41}$$

Substituting Eqs. (2.23) and (2.41) into Eq. (2.40), we obtain the vectorial wave equation for the magnetic field H

$$\nabla^2 H + \frac{\nabla n^2}{n^2}\times(\nabla\times H) + k_0^2 n^2 H = 0\,. \tag{2.42}$$

The vectorial wave equation in terms of transverse magnetic fields can be obtained in a way similar to the electric fields. By using the cross product of the gradient operator with a vector, the second term in the Eq. (2.42) can be expanded as

$$\begin{aligned}\nabla n^2\times(\nabla\times H) &= \begin{vmatrix} \vec{i} & \vec{j} & \vec{k} \\ \dfrac{\partial n^2}{\partial x} & \dfrac{\partial n^2}{\partial y} & 0 \\ (\nabla\times H)_x & (\nabla\times H)_y & (\nabla\times H)_z \end{vmatrix} \\ &= \frac{\partial n^2}{\partial y}(\nabla\times H)_z\,\vec{i} - \frac{\partial n^2}{\partial x}(\nabla\times H)_z\,\vec{j} + \left[\frac{\partial n^2}{\partial x}(\nabla\times H)_y + \frac{\partial n^2}{\partial y}(\nabla\times H)_x\right]\vec{k}\end{aligned} \tag{2.43}$$

by assuming $\dfrac{\partial n^2}{\partial z} = 0$. The definition of the curl in Cartesian coordinates gives

$$(\nabla\times H)_x = \frac{\partial H_z}{\partial y} - \frac{\partial H_y}{\partial z} \tag{2.44}$$

$$(\nabla\times H)_y = \frac{\partial H_x}{\partial z} - \frac{\partial H_z}{\partial x} \tag{2.45}$$

$$(\nabla\times H)_z = \frac{\partial H_y}{\partial x} - \frac{\partial H_x}{\partial y}\,. \tag{2.46}$$

Thus, Eq. (2.43) can be rewritten as

$$\nabla n^2 \times (\nabla \times H) = \frac{\partial n^2}{\partial y}\left(\frac{\partial H_y}{\partial x} - \frac{\partial H_x}{\partial y}\right)\vec{i} - \frac{\partial n^2}{\partial x}\left(\frac{\partial H_y}{\partial x} - \frac{\partial H_x}{\partial y}\right)\vec{j} + \left[\frac{\partial n^2}{\partial x}\left(\frac{\partial H_x}{\partial z} - \frac{\partial H_z}{\partial x}\right) + \frac{\partial n^2}{\partial y}\left(\frac{\partial H_z}{\partial y} - \frac{\partial H_y}{\partial z}\right)\right]\vec{k} \quad (2.47)$$

Substituting Eq. (2.47) into Eq. (2.42) and decomposing the result into the x and y components, we obtain the vectorial wave equation in terms of transverse magnetic fields

$$\frac{\partial^2 H_x}{\partial x^2} + n^2 \frac{\partial}{\partial y}\left(\frac{1}{n^2}\frac{\partial H_x}{\partial y}\right) + \frac{\partial^2 H_x}{\partial z^2} + k_o^2 n^2 H_x + \frac{1}{n^2}\frac{\partial n^2}{\partial y}\frac{\partial H_y}{\partial x} = 0 \quad (2.48)$$

$$n^2 \frac{\partial}{\partial x}\left(\frac{1}{n^2}\frac{\partial H_y}{\partial x}\right) + \frac{\partial^2 H_y}{\partial y^2} + \frac{\partial^2 H_y}{\partial z^2} + k_o^2 n^2 H_y + \frac{1}{n^2}\frac{\partial n^2}{\partial x}\frac{\partial H_x}{\partial y} = 0 \quad (2.49)$$

For a 2D structure, we obtain the Helmholtz equation for the transverse magnetic (TM) polarization

$$\frac{\partial^2 H_y}{\partial z^2} + n^2 \frac{\partial}{\partial x}\left(\frac{1}{n^2}\frac{\partial H_y}{\partial x}\right) + k_o^2 n^2 H_y = 0 \quad (2.50)$$

2.4 Boundary Conditions for Electromagnetic Fields

The Maxwell's equations (2.1) – (2.4) do not determine the electromagnetic fields completely. In the cases where there are discontinuities in the refractive index, the fields must be linked by appropriate boundary conditions at an interface between two regions of different refractive indices, as shown in Figure 2.1.

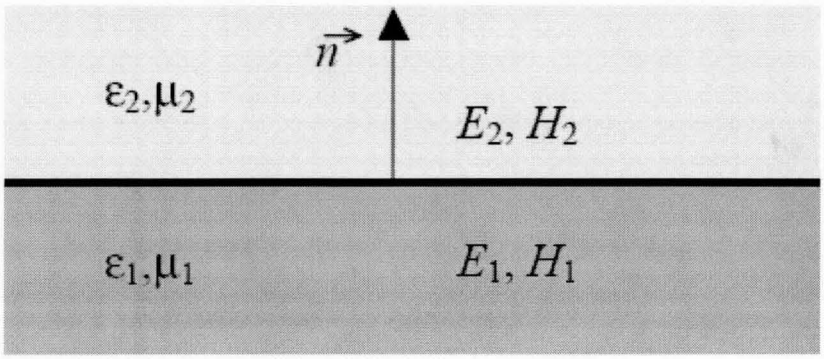

Figure 2.1 Discontinuity in a medium.

When surface charges and surface currents are absent, the boundary conditions for the electromagnetic fields are summarized as follows.

(a) Tangential components of the electric fields are continuous

$$E_{1t} = E_{2t}. \tag{2.51}$$

(b) Tangential components of the magnetic fields are continuous

$$H_{1t} = H_{2t}. \tag{2.52}$$

(c) Normal components of the electric flux densities are continuous

$$D_{1n} = D_{2n}. \tag{2.53}$$

(d) Normal components of the magnetic flux densities are continuous

$$B_{1n} = B_{2n} \tag{2.54}$$

In non-magnetic medium ($\mu_1 = \mu_2 = \mu_0$), Eq. (2.54) is reduced to

$$H_{1n} = H_{2n} \tag{2.55}$$

In the Eqs. (2.51) – (2.55), the subscript n and t are unit normal and tangential vectors at the boundary, respectively.

2.5 Summary

In this chapter, we present the basic of the electromagnetic theory of light. Starting from the general time-domain Maxwell's equations, we derive the frequency-domain Maxwell's equations for time-harmonic light waves propagating in a source-free, linear, isotropic, non-conductive and non-magnetic medium. The vectorial wave equations for both the electric fields and magnetic fields are then derived to describe the light propagation in optical waveguides. For longitudinally slow-varying waveguide structures, we further derive the wave equations in terms of transverse field components which are frequently used in practice.

Optical waveguides are inherently inhomogeneous structures, in the sense that different media with different refractive index are necessary to achieve light confinement. The boundary conditions for the electromagnetic fields are also presented in this chapter. The boundary conditions and Maxwell's equations form the foundation of this thesis and will be used throughout the remaining of this thesis in various forms for the modeling of different photonic devices.

Chapter 3
Finite-Difference Methods

3.1 Introduction

The wave equations derived in chapter 2 are second-order partial differential equations. The exact solution of these partial differential equations is only available for some simple structures, such as step-index slab waveguides and optical fibers. For more complicated structures, wave equations have to be solved numerically, aiming at the numerical solution. The finite-difference method (FDM) is one of the most well-known numerical methods, which is widely used in the mode analysis and propagation analysis. In the FDM, the partial differential equation is transformed into a matrix equation by approximating the derivatives with a finite-difference (FD) formula. The FD formula plays a key role in the FDM for the numerical solution of wave equations. Several formulations have been proposed to improve the accuracy and efficiency of the FDM [49]-[53].

The simplest FD scheme for mode equations is the central difference scheme [44] on a uniform mesh. In this formulation, by using the Taylor series expansion, the second-order partial derivatives at a grid point are represented by linear combinations of the three field values at, and directly adjacent to, the grid point. This formulation is second-order accurate for homogenous materials and is thus referred to as the scalar formula. For step-

index waveguides, the Taylor series expansion regarding the derivatives cannot be done universally due to the existence of dielectric discontinuity. Stern [8] derived an improved formula for semi-vectorial mode solvers based on graded index approximation. The derivation is analogy to the simplest formulation, but the dielectric discontinuity is considered by means of averaging the refractive indices over meshes. Since this method assumes a continuous second-order derivative, the accuracy is $O\left(h^0\right)$ for step-index waveguides, where h is the mesh size, in the case where dielectric interfaces lie midway between grid points. Otherwise, the accuracy becomes even worse.

Aiming at accurately modeling step-index waveguides, Vassallo [49] developed a vectorial three-point FD formula by a different methodology, in which Taylor series expansions to sampling points are performed in neighbouring homogeneous regions and the dielectric interface conditions between different refractive indices are rigorously matched by making use of the Helmholtz equation. This formula achieves $O\left(h^2\right)$ accuracy when the dielectric interface is placed midway between grid points and $O(h)$ accuracy otherwise. Yamauchi *et al.* [53] improved Vassallo's formula to $O\left(h^2\right)$ accuracy regardless of the interface position by evaluating the third-order derivative with the help of Fresnel equation (one-way BPM equation).

Formulas with accuracy higher than $O\left(h^2\right)$ are called high-order formulas. The greatest advantage of high-order formulas lies in their ability to provide accurate results even with very coarse meshes, resulting in dramatic savings in computational cost. The

standard method for deriving high-order formulas is to include additional high-order derivatives into Taylor series expansions. For the simplest FD formula, the Taylor series expansion to sampling points is truncated by neglecting derivatives higher than second order. If additional high-order derivatives are retained therein, the accuracy of the resulting formula will be improved. High-order formulas achieved in this manner always require non-compact stencils that involve more sampling field values. As a result, the matrix will no longer be tridiagonal, hence increasing the computational cost. However, by using the Douglas scheme [54], a three-point formula with $O\left(h^4\right)$ accuracy can be obtained when the medium is homogeneous. Sun *at el.* [55] introduced this formula to the one-way BPM. Alternatively, Yamauchi *et al.* [56] evaluated the fourth-order derivative contained in Taylor series expansions using the generalized Douglas scheme and the Fresnel equation as well, leading to a homogeneous $O\left(h^4\right)$ accurate FD formula. However, interfaces conditions are not treated in the above two formulations. For step-index waveguides, their accuracies are still $O\left(h^2\right)$ at best and are reduced to $O\left(h\right)$ when the interface does not fall midway between sampling points.

Hadley proposed a quasi-fourth-order scheme [57] for step-index waveguides in which the grid points coincide with dielectric interfaces. The high-order derivatives are evaluated through the Helmholtz propagation equation and complex averaging techniques. Chiou *et al.* [58] improved Vassallo's formula by including higher-order derivatives and evaluating them through the Douglas scheme to give $O\left(h^3\right)$ accuracy for

arbitrarily positioned interfaces and $O(h^4)$ accuracy where interfaces lie midway between sampling points.

Please note that all the high-order FD formulas mentioned above are three-point schemes. That means high accuracy can be achieved without sacrificing the efficiency. This attractive feature motivates us to develop various propagation techniques based on these high-order FD schemes. Before proceeding, we first present various frequently used FD formulas and their derivations in this chapter.

3.2 Derivations of Various FD Formulas

All FD formulas for second-order derivatives can be classified into two categories: homogeneous formulas which are derived from the Taylor series expansion only and heterogeneous formulas which are derived by the Taylor series expansion and rigorously matching the interface conditions. We start with homogeneous formulas.

3.2.1 Central Difference Scheme

Assume that the one-dimensional (1D) field function $\Psi(x)$ is continuous and smooth. As shown in Figure 3.1, the sampled field values are Ψ_{i-1}, Ψ_i and Ψ_{i+1} at grid points characterized by refractive index n_{i-1}, n_i and n_{i+1}, respectively.

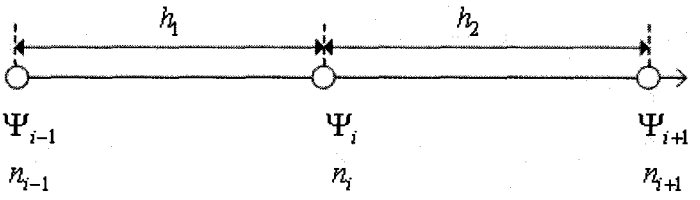

Figure 3.1 Schematics of three consecutive grid points.

Using the Taylor series expansion around the point i, Ψ_{i+1} and Ψ_{i-1} are expressed as

$$\Psi_{i+1} = \Psi_i + \frac{\partial \Psi}{\partial x} h_2 + \frac{1}{2} \frac{\partial^2 \Psi}{\partial x^2} h_2^2 + O\left(h^3\right) \tag{3.1}$$

$$\Psi_{i-1} = \Psi_i - \frac{\partial \Psi}{\partial x} h_1 + \frac{1}{2} \frac{\partial^2 \Psi}{\partial x^2} h_1^2 + O\left(h^3\right) \tag{3.2}$$

The operation $\frac{\text{Eq.(3.1)}}{h_2^2} - \frac{\text{Eq.(3.2)}}{h_1^2}$ eliminates the second-order derivative and gives the expression for the first-order derivative

$$\frac{\partial \Psi}{\partial x} = \frac{\frac{h_1}{h_2} \Psi_{i+1} - \frac{h_2}{h_1} \Psi_{i-1} + \left(\frac{h_2}{h_1} - \frac{h_1}{h_2} \right) \Psi_i}{h_1 + h_2}. \tag{3.3}$$

The operation $\frac{\text{Eq.(3.1)}}{h_2} + \frac{\text{Eq.(3.2)}}{h_1}$ eliminates the first-order derivative and gives the expression for the second-order derivative

$$\frac{\partial^2 \Psi}{\partial x^2} = \frac{\frac{1}{h_2} \Psi_{i+1} + \frac{1}{h_1} \Psi_{i-1} - \left(\frac{1}{h_1} + \frac{1}{h_2} \right) \Psi_i}{\frac{1}{2}\left(h_1 + h_2\right)} \tag{3.4}$$

In the case of uniform mesh i.e., $h_1 = h_2$, we have

$$\frac{\partial \Psi}{\partial x} = \frac{\Psi_{i+1} - \Psi_{i-1}}{2h} \tag{3.5}$$

$$\frac{\partial^2 \Psi}{\partial x^2} = \frac{\Psi_{i+1} - 2\Psi_i + \Psi_{i-1}}{h^2} \tag{3.6}$$

Eq. (3.6) is the well-known central difference scheme. In homogeneous materials, its accuracy is $O(h^2)$ for uniform mesh and $O(h)$ for non-uniform mesh.

For the second-order derivative containing the refractive index term, such as the term $\frac{\partial}{\partial x}\left[\frac{1}{n^2}\frac{\partial}{\partial x}\left(n^2 E_x\right)\right]$ appearing in Eq.(2.36), its FD expression can be obtained by differencing the first-order derivative in sequence. For the sake of simplicity, we present the derivation for uniform mesh as follows.

$$\begin{aligned}
&\frac{\partial}{\partial x}\left[\frac{1}{n^2}\frac{\partial}{\partial x}\left(n^2\Psi\right)\right] = \frac{1}{h}\left[\frac{1}{n^2}\frac{\partial}{\partial x}\left(n^2\Psi\right)\Big|_{i+1/2} - \frac{1}{n^2}\frac{\partial}{\partial x}\left(n^2\Psi\right)\Big|_{i-1/2}\right] \\
&= \frac{1}{h}\left[\frac{2}{n_i^2 + n_{i+1}^2}\frac{n_{i+1}^2\Psi_{i+1} - n_i^2\Psi_i}{h} - \frac{2}{n_i^2 + n_{i-1}^2}\frac{n_i^2\Psi_i - n_{i-1}^2\Psi_{i-1}}{h}\right] \\
&= \frac{2n_{i+1}^2}{n_i^2 + n_{i+1}^2}\frac{\Psi_{i+1}}{h^2} - \left(\frac{n_i^2}{n_i^2 + n_{i+1}^2} + \frac{n_i^2}{n_i^2 + n_{i-1}^2}\right)\frac{2\Psi_i}{h^2} + \frac{2n_{i-1}^2}{n_i^2 + n_{i-1}^2}\frac{\Psi_{i-1}}{h^2} \\
&\square \frac{a_i\Psi_{i+1} - 2b_i\Psi_i + c_i\Psi_{i-1}}{h^2}
\end{aligned} \tag{3.7}$$

where

$$a_i = \frac{2n_{i+1}^2}{n_{i+1}^2 + n_i^2} \tag{3.8}$$

$$b_i = n_i^2\left(\frac{1}{n_{i-1}^2 + n_i^2} + \frac{1}{n_i^2 + n_{i+1}^2}\right) \tag{3.9}$$

$$c_i = \frac{2n_{i-1}^2}{n_{i-1}^2 + n_i^2}. \tag{3.10}$$

The FD expressions for other second-order derivatives containing the refractive index term can be obtained in a similar way.

3.2.2 Scalar Fourth-Order FD Formula

Following the derivation of the central difference scheme, a fourth-order FD formula can be developed for uniform mesh by retaining derivative terms of up to fifth order in the Taylor series expansions to Ψ_{i+1} and Ψ_{i-1}

$$\Psi_{i+1} = \Psi_i + \frac{h}{1!}\frac{\partial\Psi}{\partial x} + \frac{h^2}{2!}\frac{\partial^2\Psi}{\partial x^2} + \frac{h^3}{3!}\frac{\partial^3\Psi}{\partial x^3} + \frac{h^4}{4!}\frac{\partial^4\Psi}{\partial x^4} + \frac{h^5}{5!}\frac{\partial^5\Psi}{\partial x^5} + O\left(h^6\right) \tag{3.11}$$

$$\Psi_{i-1} = \Psi_i - \frac{h}{1!}\frac{\partial\Psi}{\partial x} + \frac{h^2}{2!}\frac{\partial^2\Psi}{\partial x^2} - \frac{h^3}{3!}\frac{\partial^3\Psi}{\partial x^3} + \frac{h^4}{4!}\frac{\partial^4\Psi}{\partial x^4} - \frac{h^5}{5!}\frac{\partial^5\Psi}{\partial x^5} + O\left(h^6\right). \tag{3.12}$$

Addition of Eq.(3.12) to Eq.(3.11) gives

$$\frac{\Psi_{i+1} - 2\Psi_i + \Psi_{i-1}}{h^2} = \frac{\partial^2\Psi}{\partial x^2} + \frac{h^2}{12}\frac{\partial^4\Psi}{\partial x^4} + O\left(h^4\right). \tag{3.13}$$

By applying the Douglas scheme [54], Eq.(3.13) becomes

$$\begin{aligned} \frac{\delta_x^2\Psi_i}{h^2} &= \frac{\partial^2\Psi}{\partial x^2} + \frac{h^2}{12}\frac{\partial^2}{\partial x^2}\left(\frac{\partial^2\Psi}{\partial x^2}\right) + O\left(h^4\right) \\ &\approx \frac{\partial^2\Psi}{\partial x^2} + \frac{1}{12}\delta_x^2\left(\frac{\partial^2\Psi}{\partial x^2}\right) + O\left(h^4\right) \end{aligned} \tag{3.14}$$

where

$$\delta_x^2 \Psi_i \equiv \Psi_{i+1} - 2\Psi_i + \Psi_{i-1}. \tag{3.15}$$

Eq.(3.14) is rewritten as

$$\left(1 + \frac{1}{12}\delta_x^2\right)\frac{\partial^2 \Psi}{\partial x^2} = \frac{\delta_x^2 \Psi}{h^2} + O\left(h^4\right). \tag{3.16}$$

Eq.(3.16) is derived based on homogeneous refractive index profiles and its truncation error is $O(h^4)$, so it is called scalar fourth-order FD formula. It is worth noting that the operator δ_x^2 is a three-point operator. The matrix based on this formula is still tridiagonal, hence no increase in the computation effort.

For those second-order derivatives containing refractive index terms, a high-order FD formula can be still obtained by replacing the operator δ_x^2 in the Eq.(3.16) with the following operator

$$\delta_x^2 \Psi_i \equiv a_i \Psi_{i+1} - 2b_i \Psi_i + c_i \Psi_{i-1} \tag{3.17}$$

where coefficients a_i, b_i and c_i can be found in Eqs.(3.8)-(3.10). Although the $O(h^4)$ accuracy is not ensured because of averaging the refractive index, the improvement in accuracy in comparison with the central difference scheme is no doubt.

3.2.3 Vectorial Fourth-Order FD Formula

As it can be seen from the above two subsections, both the central difference scheme and the scalar fourth-order FD formula are derived based on homogeneous refractive index profiles. They achieve a good accuracy in the modeling of graded-index waveguides, but are not sufficient in the case of step-index structures. Vassallo [49] and

Chiou *et al.* [58] did the pioneering work on the development of vectorial FD formulas for step-index slab waveguides. Following the procedure proposed by Chiou *et al.*, we derive a vectorial fourth-order FD formula that can be used in either electric field or magnetic field formulations.

Consider the three consecutive points shown in Figure 3.2, where refractive index discontinuities exist between sampling points.

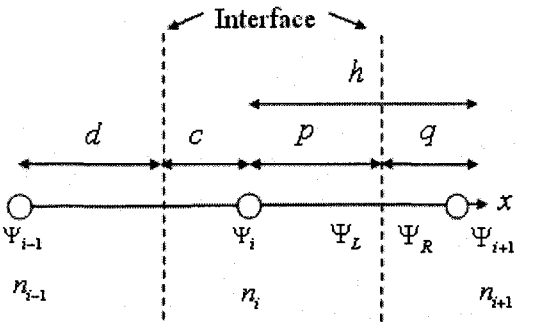

Figure 3.2 Schematics of grid points with discontinuities.

Using the Taylor series expansion within a uniform medium, Ψ_L is expanded in terms of Ψ_i as

$$\Psi_L = \Psi_i + \frac{p}{1!}\frac{\partial \Psi_i}{\partial x} + \frac{p^2}{2!}\frac{\partial^2 \Psi_i}{\partial x^2} + \frac{p^3}{3!}\frac{\partial^3 \Psi_i}{\partial x^3} + \frac{p^4}{4!}\frac{\partial^4 \Psi_i}{\partial x^4} + \frac{p^5}{5!}\frac{\partial^5 \Psi_i}{\partial x^5} + O(h^6). \quad (3.18)$$

Similarly, Ψ_{i+1} is expressed in terms of Ψ_R as

$$\Psi_{i+1} = \Psi_R + \frac{q}{1!}\frac{\partial \Psi_R}{\partial x} + \frac{q^2}{2!}\frac{\partial^2 \Psi_R}{\partial x^2} + \frac{q^3}{3!}\frac{\partial^3 \Psi_R}{\partial x^3} + \frac{q^4}{4!}\frac{\partial^4 \Psi_R}{\partial x^4} + \frac{q^5}{5!}\frac{\partial^5 \Psi_R}{\partial x^5} + O(h^6). \quad (3.19)$$

To guarantee the fourth-order accuracy, we let the refractive index discontinuity lie midway between sampling points, i.e., $p = q = h/2$. The boundary conditions require that

$$\Psi_R = \theta_E \Psi_L \tag{3.20}$$

$$\Psi'_R = \theta_H \Psi'_L \tag{3.21}$$

where θ_E and θ_H are coefficients that take into account the boundary conditions for the electric and magnetic fields at the refractive index discontinuity. Their values are summarized in Table 3.1.

	E-field		H-field	
	TE	TM	TE	TM
θ_E	1	n_i^2/n_{i+1}^2	1	1
θ_H	1	1	1	n_{i+1}^2/n_i^2

Table 3.1 Values of θ

The higher-order derivatives of Ψ_R and Ψ_L are connected by the one-dimensional Helmholtz equation

$$\beta^2 \Psi = \left(\frac{\partial^2}{\partial x^2} + k_0^2 n^2 \right) \Psi . \tag{3.22}$$

From Eq. (3.20) and (3.22), we have

$$\left(\frac{\partial^2}{\partial x^2} + k_0^2 n_{i+1}^2 \right) \Psi_R = \left(\frac{\partial^2}{\partial x^2} + k_0^2 n_i^2 \right) \theta_E \Psi_L \tag{3.23}$$

or

$$\Psi''_R = \theta_E \left(\Psi''_L + \eta \Psi_L \right). \tag{3.24}$$

Similarly, the higher-order derivatives of Ψ_R and Ψ_L are connected as

$$\Psi_R^{(3)} = \theta_H \left(\Psi_L^{(3)} + \eta \Psi'_L \right) \tag{3.25}$$

$$\Psi_R^{(4)} = \theta_E \left(\Psi_L^{(4)} + 2\eta \Psi_L'' + \eta^2 \Psi_L \right) \tag{3.26}$$

$$\Psi_R^{(5)} = \theta_H \left(\Psi_L^{(5)} + 2\eta \Psi_L^{(3)} + \eta^2 \Psi_L' \right) \tag{3.27}$$

where $\eta = k_0^2 \left(n_i^2 - n_{i+1}^2 \right)$. By substituting Eqs.(3.20), (3.21) and (3.24) - (3.27) into (3.19) and appropriately differentiating (3.18), Ψ_{i+1} can be expressed in terms of Ψ_i as

$$\Psi_{i+1} = f_0 \Psi_i + f_1 \Psi_i' + f_2 \Psi_i'' + f_3 \Psi_i^{(3)} + f_4 \Psi_i^{(4)} + f_5 \Psi_i^{(5)} + O(h^6). \tag{3.28}$$

The following expression can be similarly obtained

$$\Psi_{i-1} = e_0 \Psi_i + e_1 \Psi_i' + e_2 \Psi_i'' + e_3 \Psi_i^{(3)} + e_4 \Psi_i^{(4)} + e_5 \Psi_i^{(5)} + O(h^6) \tag{3.29}$$

where the coefficients are given in Appendix A. The difference forms of Ψ_i' and Ψ_i'' are derived as follows by ignoring the higher-order terms containing $\Psi_i^{(3)}$, $\Psi_i^{(4)}$, and $\Psi_i^{(5)}$ in Eqs.(3.28) and (3.29)

$$\begin{aligned} \Psi_i' &= \frac{f_2 \Psi_{i-1} + \left(f_0 e_2 - e_0 f_2 \right) \Psi_i - e_2 \Psi_{i+1}}{e_1 f_2 - f_1 e_2} + O(h^2) \\ &= s_- \Psi_{i-1} + s_0 \Psi_i + s_+ \Psi_{i+1} \approx D_x \Psi_i \end{aligned} \tag{3.30}$$

$$\begin{aligned} \Psi_i'' &= \frac{f_1 \Psi_{i-1} + \left(f_0 e_1 - e_0 f_1 \right) \Psi_i - e_1 \Psi_{i+1}}{e_2 f_1 - f_2 e_1} + O(h^2) \\ &= t_- \Psi_{i-1} + t_0 \Psi_i + t_+ \Psi_{i+1} \approx D_x^2 \Psi_i \end{aligned} . \tag{3.31}$$

Eliminating Ψ_i' and $\Psi_i^{(5)}$ simultaneously in Eqs.(3.28) and (3.29), we obtain

$$\begin{aligned} &\frac{f_1 \Psi_{i-1} + \left(f_0 e_1 - e_0 f_1 \right) \Psi_i - e_1 \Psi_{i+1}}{e_2 f_1 - f_2 e_1} \\ &= \Psi_i'' + g_1 \Psi_i^{(3)} + g_2 \Psi_i^{(4)} + O(h^4) \\ &= \left(1 + g_1 \frac{\partial}{\partial x} + g_2 \frac{\partial^2}{\partial x^2} \right) \Psi_i'' + O(h^4) \end{aligned} \tag{3.32}$$

where g_1 and g_2 are given in Appendix A. Replacing the first and second differential operators in the brackets of Eq.(3.32) with (3.30) and (3.31), respectively, we finally obtain the fourth-order FD formula:

$$\Psi_i'' = \frac{D_x^2 \Psi_i}{1 + g_1 D_x + g_2 D_x^2} + O(h^4). \tag{3.33}$$

For homogeneous materials, all the coefficients regarding the refractive index discontinuity in Eq.(3.33) can be ignored, leading to the scalar four-order FD formula which is same as Eq.(3.16).

3.2.4 Vectorial Second-Order FD Formula

The vectorial second-order FD formula can be obtained when the high-order terms up to third derivative are retained in the above derivation. Doing so leads to the following expression:

$$\Psi_i'' = \frac{b_1 \Psi_{i-1} + (b_0 a_1 - a_0 b_1)\Psi_i - a_1 \Psi_{i+1}}{a_2 b_1 - b_2 a_1} + O(h^2) \tag{3.34}$$

where the coefficients are summarized in Appendix A. By neglecting the refractive index discontinuity in these coefficients, Eq.(3.34) is reduced to the central difference scheme.

3.3 Evaluations of Various FD Formulas

The accuracy of various FD formulas is evaluated by calculating the transverse wave number of the TE mode supported by a symmetric slab waveguide. The investigated

structure is a step-index waveguide with high index contrast. The core and cladding indices are $n_{core}=1.5$ and $n_{clad}=1.0$, respectively. The core width is $D=0.427$ μm and the wavelength is $\lambda=1.0$ μm. The exact values of the transverse wave numbers in the core and cladding are given by $k_x=k_0\sqrt{n_{core}^2-n_{eff}^2}$ and $\alpha_x=k_0\sqrt{n_{eff}^2-n_{clad}^2}$, respectively, where n_{eff} is the effective index of the TE mode. For this structure, the exact value of the effective index is $n_{eff}=1.336021280054586$, hence the exact values of the transverse wave numbers are $k_{x,exact}=4.284778310330654$ and $\alpha_{x,exact}=5.566749216263184$, respectively. The numerical values of k_x or α_x can be calculated by using various FD formulas including Eqs.(3.6), (3.16), (3.33) and (3.34). For example

$$\tau_{numerical}=\frac{D_x^2\Psi_i}{\left(1+g_1D_x+g_2D_x^2\right)\Psi_i} \tag{3.35}$$

for the vectorial fourth-order FD formula, where $\tau=-k_x^2$ in the core region and $\tau=\alpha_x^2$ in the cladding region. In the calculation of $\tau_{numerical}$, the sampled fields Ψ_i and $\Psi_{i\pm1}$ are assigned with exact values. In order to evaluate different FD formulas, we calculate the relative error in the transverse wave number defined as

$$\in k_x=\left|\frac{k_{x,numerical}-k_{x,exact}}{k_0\left(n_{core}-n_{clad}\right)}\right| \tag{3.36}$$

in the core region, or

$$\in \alpha_x=\left|\frac{\alpha_{x,numerical}-\alpha_{x,exact}}{k_0\left(n_{core}-n_{clad}\right)}\right| \tag{3.37}$$

in the cladding region. The relative error in the transverse wave number depends on the accuracy of the FD formula only, thus enabling us to evaluate different formulas effectively.

Figure 3.3 shows $\in k_x$ as a function of the mesh size for three consecutive grid points without an index discontinuity between them, i.e., $n_{i-1} = n_i = n_{i+1} = n_{core}$. As it can be seen, the slope is two for central difference scheme and vectorial second-order formula, indicating their truncation error is $O(h^2)$, and the slope is four for scalar and vectorial four-order formulas, indicating their truncation error is $O(h^4)$. The calculated truncation errors match exactly with the theoretical derivation. The calculations also clearly verify the superiority of high-order FD formulas in approximating the second-order derivatives. It is observed that the truncation error of scalar formulas coincides with vectorial formulas for both $O(h^2)$ and $O(h^4)$ formulations. Since there is no index discontinuity between sampling points, the vectorial formula degenerates to the scalar formula. In practice, the scalar formula is able to provide accurate answers in modeling of graded-index structures.

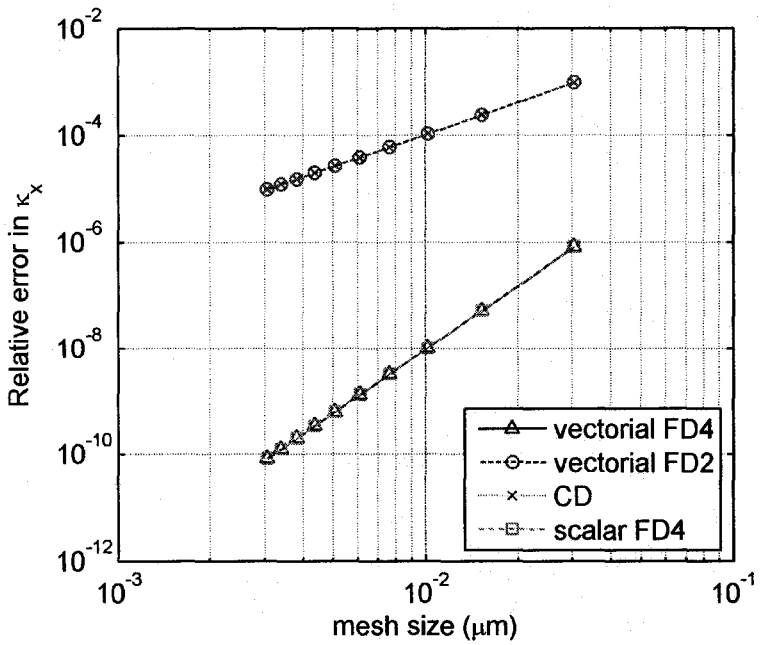

Figure 3.3 Relative error in the transverse wave number as a function of mesh size: without index discontinuity. Legends vectorial FD4, vectorial FD2, CD and scalar FD4 represent vectorial four-order FD formula, vectorial second-order FD formula, central difference scheme and scalar fourth-order FD formula, respectively.

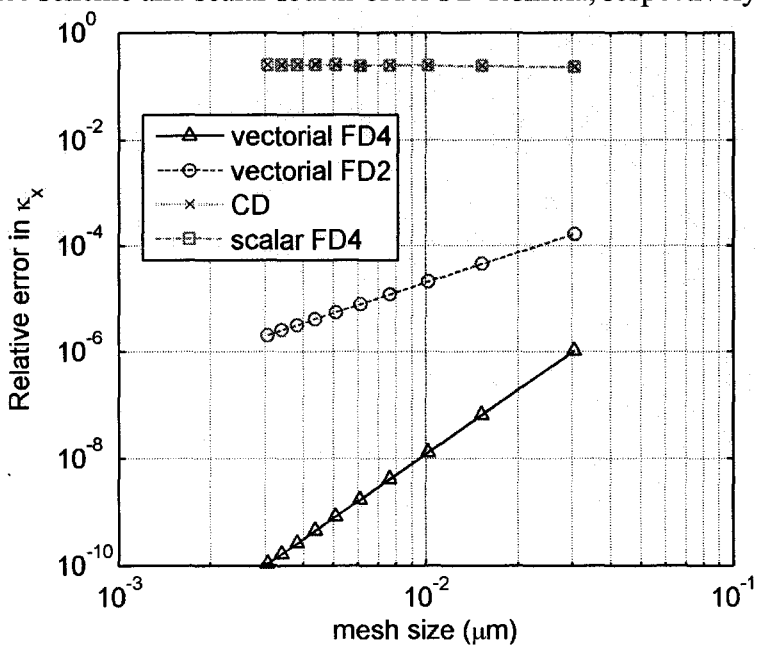

Figure 3.4 Relative error in the transverse wave number as a function of mesh size: with index discontinuity. The legend is the same with Figure 3.3.

Figure 3.4 shows $\in k_x$ as a function of the mesh size for three consecutive grid points around the interface, i.e., $n_{i-1} = n_i = n_{core}$, $n_{i+1} = n_{clad}$. It can be seen that the slopes are two and four for vectorial second-order and vectorial fourth-order formulas, respectively. That means the accuracy of vectorial formulas can be still maintained even if index discontinuities exist. In contrast, the $\in k_x$ calculated by scalar formulas cannot be reduced with decreasing mesh size. The slopes of both the central difference scheme and the scalar fourth-order FD formula indicate $O(h^0)$ accuracy. The dramatic degradation of accuracy for scalar formulas is due to the existence of the large index discontinuity. Therefore, in the simulation of step-index waveguides with high index contrast, high-order vectorial FD formulas are highly desirable because of not only the increased accuracy but also the improved efficiency.

3.4 Summary

In this chapter, four types of finite-difference (FD) formulas frequently used in solving partial differential wave equations are given, i.e., conventional central difference scheme, scalar fourth-order FD, vectorial second-order FD, and vectorial fourth-order FD formulas. Their truncation errors are analyzed by the Taylor series expansion.

The accuracies of various FD formulas are assessed in a step-index slab waveguide by exact field values. The superiority of the vectorial fourth-order FD formula over other FD formulas is clearly demonstrated.

Chapter 4
High-Order Mode Solving Techniques

4.1 Introduction

An optical mode is a particular intensity pattern of a beam of electromagnetic wave propagating in optical waveguides in a plane perpendicular (i.e. transverse) to the propagation direction of the beam. Two characteristics of an optical mode are the mode profile which describes the transverse intensity pattern, and the propagation constant which describes the phase velocity and the attenuation rate. Optical modes are determined by the refractive index profile of an optical waveguide and the operating wavelength. Modal analysis is the fundamental basis for the design of optical waveguides.

Modal solutions of a three-dimensional (3D) waveguide can be obtained by numerically solving the wave equations derived in chapter 2 with the replacement of $\partial/\partial z = -j\beta$, where β is the propagation constant. For one-dimensional (1D) slab waveguides, 1D wave equations can be directly derived from the Maxwell's equations. Since the electric and magnetic fields supported by slab waveguides show no dependence on one transverse direction, modal solutions are decoupled into two sets: the transverse electric mode (TE mode) and the transverse magnetic mode (TM mode) [59]. Analytical solutions exist for slab waveguides and will be derived in this chapter for special case of three-layer slab. The 1D wave equations can be also solved by the finite-difference

method. Although various FD formulas are assessed by an analytical method in chapter 3, they are not utilized to solve wave equations therein. In this chapter, we solve the 1D wave equations for both TE and TM mode using the central difference scheme and the vectorial fourth-order FD formula to gain a taste of the advantage of high-order FD formulas in mode solving techniques. The availability of an analytical solution to slab waveguides enables us to compare the accuracy of these two FD formulas.

In recent years, surface plasmonic waveguides [60]-[64] have attracted particular attention as they can confine and guide light in nanometer scale regime. An analytical solution to the long-range surface plasmon polariton (LRSPP) mode supported by thin metal films [65][66] is also presented in this chapter, which will be used in a later chapter.

It is well known that bends in dielectric waveguides are an important element for photonic integrated circuits [67]. Therefore, it is essential to be able to design and simulate these bends in an accurate and efficient manner. A number of theoretical analyses have been done to investigate the characteristics of these curved waveguides [68]-[70]. In order to build compact photonic integrated circuits, high index contrast waveguides are generally preferred as they can achieve much smaller bending radius [48]. In view of the large index discontinuity and the resulting small core width, we introduce the high-order FDM to the analysis of waveguide bends in this chapter. There are two popular numerical models, namely, the conformal transformation method [68] in which the curved waveguide is translated into an equivalent straight waveguide with a transformed index profile, and the cylindrical coordinate system formulation [70].

Important characteristics of waveguide bends, such as bending loss, minimum bending radius, confinement factor and polarization dependence are investigated.

4.2 One-Dimensional (1D) Wave Equation

The 1D wave equation can be derived from Maxwell's equations

$$\nabla \times E = -j\omega\mu_0 H \tag{4.1}$$

$$\nabla \times H = j\omega n^2 \varepsilon_0 E\,. \tag{4.2}$$

Separating components gives

$$\frac{\partial E_z}{\partial y} - \frac{\partial E_y}{\partial z} = -j\omega\mu_0 H_x \tag{4.3}$$

$$\frac{\partial E_x}{\partial z} - \frac{\partial E_z}{\partial x} = -j\omega\mu_0 H_y \tag{4.4}$$

$$\frac{\partial E_y}{\partial x} - \frac{\partial E_x}{\partial y} = -j\omega\mu_0 H_z \tag{4.5}$$

$$\frac{\partial H_z}{\partial y} - \frac{\partial H_y}{\partial z} = j\omega\varepsilon_0 n^2 E_x \tag{4.6}$$

$$\frac{\partial H_x}{\partial z} - \frac{\partial H_z}{\partial x} = j\omega\varepsilon_0 n^2 E_y \tag{4.7}$$

$$\frac{\partial H_y}{\partial x} - \frac{\partial H_x}{\partial y} = j\omega\varepsilon_0 n^2 E_z\,. \tag{4.8}$$

To develop 1D wave equation, we consider the 1D structure illustrated in Figure 4.1.

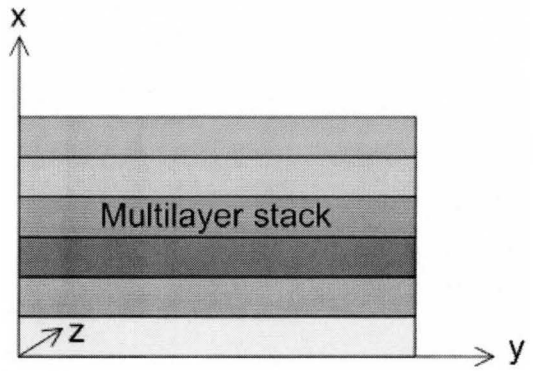

Figure 4.1 Schematics of one-dimensional waveguide.

The confinement is assumed to be in the x direction. The light is assumed to propagate in $+z$ direction. Since the structure is uniform in the propagation direction, the derivative with respect to the z coordinate, $\partial/\partial z$, can be replaced by $-j\beta$. In addition, the structure is also assumed to be infinite in the $\pm y$ direction. The electric and magnetic fields supported by this structure therefore show no dependence on this direction, i.e., $\partial/\partial y = 0$ and hence Eqs.(4.3)-(4.8) simplify to

$$\beta E_y = -\omega\mu_0 H_x \tag{4.9}$$

$$j\beta E_x + \frac{\partial E_z}{\partial x} = j\omega\mu_0 H_y \tag{4.10}$$

$$\frac{\partial E_y}{\partial x} = -j\omega\mu_0 H_z \tag{4.11}$$

$$\beta H_y = \omega\varepsilon_0 n^2 E_x \tag{4.12}$$

$$j\beta H_x + \frac{\partial H_z}{\partial x} = -j\omega\varepsilon_0 n^2 E_y \tag{4.13}$$

$$\frac{\partial H_y}{\partial x} = j\omega\varepsilon_0 n^2 E_z . \tag{4.14}$$

Two types of modes are defined for 1D waveguides: TE mode and TM mode. The TE mode contains only electric fields that are transverse to the propagation direction, i.e., $E_z = 0$. Similarly, the TM mode contains no magnetic fields in the propagation direction hence $H_z = 0$. By applying these definitions to Eqs.(4.9) - (4.14), we have

$$E_x = E_z = H_y = 0 \tag{4.15}$$

for TE mode and

$$H_x = H_z = E_y = 0 . \tag{4.16}$$

for TM mode. In other words, the TE mode only contains the E_y, H_x and H_z field components while the TM mode only contains the H_y, E_x and E_z field components.

For the TE mode, applying Eq.(4.15) to Eqs.(4.9) - (4.14) gives

$$\beta E_y = -\omega\mu_0 H_x \tag{4.17}$$

$$\frac{\partial E_y}{\partial x} = -j\omega\mu_0 H_z \tag{4.18}$$

$$j\beta H_x + \frac{\partial H_z}{\partial x} = -j\omega\varepsilon_0 n^2 E_y . \tag{4.19}$$

Substituting Eqs.(4.17) and (4.18) into (4.19), we get the following TE wave equation for E_y

$$\frac{d^2E_y}{dx^2}+\left(k_0^2n^2-\beta^2\right)E_y=0. \tag{4.20}$$

Similarly, we can get the TM wave equation for H_y

$$\frac{d^2H_y}{dx^2}+\left(k_0^2n^2-\beta^2\right)H_y=0. \tag{4.21}$$

These 1D wave equations can be solved by either numerical methods or analytical methods. We will discuss the solution methods in the following sections.

4.3 Analytical Methods

For 1D multilayer structures, there exist analytical solutions to the wave equations (4.20) and (4.21). As examples of analytical methods, we will solve the wave equations for three-layer dielectric slab waveguides and thin metal films surrounded by dielectric. Three-layer dielectric slab waveguides can be further classified into symmetric and asymmetric structures according to the refractive index of cladding layers, both of which will be discussed in the following subsections. Only guided modes are considered here.

4.3.1 Symmetric Three-Layer Slab Waveguides

The schematic diagram of symmetric three-layer slab waveguides is shown in Figure 4.2. Assume that the layer of refractive index n_1 and thickness $2a$ is the guiding

layer. The upper and lower cladding layers are assumed to be extended to $\pm\infty$ in y direction and have the same refractive index n_2.

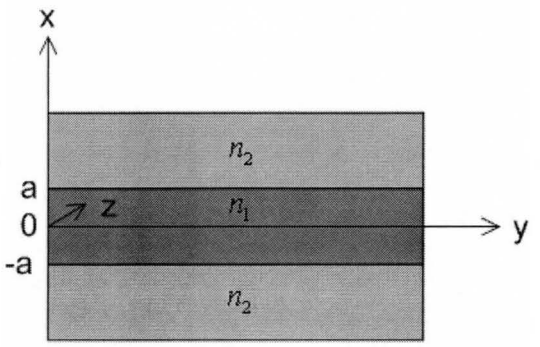

Figure 4.2 Schematics of symmetric three-layer slab waveguide.

We first derive analytical solutions to the TE mode. The TE wave equations in the guiding and cladding layers can be written separately as

$$\begin{aligned} &\frac{d^2E_y}{dx^2}+\left(k_0^2n_1^2-\beta^2\right)E_y=0 \quad (-a\le x\le a) \\ &\frac{d^2E_y}{dx^2}+\left(k_0^2n_2^2-\beta^2\right)E_y=0 \quad (x>a \text{ or } x<-a) \end{aligned} \tag{4.22}$$

Since we only consider the guided modes here, the propagation constant β varies in the range of $k_0n_2<\beta<k_0n_1$, thus we define

$$\begin{aligned} \gamma_1^2&=k_0^2n_1^2-\beta^2 \\ \gamma_2^2&=\beta^2-k_0^2n_2^2 \end{aligned} \tag{4.23}$$

With this definition, Eq.(4.22) simplifies to

$$\begin{aligned} &\frac{d^2E_y}{dx^2}+\gamma_1^2E_y=0 \quad (-a\le x\le a) \\ &\frac{d^2E_y}{dx^2}-\gamma_2^2E_y=0 \quad (x>a \text{ or } x<-a) \end{aligned} \tag{4.24}$$

The general solution to Eq.(4.24) is

$$E_y(x)=\begin{cases} B\exp\left[\gamma_2(x+a)\right] & (-\infty<x\le -a) \\ A\cos(\gamma_1 x-\phi_1) & (-a\le x\le a) \\ C\exp\left[-\gamma_2(x-a)\right] & (a\le x<\infty) \end{cases} \tag{4.25}$$

where A、B、C、ϕ_1 are constants. Imposing the boundary condition, on the tangential fields at $x=a$, i.e. Eq. (2.51), we get the field distribution function for the TE even mode

$$E_y(x)=\begin{cases} A\cos(\gamma_1 a)\exp\left[\gamma_2(x+a)\right] & (-\infty<x\le -a) \\ A\cos(\gamma_1 x) & (-a\le x\le a) \\ A\cos(\gamma_1 a)\exp\left[-\gamma_2(x-a)\right] & (a\le x<\infty) \end{cases}. \tag{4.26}$$

Using the continuity of $\frac{dE_y(x)}{dx}$ at $x=a$, we have the following relation from the second and third equations in Eq.(4.26)

$$\gamma_1\sin(\gamma_1 a)=\gamma_2\cos(\gamma_1 a). \tag{4.27}$$

Further, we have

$$\tan(\gamma_1 a)=\frac{\gamma_2}{\gamma_1}\square T_2. \tag{4.28}$$

Therefore, we get the characteristic equation for the TE even mode

$$2\gamma_1 a=2m\pi+2\arctan T_2 \quad (2m = 0,\ 2,\ 4,\ \cdots). \tag{4.29}$$

Similarly, we can get the field distribution function for the TE odd mode

$$E_y(x)=\begin{cases} -A\sin(\gamma_1 a)\exp\left[\gamma_2(x+a)\right] & (-\infty < x \le -a) \\ A\sin(\gamma_1 x) & (-a \le x \le a) \\ A\sin(\gamma_1 a)\exp\left[-\gamma_2(x-a)\right] & (a \le x < \infty) \end{cases}, \tag{4.30}$$

and the characteristic equation

$$2\gamma_1 a=(2m-1)\pi+2\arctan T_2 \quad (2m-1 = 1, 3, 5, \cdots). \tag{4.31}$$

The field distribution function of the TM even mode can be derived in a way similar to the TE mode, i.e.,

$$H_y(x)=\begin{cases} A\cos(\gamma_1 a)\exp\left[\gamma_2(x+a)\right] & (-\infty < x \le -a) \\ A\cos(\gamma_1 x) & (-a \le x \le a) \\ A\cos(\gamma_1 a)\exp\left[-\gamma_2(x-a)\right] & (a \le x < \infty) \end{cases}. \tag{4.32}$$

The characteristic equation is obtained by using the continuity of $\frac{1}{n^2}\frac{dH_y(x)}{dx}$ at $x=a$, i.e.,

$$\frac{\gamma_1}{n_1^2}\sin(\gamma_1 a)=\frac{\gamma_2}{n_2^2}\cos(\gamma_1 a), \tag{4.33}$$

and further

$$2\gamma_1 a=2m\pi+2\arctan T_2 \quad (2m = 0, 2, 4, \cdots) \tag{4.34}$$

where $T_2=\left(n_1^2/n_2^2\right)(\gamma_2/\gamma_1)$.

Similarly, we can get the field distribution function for the TM odd mode

$$H_y(x)=\begin{cases} -A\sin(\gamma_1 a)\exp\left[\gamma_2(x+a)\right] & (-\infty < x \le -a) \\ A\sin(\gamma_1 x) & (-a \le x \le a) \\ A\sin(\gamma_1 a)\exp\left[-\gamma_2(x-a)\right] & (a \le x < \infty) \end{cases}, \tag{4.35}$$

and the characteristic equation

$$2\gamma_1 a = (2m-1)\pi + 2\arctan T_2 \quad (2m-1 = 1,\ 3,\ 5,\ \cdots). \tag{4.36}$$

In summary, the field distribution function for symmetric three-layer slab waveguides can be expressed in the following form

$$\psi(x)=\begin{cases} A\cos(\gamma_1 a+\phi_1)\exp\left[\gamma_2(x+a)\right] & (-\infty < x \le -a) \\ A\cos(\gamma_1 x-\phi_1) & (-a \le x \le a) \\ A\cos(\gamma_1 a-\phi_1)\exp\left[-\gamma_2(x-a)\right] & (a \le x < \infty) \end{cases} \tag{4.37}$$

where $\psi(x)=E_y(x)$ for TE modes and $\psi(x)=H_y(x)$ for TM modes, $\phi_1=0$ for even modes and $\phi_1=\pi/2$ for odd modes. The characteristic equations can be also written in a compact form

$$2\gamma_1 a = m\pi + 2\arctan T_2 \quad (m = 0,\ 1,\ 2,\cdots) \tag{4.38}$$

with $T_2=\left(n_1^2/n_2^2\right)^s(\gamma_2/\gamma_1)$, where $s=0$ for TE modes and $s=1$ for TM modes, $m=0,2,4,\cdots$ for even modes and $m=1,3,5,\cdots$ for odd modes. Note that Eq.(4.38) is a transcendental equation with respect to β. Its solution has to be found by numerical methods such as the bisection method.

4.3.2 Asymmetric Three-Layer Slab Waveguides

The schematic diagram of asymmetric three-layer slab waveguides is shown in Figure 4.3. Assume that the layer of refractive index n_1 and thickness b is the guiding layer. The refractive indices of upper and lower cladding layers n_3 and n_2, respectively. We assume $n_1 > n_2 > n_3$. Due to the loss of symmetry, the even or odd modes cannot be identified in asymmetric structures.

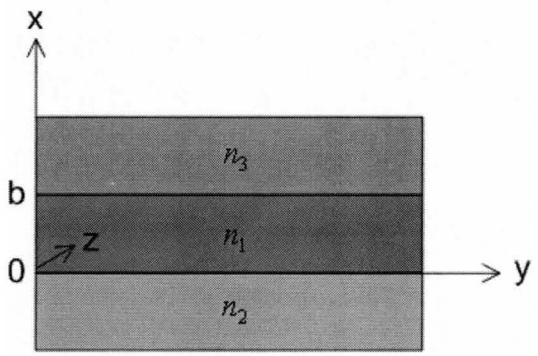

Figure 4.3 Schematics of asymmetric three-layer slab waveguide.

To derive the field distribution function for TE modes, we write the wave equations for each layer as

$$\begin{aligned}
&\frac{d^2E_y}{dx^2} + \left(k_0^2 n_2^2 - \beta^2\right) E_y = 0 \quad (-\infty < x \le 0) \\
&\frac{d^2E_y}{dx^2} + \left(k_0^2 n_1^2 - \beta^2\right) E_y = 0 \quad (0 \le x \le b) \quad . \\
&\frac{d^2E_y}{dx^2} + \left(k_0^2 n_3^2 - \beta^2\right) E_y = 0 \quad (b \le x < \infty)
\end{aligned} \tag{4.39}$$

For guided modes, the propagation constant β varies in the range of $k_0 n_2 < \beta < k_0 n_1$, thus we define

$$\begin{aligned}\gamma_1^2 &= k_0^2 n_1^2 - \beta^2 \\ \gamma_2^2 &= \beta^2 - k_0^2 n_2^2 \\ \gamma_3^2 &= \beta^2 - k_0^2 n_3^2\end{aligned} \tag{4.40}$$

With this definition, Eq.(4.40) simplifies to

$$\begin{aligned}&\frac{d^2E_y}{dx^2} - \gamma_2^2 E_y = 0 \quad (-\infty < x \le 0) \\ &\frac{d^2E_y}{dx^2} + \gamma_1^2 E_y = 0 \quad (0 \le x \le b) \\ &\frac{d^2E_y}{dx^2} - \gamma_3^2 E_y = 0 \quad (b \le x < \infty)\end{aligned} \tag{4.41}$$

The general solution to Eq.(4.41) is

$$E_y(x) = \begin{cases} A\exp(\gamma_2 x) & (-\infty < x \le 0) \\ A\left[\cos(\gamma_1 x) + T_2 \sin(\gamma_1 x)\right] & (0 \le x \le b) \\ D\exp\left[-\gamma_3 (x-b)\right] & (b \le x < \infty) \end{cases} \tag{4.42}$$

where $T_2 = \gamma_2/\gamma_1$. Using the boundary condition, Eq.(2.51), we can get the field distribution function for TE modes

$$E_y(x) = \begin{cases} A\exp(\gamma_2 x) & (-\infty < x \le 0) \\ A\left[\cos(\gamma_1 x) + T_2 \sin(\gamma_1 x)\right] & (0 \le x \le b) \\ A\left[\cos(\gamma_1 b) + T_2 \sin(\gamma_1 b)\right]\exp\left[-\gamma_3 (x-b)\right] & (b \le x < \infty) \end{cases} \tag{4.43}$$

and the characteristic equation

$$\gamma_1 b = m\pi + \arctan T_2 + \arctan T_3 \quad (m = 0, 1, 2, \cdots) \tag{4.44}$$

where $T_3 = \gamma_3/\gamma_1$.

Similarly, the field distribution function for TM modes can be obtained as

$$H_y(x)=\begin{cases} A\exp(\gamma_2 x) & (-\infty < x \le 0) \\ A\left[\cos(\gamma_1 x)+T_2\sin(\gamma_1 x)\right] & (0 \le x \le b) \\ A\left[\cos(\gamma_1 b)+T_2\sin(\gamma_1 b)\right]\exp\left[-\gamma_3(x-b)\right] & (b \le x < \infty) \end{cases} \quad (4.45)$$

where $T_2=\left(n_1^2/n_2^2\right)(\gamma_2/\gamma_1)$, and the characteristic equation is

$$\gamma_1 b = m\pi + \arctan T_2 + \arctan T_3 \quad (m = 0,\ 1,\ 2,\cdots) \quad (4.46)$$

where $T_3=\left(n_1^2/n_2^2\right)(\gamma_3/\gamma_1)$.

In summary, the field distribution function for asymmetric three-layer slab waveguides can be expressed in the following form

$$\psi_y(x)=\begin{cases} A\exp(\gamma_2 x) & (-\infty < x \le 0) \\ A\left[\cos(\gamma_1 x)+T_2\sin(\gamma_1 x)\right] & (0 \le x \le b) \\ A\left[\cos(\gamma_1 b)+T_2\sin(\gamma_1 b)\right]\exp\left[-\gamma_3(x-b)\right] & (b \le x < \infty) \end{cases} \quad (4.47)$$

where $\psi(x)=E_y(x)$ for TE modes and $\psi(x)=H_y(x)$ for TM modes, $T_2=\left(n_1^2/n_2^2\right)^s(\gamma_2/\gamma_1)$ and $T_3=\left(n_1^2/n_2^2\right)^s(\gamma_3/\gamma_1)$ with $s=0$ for TE modes and $s=1$ for TM modes. The characteristic equation is summarized as

$$\gamma_1 b = m\pi + \arctan T_2 + \arctan T_3 \quad (m = 0,\ 1,\ 2,\cdots) \ . \quad (4.48)$$

Again, Eq.(4.48) is a transcendental equation with respect to β, which has to be solved numerically.

4.3.3 Thin Metal Film Embedded in Dielectric

The geometry of the thin metal film is shown in Figure 4.4. A metal film of variable thickness d and refractive index n_M is sandwiched by two semi-infinite dielectric layers of n_1 and n_3. We assume the structure is uniform along the direction parallel to the plane of the interface, donated by y.

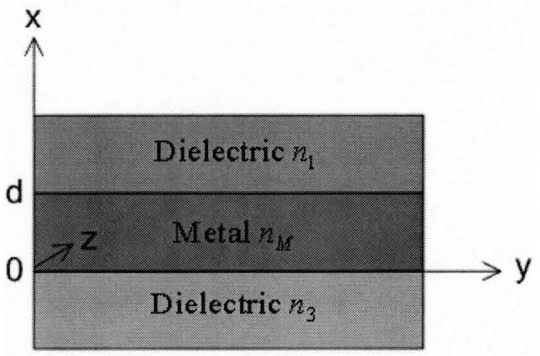

Figure 4.4 Schematics of thin metal film embedded in dielectric.

For isotropic medium, the surface polaritons waves are transverse magnetic in nature and can be described by their magnetic fields which lie in the plane of the interface and in the y direction. By imposing the boundary conditions to wave equations, the magnetic field distributions across the transverse direction are given in the following form [71]

$$H_y(x) = \begin{cases} e^{S_1 x} & x < 0 \\ \cosh(S_2 x) + \dfrac{S_1 n_M^2}{S_2 n_1^2} \sinh(S_2 x) & 0 < x < d \\ \left[\cosh(S_2 d) + \dfrac{S_1 n_M^2}{S_2 n_1^2} \sinh(S_2 d) \right] e^{-S_3 (x-d)} & x > d \end{cases} \tag{4.49}$$

where

$$\begin{aligned} S_1^2 &= \beta^2 - n_1^2 k_0^2 \\ S_2^2 &= \beta^2 - n_M^2 k_0^2 \\ S_3^2 &= \beta^2 - n_3^2 k_0^2 \end{aligned} . \tag{4.50}$$

Solving the boundary condition for the tangential field components leads to the dispersion relation

$$\tanh(S_2 d)(n_1^2 n_3^2 S_2^2 + n_M^2 S_1 S_3) + \left[S_2 (n_1^2 S_3^2 + n_3^2 S_1^2) n_M^2 \right] = 0 . \tag{4.51}$$

The complex propagation constant $\beta = \beta_R - j\beta_I$ can be obtained by solving the transcendental equation (4.51) with the well-known Newton method. The imaginary part of β indicates the absorption loss by metals.

4.4 Numerical Methods

Although analytical solutions to 1D wave equations exist, different derivations are required for different structures (e.g. three-layer, four-layer, and multilayer structures) in order to find the analytical solutions. Alternatively, 1D wave equations can be solved numerically by replacing the second derivatives with their finite-difference expressions.

In this numerical method, solving the partial differential equations transforms to solving an eigenvalue problem regardless of structure geometry. What we need to adjust for different structures is just the refractive index profile. In this respect, numerical methods are more universal than analytical methods in solving 1D wave equations. Analytical methods are no longer available for 2D wave equations which involve two-dimensional confinement on waveguide cross sections. Mode solving for 2D structures has to rely on numerical methods. Therefore, numerical methods play an extremely important role in mode solving techniques and have been widely used in various commercial mode solvers.

As we discussed in chapter 3, finite-difference formulas for second derivatives can greatly affect the efficiency and accuracy of the FDM. Although various FD formulas have been assessed therein, their roles in solving partial differential wave equations have not been seen so far. In this section, we will solve the 1D wave equations using the conventional central difference scheme and the vectorial fourth-order FD formula. The advantage of high-order FD formulas in mode solving techniques will be demonstrated in a number of numerical examples.

4.4.1 Implementation

The 1D wave equations we need to solve are

$$\frac{d^2E_y}{dx^2}+\left(k_0^2n^2-\beta^2\right)E_y=0 \tag{4.52}$$

for TE modes and

$$n^2 \frac{\partial}{\partial x}\left(\frac{1}{n^2}\frac{\partial H_y}{\partial x}\right)+\left(k_o^2 n^2-\beta^2\right)H_y=0 \tag{4.53}$$

for TM modes. Note that the TM wave equation (4.53) is written in a universal form.

A. Central Difference Scheme

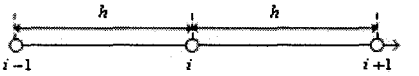

Figure 4.5 Uniform discretization for the FDM.

Figure 4.5 shows a uniform discretization in the 1D structure. By using the central difference scheme, the second derivative in Eq.(4.52) can be expressed in the following finite-difference form

$$\frac{d^2E_y}{dx^2}=\frac{E_y(i-1)-2E_y(i)+E_y(i+1)}{h^2}. \tag{4.54}$$

The Eq.(4.52) is thus discretized into a matrix eigenvalue equation such as

$$A\Phi=\beta^2\Phi \tag{4.55}$$

where Φ is a vector formed with the unknown $E_y(i)$ values and where A is a tridiagonal matrix. Figure 4.6 shows the general form of a tridiagonal matrix.

$$A=\begin{bmatrix} a_{11} & a_{12} & 0 & 0 \\ a_{21} & a_{22} & \ddots & 0 \\ 0 & \ddots & \ddots & a_{n-1,n} \\ 0 & 0 & a_{n,n-1} & a_{nn} \end{bmatrix}$$

Figure 4.6 General form of tridiagonal matrix.

The matrix A is composed of three vectors, namely, vectors on maindiagonal, subdiagonal and superdiagonal. The elements in these three vectors are

$$\begin{aligned} \text{subdiagonal} &= \left\{\frac{1}{h^2}\right\} \\ \text{maindiagonal} &= \left\{k_0^2 n^2(i) - \frac{2}{h^2}\right\}. \\ \text{superdiagonal} &= \left\{\frac{1}{h^2}\right\} \end{aligned} \tag{4.56}$$

The eigenvalue problem in Eq.(4.55) can be solved efficiently by the shifted-inverse power method [72]. The eigenvalue corresponds the square of the propagation constant β^2 and the eigenvector corresponds the field distribution function E_y.

The second derivative in TM wave equation (4.53) contains refractive index terms, so its FD expression has to be derived by means of averaging the index over meshes as follows

$$\begin{aligned} n^2 \frac{\partial}{\partial x}\left(\frac{1}{n^2}\frac{\partial H_y}{\partial x}\right) &= \frac{n^2(i)}{h}\left(\frac{1}{n^2}\frac{\partial H_y}{\partial x}\bigg|_{i+1/2} - \frac{1}{n^2}\frac{\partial H_y}{\partial x}\bigg|_{i-1/2}\right) \\ &= \frac{n^2(i)}{h}\left(\frac{1}{n^2(i+1/2)}\frac{H_y(i+1)-H_y(i)}{h} - \frac{1}{n^2(i-1/2)}\frac{H_y(i)-H_y(i-1)}{h}\right) \\ &= \frac{n^2(i)}{h^2}\left(\frac{2}{n^2(i)+n^2(i+1)}\Big[H_y(i+1)-H_y(i)\Big] - \frac{2}{n^2(i)+n^2(i-1)}\Big[H_y(i)-H_y(i-1)\Big]\right) \\ &= \frac{a_i H_y(i+1) - 2b_i H_y(i) + c_i H_y(i-1)}{h^2} \end{aligned} \tag{4.57}$$

where

$$a_i = \frac{2n^2(i)}{n^2(i)+n^2(i+1)} \tag{4.58}$$

$$b_i = \frac{n^2(i)}{n^2(i)+n^2(i+1)} + \frac{n^2(i)}{n^2(i)+n^2(i-1)}. \tag{4.59}$$

$$c_i = \frac{2n^2(i)}{n^2(i)+n^2(i-1)} \tag{4.60}$$

Thus, the elements in matrix A for TM wave equation (4.53) are

$$\begin{aligned} \text{subdiagonal} &= \left\{\frac{c_i}{h^2}\right\} \\ \text{maindiagonal} &= \left\{k_0^2 n^2(i) - \frac{2b_i}{h^2}\right\}. \\ \text{superdiagonal} &= \left\{\frac{a_i}{h^2}\right\} \end{aligned} \tag{4.61}$$

Similarly, the propagation constant β and the field distribution function H_y can be found by solving the eigenvalue problem.

B. Vectorial Fourth-Order FD Formula

Under this formulation, the 1D wave equations can be expressed in the following Helmholtz equation

$$\frac{d^2\Phi}{dx^2} + \left(k_0^2 n^2 - \beta^2\right)\Phi = 0 \tag{4.62}$$

where $\Phi = E_y$ for TE mode and $\Phi = H_y$ for TM mode. Substituting the vectorial fourth-order FD formula (3.33) into the Helmholtz equation leads to

$$\frac{D_x^2 \Phi_i}{1 + g_1 D_x + g_2 D_x^2} + k_0^2 n^2 \Phi_i = \beta^2 \Phi_i \tag{4.63}$$

or

$$D_x^2 \Phi_i + k_0^2 n^2 \left(1 + g_1 D_x + g_2 D_x^2\right)\Phi_i = \beta^2 \left(1 + g_1 D_x + g_2 D_x^2\right)\Phi_i. \tag{4.64}$$

It should be noted that Eq.(4.62) does not contain the refractive index term. The dielectric interface conditions between different refractive indices are included in the coefficients of the FD formula. Moreover, by adjusting the coefficients shown in Table 3.1, the modal solutions to both TE and TM modes can be easily obtained.

Combining all sampled points together from Eq.(4.64), we get the following generalized eigenvalue problem

$$A'\Phi = \beta^2 C\Phi \tag{4.65}$$

Where $A' = A + k_0^2 N^2 (C - I), N^2 = diag(n_1^2, n_2^2, \cdots n_j^2, \cdots)$, A results from the operator $D_x^2 + k_0^2 n^2$, C results from the operator $\left(1 + g_1 D_x + g_2 D_x^2\right)$, and I is an identity matrix. It is worth mentioning that the matrices A, C and A' are all tridiagonal. Accordingly, the eigenvalue problem (4.65) can be solved efficiently.

4.4.2 Numerical Results

We show the advantage of the fourth-order FD formulas in solving the mode of dielectric slab waveguides. The investigated structure is a three-layer symmetric slab waveguide with high index contrast. The core and cladding indices are $n_{core} = 3.5$ and $n_{clad} = 1.5$, respectively. The core width is $2a = 0.1$ μm and the wavelength is $\lambda = 1.55$ μm. We numerically solve the modes of this structure by using the central difference scheme and the vectorial fourth-order FD formula. The availability of analytical solutions to this structure allows us to evaluate these two FD formulas. We choose the assessment

criteria as the relative error of the propagation constant of the fundamental mode, defined as

$$\varepsilon = \frac{\left|\beta_{analytical} - \beta_{numerical}\right|}{\beta_{analytical}}. \tag{4.66}$$

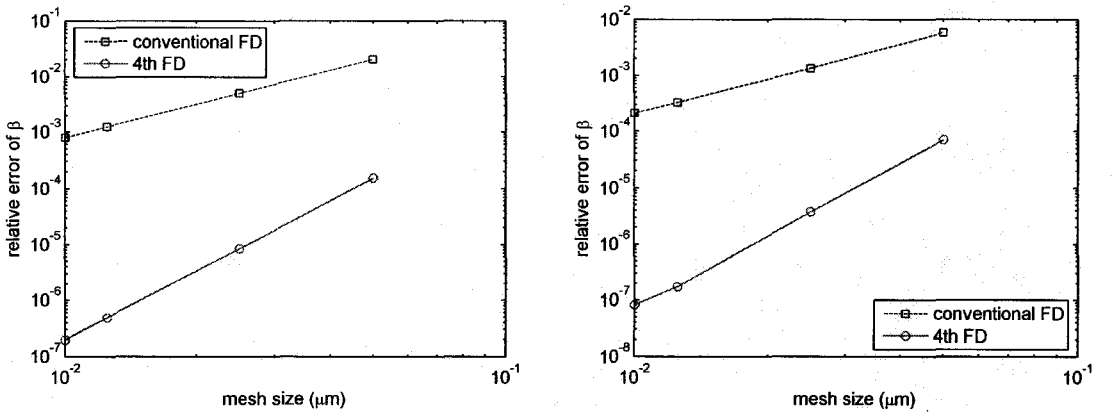

(a) (b)

Figure 4.7 Relative error in the propagation constant as a function of mesh size. (a) TE; (b) TM. "conventional FD" represents the conventional central difference scheme and "4th FD" represents the vectorial fourth-order FD formula.

Figure 4.7(a) and (b) shows the relative error of the propagation constant of the fundamental mode as a function of mesh size for TE and TM modes, respectively. The dashed blue curve corresponds the results calculated using the conventional central difference scheme, denoted by "conventional FD" and the solid red curve corresponds the results calculated using the vectorial fourth-order FD formula, denoted by "4th FD". It can be seen that the results based on "4th FD" are always more accurate than those based on "conventional FD" for a fixed mesh size. Moreover, the convergence rate of "4th FD" is much faster than the "conventional FD", which reveals the higher-order property of

"4th FD". The significant improvement in the accuracy is attributed to the higher-order Taylor series expansion and the rigorous treatment of interface condition.

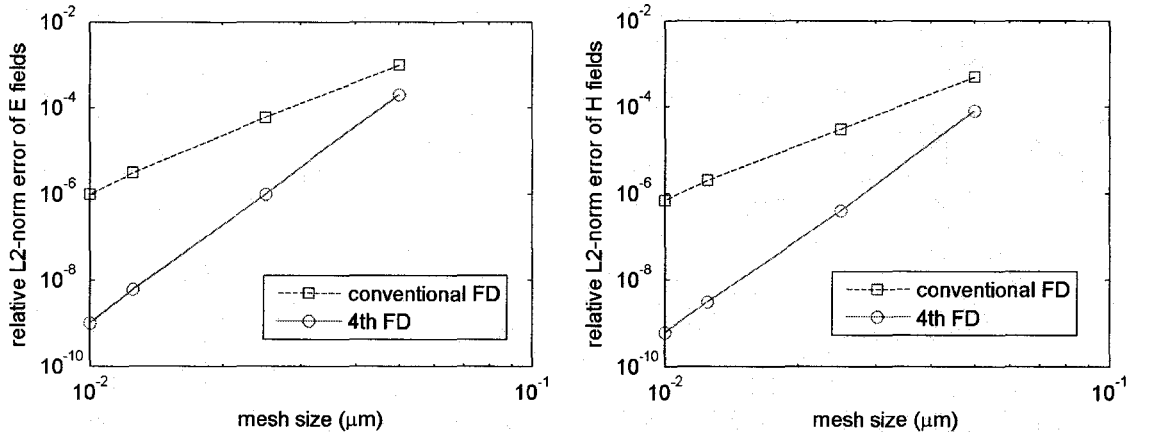

(a) (b)

Figure 4.8 Relative L2-norm errors of the calculated fields as a function of mesh size. (a) TE; (b) TM. "conventional FD" represents the conventional central difference scheme and "4th FD" represents the vectorial fourth-order FD formula.

Figure 4.8 shows the relative L2-norm error of the calculated field as a function of mesh size for both TE and TM modes. The field values calculated by analytical method are used as the benchmark. Again, it is found that the fields calculated from the "4th FD" are more accurate than those calculated from the "conventional FD".

4.5 High-Order Mode Solving Techniques for Bent Waveguides

In the last section, we have demonstrated the superiority of high-order FD formulas over the conventional difference scheme in solving the modes of straight waveguides. We will investigate the characteristics of bent dielectric waveguides using

the high-order FDM in this section. Since our concern is high index contrast waveguides with fine geometries, the high-order mode solving technique is particularly desired for accurate and efficient analysis.

There are two popular numerical models for analysis of bend waveguides, namely, the conformal transformation method [68] and the cylindrical coordinate system formulation [70]. Here, we introduce the high-order FD formula to the conformal transformation method.

4.5.1 Conformal Transformation Method

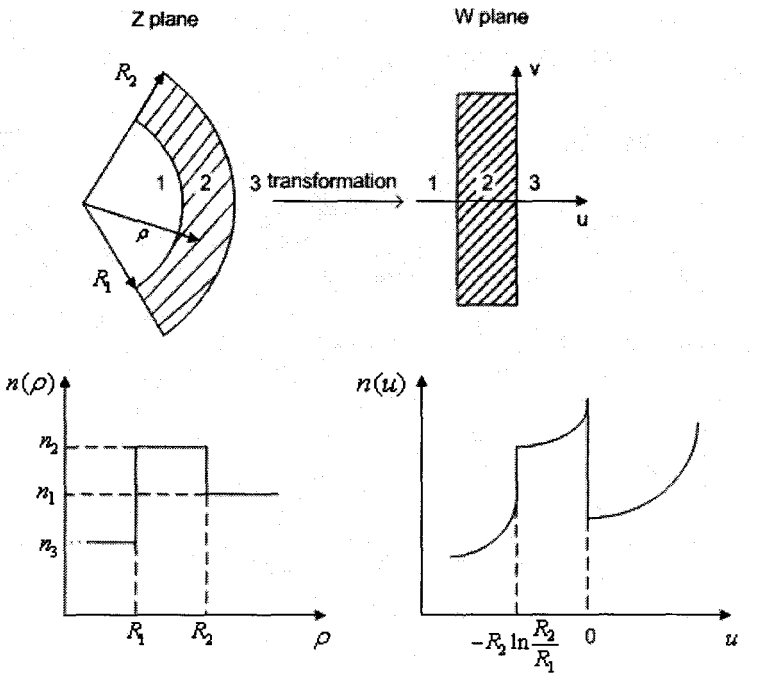

(a) (b)

Figure 4.9 (a) A waveguide bend with step-index distribution; (b) its transformation.

The conformal transformation provides a method for converting the curved waveguides to the equivalent straight waveguides which can be readily analyzed by the standard mode solvers. The objective of the transformation is to select an analytical function $f(Z)$ that converts the curved boundaries in the x, y plane to straight ones in the u, v plane. The transformation is intuitively illustrated in Figure 4.9. Figure 4.9(a) shows a circularly curved dielectric waveguide with a step discontinuity in refractive index at radii R_1 and R_2. Using the conformal transformation

$$W = R_2 \ln(Z/R_2), \tag{4.67}$$

we obtain an equivalent straight waveguide shown in Figure 4.9(b). Its refractive index profile is

$$n(u) = \begin{cases} n_1 \exp(\frac{u}{R_2}) & u < -R_2 \ln(\frac{R_2}{R_1}) \\ n_2 \exp(\frac{u}{R_2}) & -R_2 \ln(\frac{R_2}{R_1}) < u < 0 \\ n_3 \exp(\frac{u}{R_2}) & u > 0 \end{cases}. \tag{4.68}$$

It is clear that all of the modes of the equivalent structure will radiate to the right where the refractive index exceeds the maximum refractive index in the core. The mode solver based on the vectorial fourth-order FD formula can be directly applied to the transformed structure.

4.5.2 Numerical Results

The characteristics of a symmetric bent waveguide are investigated by the high-order mode solver based on conformal transformation method. The indices of the core and cladding layers are denoted by n_1 and n_2, respectively. The wavelength is $\lambda = 1.55$ μm. We choose the core width $2d$ according to the following relation

$$\frac{\lambda}{2d} > 2\sqrt{2}\,\bar{n}\sqrt{\Delta} \tag{4.69}$$

where $\bar{n} = \frac{n_1 + n_2}{2}$ and $\Delta = \frac{n_1 - n_2}{\bar{n}}$, such that the single mode condition is satisfied. Figure 4.10 shows the single mode condition for symmetric slab waveguides with different refractive index contrast. As illustrated in Figure 4.10, the core width shrinks with increasing the refractive index contrast under the single mode condition. Accordingly, compact integrated photonic circuits can be achieved by using high index contrast waveguides.

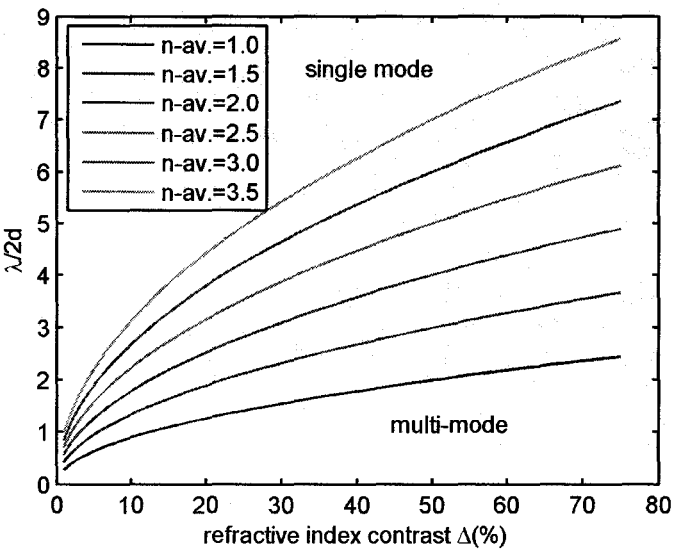

Figure 4.10 Single mode condition for symmetric slab waveguides. n-av. represents $\bar{n}$.

Bent waveguides with high index contrast are particularly useful for high integration, because their bending radius can be considerably decreased. However, it is well-known that the bending loss increases as the bending radius decreases. Therefore, it is essential to know the minimum bending radius given the acceptable maximum bending loss. The minimum bending radius is defined as the radius for a pre-defined maximum bending loss such that

$$R = R_{\min} \tag{4.70}$$

when $\alpha(R_{\min}) = \alpha_{\max}$ (α is bending loss). The bending loss can be calculated from the imaginary part of the propagation constant. Figure 4.11 shows the minimum bending radius as a function of the refractive index contrast provided that the maximum bending loss is 0.5 dB/cm. The maximum core width under the single mode condition is also shown in the same figure.

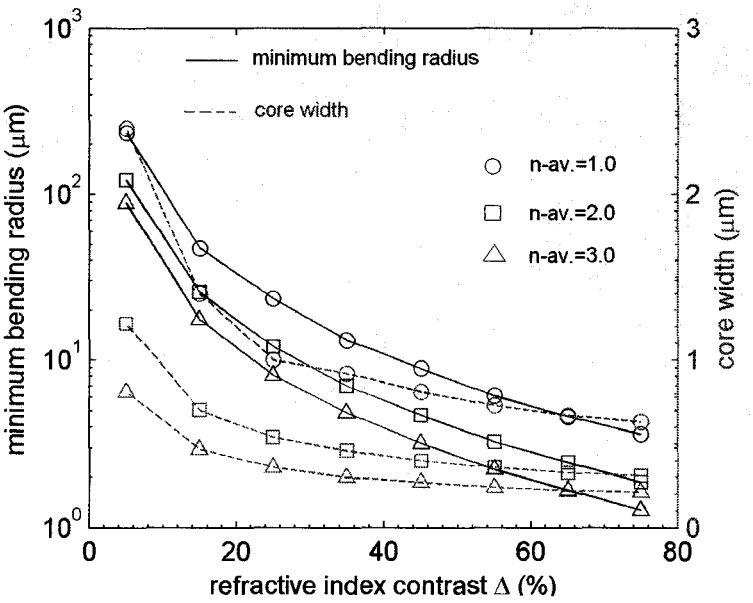

(a)

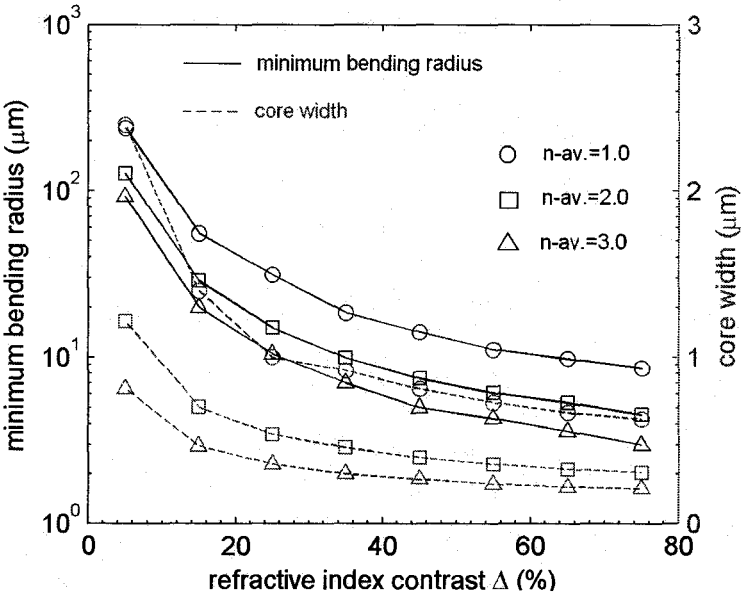

(b)

Figure 4.11 Minimum bending radius and maximum core width as a function of refractive index contrast for $\bar{n} = 1.0$, 2.0, and 3.0. (a) TE; (b) TM.

It can be seen that the minimum bending radius decreases with increasing the refractive index contrast. This is an attractive feature because a small bending radius can be achieved for high index contrast waveguides.

It is also important to know the confinement factor of bent waveguides, which describes the portion of the power confined in the guiding layer. The confinement factor is defined as

$$\Gamma_{TE} = \frac{\int_{-d}^{+d} |E_y|^2 dx}{\int_{-\infty}^{+\infty} |E_y|^2 dx} \tag{4.71}$$

for TE mode and

$$\Gamma_{TM} = \frac{\int_{-d}^{+d} \Re\left\{\frac{1}{n^2}\right\} |H_y|^2 \, dx}{\int_{-\infty}^{+\infty} \Re\left\{\frac{1}{n^2}\right\} |H_y|^2 \, dx} \tag{4.72}$$

for TM mode. Figure 4.12 shows the confinement factor as a function of the refractive index contrast. The confinement factor in each case is calculated using the corresponding minimum bending radius, which is also shown in the same figure.

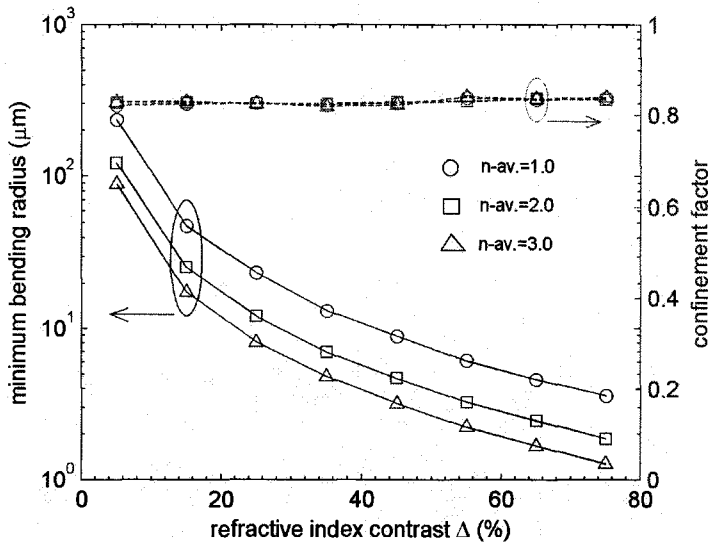

(a)

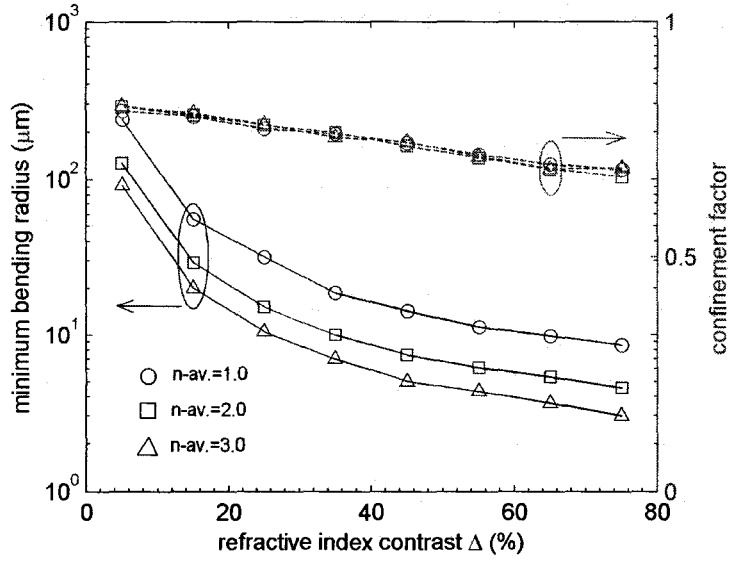

(b)

Figure 4.12 Confinement factor and minimum bending radius as a function of refractive index contrast for $\bar{n} = 1.0$, 2.0, and 3.0. (a) TE; (b) TM.

It is found that, in the case of minimum bending radius, the confinement factor does not vary with the refractive index contrast for TE modes, but slightly decreases with increasing the refractive index contrast for TM modes. This implies that the small bending radius and high confinement factor can be achieved simultaneously for high index contrast bent waveguides.

Finally, the polarization effects of bent waveguides are investigated by the high-order mode solver. Both the birefringence and the confinement difference are calculated. The birefringence is defined as

$$B = \frac{n_{eff}^{TE} - n_{eff}^{TM}}{n_{eff}^{TE} + n_{eff}^{TM}}. \tag{4.73}$$

The confinement difference is defined as

$$D = \frac{\Gamma_{TE} - \Gamma_{TM}}{\Gamma_{TE} + \Gamma_{TM}}. \tag{4.74}$$

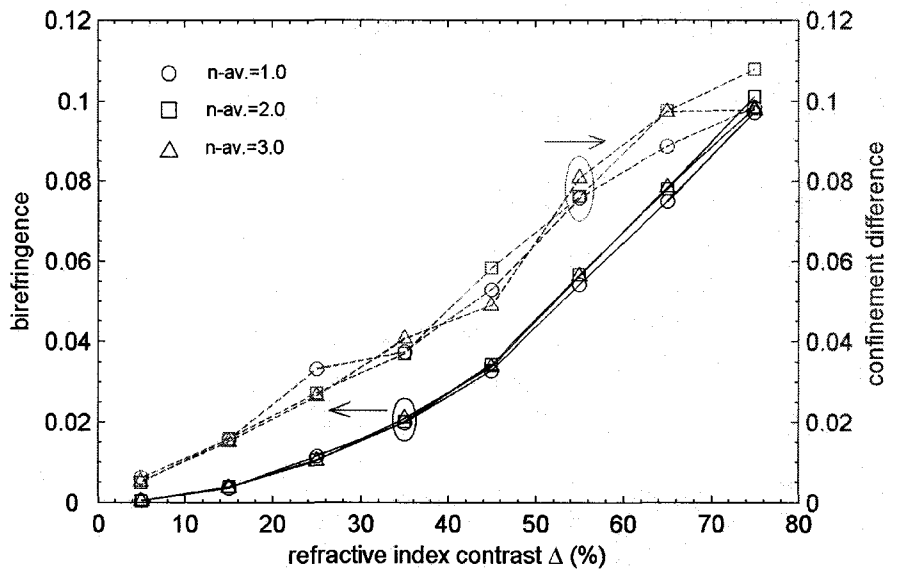

Figure 4.13 Polarization effects as a function of refractive index contrast for $\bar{n} = 1.0$, 2.0, and 3.0.

Figure 4.13 shows the birefringence and confinement difference as functions of refractive index contrast. It can be seen that the polarization effects of bent waveguides become stronger as the refractive index contrast increases. Therefore, the bent waveguides with high index contrast can find applications in optical devices utilizing polarization effects.

4.6 Summary

In this chapter, we first derive the analytical solutions to one-dimensional wave equations for three-layer dielectric slab waveguides and plasmonic waveguides based on thin metal film embedded in dielectric. The one-dimensional wave equations are then solved numerically based on the conventional central difference scheme and vectorial fourth-order FD formula. By comparing with analytical solutions, it is demonstrated that the vectorial fourth-order FD formula has the obvious advantage in accuracy in solving the modes of high index contrast dielectric waveguides.

Finally, the high-order mode solving technique is applied to the analysis of bent waveguides with the help of conformal transformation. Important characteristics of waveguide bends with high index contrast, such as bending loss, minimum bending radius, confinement factor and polarization dependence are investigated.

Chapter 5
High-Order Finite-Difference Beam Propagation Method (BPM)

5.1 Introduction

Beam propagation method (BPM) based on finite-difference (FD) schemes is one of the most popular numerical techniques for simulation of electromagnetic field propagation in optical waveguides and photonic integrated circuits. The wide-spread acceptance and application of the FD-based BPM are primarily due to its relative ease of mesh implementation in comparison with other methods such as the finite element methods (FEM) [73]. It is well-known that one of the main limiting factors for the accuracy of the FD-BPM arises from the finite difference schemes for the second-order derivatives in the transverse direction. The conventional central differencing [44] is of second-order in the transverse mesh discretization (i.e., Δx and Δy). Several improved formulations with lower truncation errors have been derived for the optical waveguide mode solvers [49]-[52]. Parallel development has also occurred to the beam propagation methods, where most of the applications of high-order FD formulas have been restricted to the paraxial approximations [55][56].

Yamauchi *et al.* first introduced the Douglas scheme to a wide-angle FD-BPM [74][75] in which the truncation error is reduced to the fourth order for the case of

graded-index waveguides. The discussion is limited to the TE polarization only. Vassallo formulated a wide-angle algorithm based on high-order formulas by using Taylor series expansions to approximate the exponential function of the square root operator [76][77]. The treatment of discontinuities in the refractive index results in the second-order accurate FD formula even at the discontinuities as long as the index interfaces lie midway between the adjacent grid points. Hadley proposed a quasi-fourth-order scheme [57] for step-index waveguides in which the grid points coincide with the dielectric boundary, and applied this scheme for the wide-angle beam propagation using the Padé (1,1) approximation [30]. The higher-order field derivatives are evaluated through the Helmholtz propagation equation and complex averaging techniques. So far, no attempt has been made to generalize the wide-angle algorithm to the ultra wide-angle propagation schemes involving higher-order Padé approximation.

In this chapter, by taking advantage of the Padé approximation to the square root operator [78], we have successfully incorporated the vectorial fourth-order FD formula into an ultra-wide-angle scheme based on Padé series expansion. In the case of 2D waveguide structures, the high-order FD discretization and the implementation of the PML numerical boundary conditions [26] lead to a tridiagonal matrix and can be readily solved. Both TE and TM polarizations are considered for waveguide structures with high index contrast and/or ultra-wide angle propagation. For the sake of comparison, the conventional central-differencing scheme and several other high-order finite-difference formulas are also incorporated into the BPM and their scope of validity and degree of accuracy are accessed in a systematic fashion.

5.2 One-Way Wave Equations

For the sake of simplicity, we confine our discussions to two-dimensional structures. If the refractive index varies slowly along z (the propagation direction), the governing Helmholtz equation in terms of the transverse electric fields can be derived from Eqs.(2.32) and (2.33), expressed as

$$\left(\frac{\partial^2}{\partial z^2}+P\right)E=0 \tag{5.1}$$

where E represents E_y for TE polarization (y polarized transverse E field) or E_x for TM polarization (x polarized transverse E field), and the operator P is defined as

$$P=\begin{cases}\dfrac{\partial^2}{\partial x^2}+k_0^2n^2 & \text{TE polarization}\\ \dfrac{\partial}{\partial x}\left[\dfrac{1}{n^2}\dfrac{\partial\left(n^2\cdot\right)}{\partial x}\right]+k_0^2n^2 & \text{TM polarization}\end{cases} \tag{5.2}$$

where k_0 is the vacuum wave vector and $n=n(x,z)$ is the refractive index of the medium. The time dependence of the field is assumed to be $e^{j\omega t}$. By assuming the wave propagates along $+z$ direction, the field $E(x,z)$ can be expressed as

$$E(x,z)=\Psi(x,z)e^{-jk_0n_0z} \tag{5.3}$$

where $\Psi(x,z)$ represents the slow varying field and n_0 is the reference refractive index. Substituting Eq.(5.3) into (5.1), we obtain the one-way wave equation written in terms of the slow varying field

$$\frac{\partial^2 \Psi}{\partial z^2} - j2k_0 n_0 \frac{\partial \Psi}{\partial z} + k_0^2 n_0^2 \bar{P}\Psi = 0 \tag{5.4}$$

where the operator $\bar{P}$ takes the form of

$$\bar{P} = \begin{cases} \dfrac{1}{k_0^2 n_0^2}\left[\dfrac{\partial^2}{\partial x^2} + k_0^2\left(n^2 - n_0^2\right)\right] & \text{TE} \\ \dfrac{1}{k_0^2 n_0^2}\left\{\dfrac{\partial}{\partial x}\left[\dfrac{1}{n^2}\dfrac{\partial\left(n^2 \cdot\right)}{\partial x}\right] + k_0^2\left(n^2 - n_0^2\right)\right\} & \text{TM} \end{cases}. \tag{5.5}$$

5.2.1 Paraxial Wave Equations

If the variation of Ψ with z is sufficiently slow so that the following slowly-varying envelope approximation is applicable

$$\left|2k_0 n_0 \frac{\partial \Psi}{\partial z}\right| \square \left|\frac{\partial^2 \Psi}{\partial z^2}\right|, \tag{5.6}$$

the second-order derivative term $\dfrac{\partial^2 \Psi}{\partial z^2}$ can be neglected. Thus, Eq.(5.4) reduces to

$$2jk_0 n_0 \frac{\partial \Psi}{\partial z} = P\Psi . \tag{5.7}$$

The above equation is referred to the paraxial wave equation. Note that Eq.(5.7) is a first-order ordinary differential equation, its general solution can be expressed as

$$\Psi(z + \Delta z) = \exp\left(-j\frac{P}{2k_0 n_0}\Delta z\right)\Psi(z) . \tag{5.8}$$

By introducing the Crack Nicholson scheme to the exponential function, i.e.,

$$\exp(x) = \frac{1 + x/2}{1 - x/2} \tag{5.9}$$

Eq.(5.8) becomes

$$\left(1+\frac{jk_0n_0\Delta z}{4}P\right)\Psi(z+\Delta z)=\left(1-\frac{jk_0n_0\Delta z}{4}P\right)\Psi(z). \tag{5.10}$$

Applying the vectorial fourth-order FD formula to the above equation gives

$$\begin{aligned}&\Psi(z+\Delta z)+\frac{jk_0n_0\Delta z}{4}\left[\frac{D_x^2\Psi(z+\Delta z)}{1+g_1D_x+g_2D_x^2}+k_0^2\left(n^2-n_0^2\right)\Psi(z+\Delta z)\right]\\&=\Psi(z)+\frac{jk_0n_0\Delta z}{4}\left[\frac{D_x^2\Psi(z)}{1+g_1D_x+g_2D_x^2}+k_0^2\left(n^2-n_0^2\right)\Psi(z)\right]\end{aligned}. \tag{5.11}$$

As a result, we obtain the finite-difference form of the paraxial wave equation

$$c_{i-1}^{l+1}\Psi_{i-1}^{l+1}+c_i^{l+1}\Psi_i^{l+1}+c_{i+1}^{l+1}\Psi_{i+1}^{l+1}=c_{i-1}^{l}\Psi_{i-1}^{l}+c_i^{l}\Psi_i^{l}+c_{i+1}^{l}\Psi_{i+1}^{l} \tag{5.12}$$

where the coefficients can be found in Appendix B. It should be noted that the above matrix equation is still tridiagonal, although the high-order FD scheme is used instead of the conventional central difference scheme. The tridiagonal matrix equation can be efficiently solved by the Thomas algorithm.

5.2.2 Wide-Angle Wave Equations

The paraxial wave equation assumes that the envelope function Ψ varies slowly with z. However, when fields propagate off the axis, the slowly-varying envelope approximation is no longer valid and hence the propagating fields can not be accurately predicted from the paraxial wave equation. Furthermore, a reference refractive index must be assumed in the paraxial algorithm. The choice of the reference index is critical for the accuracy of the numerical solutions. To determine the optimum reference index is cumbersome and difficult in practical applications. In order to remove these limitations, we need to solve the one-way wave equation (5.4) directly. Eq.(5.4) can be reduced to

$$\frac{\partial \Psi}{\partial z} = -jk_0 n_0 \left(\sqrt{1+\bar{P}} - 1\right)\Psi . \tag{5.13}$$

Note that Eq.(5.13) contains the square root operator which is not amendable to direct numerical solution without rationalization. In this respect, several approaches have been proposed to resolve this problem in both underwater acoustics [78][79] and integrated optics [30], [80][81]. Since the emphasis of this chapter is the application of the high-order FD formulas to the ultra wide-angle scheme, we employ the efficient multi-step method based on the Padé series approximation [82].

Given the field at the propagation distance z, the analytical solution of Eq.(5.13) at $z + \Delta z$ is

$$\Psi(z+\Delta z) = \exp\left[-jk_0 n_0 \Delta z(\sqrt{1+\bar{P}} - 1)\right]\Psi(z). \tag{5.14}$$

The square root operator on the right side of Eq.(5.14) is approximated by [82]

$$\sqrt{1+\mathrm{X}} \approx 1 + \sum_{k=1}^{m} \frac{a_{k,m}\mathrm{X}}{1+b_{k,m}\mathrm{X}} \tag{5.15}$$

where

$$a_{k,m} = \frac{2}{2m+1}\sin^2\left(\frac{k\pi}{2m+1}\right) \tag{5.16}$$

$$b_{k,m} = \cos^2\left(\frac{k\pi}{2m+1}\right). \tag{5.17}$$

The multi-step scheme is achieved by rewriting Eq.(5.14) as

$$\Psi(z+\Delta z) = \exp\left(-jk_0 n_0 \Delta z \sum_{k=1}^{m} \frac{a_{k,m}\bar{P}}{1+b_{k,m}\bar{P}}\right)\Psi(z) = \prod_{k=1}^{m} \exp(-jk_0 n_0 \Delta z \frac{a_{k,m}\bar{P}}{1+b_{k,m}\bar{P}})\Psi(z) \tag{5.18}$$

from which the kth step takes the form

$$\Psi[z+k\Delta z/m]=\exp(-jk_0n_0\Delta z\frac{a_{k,m}\bar{P}}{1+b_{k,m}\bar{P}})\Psi[z+(k-1)\Delta z/m]. \tag{5.19}$$

With the Crank-Nicholson scheme [83] for the exponential function, we obtain the following approximate equation in which only the transverse differential operator is retained

$$\Psi[z+k\Delta z/m]=\frac{1+\tau_{k,m}\bar{P}}{1+\tau^*_{k,m}\bar{P}}\Psi[z+(k-1)\Delta z/m] \tag{5.20}$$

where

$$\tau_{k,m}=b_{k,m}-\frac{jk_0n_0\Delta z}{2}a_{k,m}. \tag{5.21}$$

Again, applying the vectorial fourth-order FD formula to Eq.(5.20) gives the following finite-difference form

$$\begin{aligned}&c_{i-1}^{l+k/m}\Psi_{i-1}^{l+k/m}+c_i^{l+k/m}\Psi_i^{l+k/m}+c_{i+1}^{l+k/m}\Psi_{i+1}^{l+k/m}\\&=c_{i-1}^{l+(k-1)/m}\Psi_{i-1}^{l+(k-1)/m}+c_i^{l+(k-1)/m}\Psi_i^{l+(k-1)/m}+c_{i+1}^{l+(k-1)/m}\Psi_{i+1}^{l+(k-1)/m}\end{aligned} \tag{5.22}$$

where the coefficients can be found in Appendix B.

5.3 Numerical Examples

In this section, we apply various FD formulas to the wide-angle and paraxial BPM. Their performance in simulation of one-way wave propagation is evaluated in a number of numerical examples.

5.3.1 Radiation of Line Source

As the first example for comparison, we simulated the radiation from a line source in free space, which propagates in all directions evenly. As such, this example provides us with an excellent opportunity to check the accuracy of the different numerical solutions intuitively and precisely. The excitation is generated by the Hankel function. Simulations are carried out based on the central differencing (CD) and the fourth-order differencing (FD4) by using the wide-angle BPM with different Padé orders. Since the refractive index is uniform, there is no difference between the true and quasi FD4 and between the CD and the FD2 schemes, respectively. As the focus of this study is on performance of the FD-based wide-angle schemes, both coarse mesh and fine mesh are used for the sake of comparison. The computation window is chosen as 20 μm, in which a PML [26] of 5 μm is placed adjacent to the edge of the window. At the edge of the window, the conventional transparent boundary condition is employed. In the simulation, we propagate the field originated from the line source along $+z$ direction for total of 10 μm with a longitudinal step size equal to $\Delta z = 0.05$ μm. The wavelength is $\lambda = 1.55$ μm.

Figures 5.1(a)-(d) show the field patterns simulated by the paraxial scheme in which the CD and the FD4 are used with coarse ($\Delta x = 0.4$ μm) and fine ($\Delta x = 0.05$ μm) meshes, respectively. It is noted that the paraxial schemes do not reproduce the correct radiation patterns as expected. Further, we see that, while the fine mesh simulations of both FD schemes yield the same results, considerable difference is noted for the coarse mesh calculations. The errors inherent in the paraxial approximation are reduced successively by increasing the Padé order in the wide-angle scheme and the simulation results of Padé (11,11) for the CD and FD4 formulas are illustrated in Figures 5.2(a)-(d)

for the coarse and fine meshes, respectively. The wide-angle BPM can produce the expected radiation patterns for the fine mesh case, whereas the FD4 is seen to be more accurate than the CD for the coarse mesh. In this sense, the high-order FD scheme does produce more accurate results than the conventional CD scheme for the ultra-wide angle BPM.

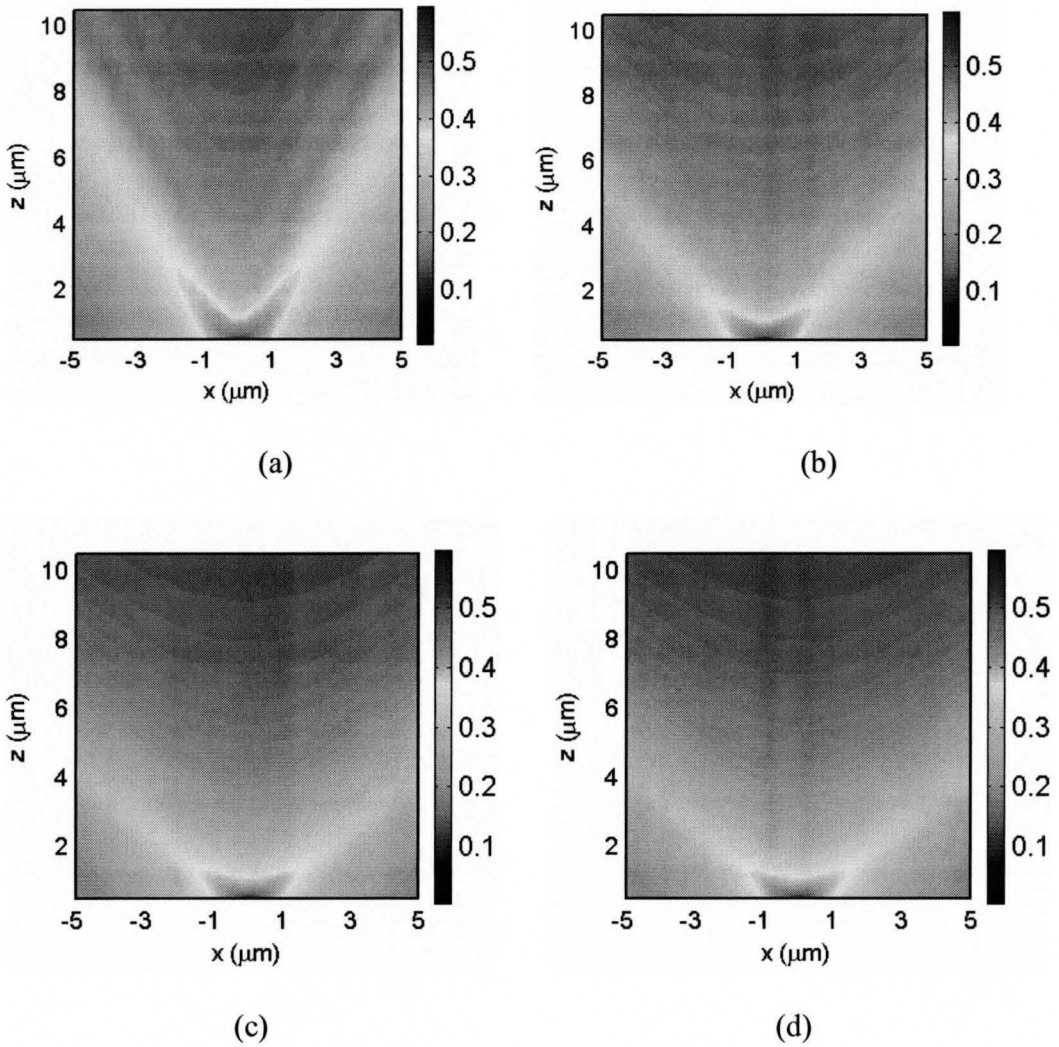

Figure 5.1 Field distributions of the radiation from a line source obtained by the paraxial BPM. (a) CD in coarse mesh; (b) FD4 in coarse mesh; (c) CD in fine mesh; (d) FD4 in fine mesh. Coarse mesh $\Delta x = 0.4$ μm, fine mesh: $\Delta x = 0.05$ μm, and longitudinal step-size: $\Delta z = 0.05$ μm.

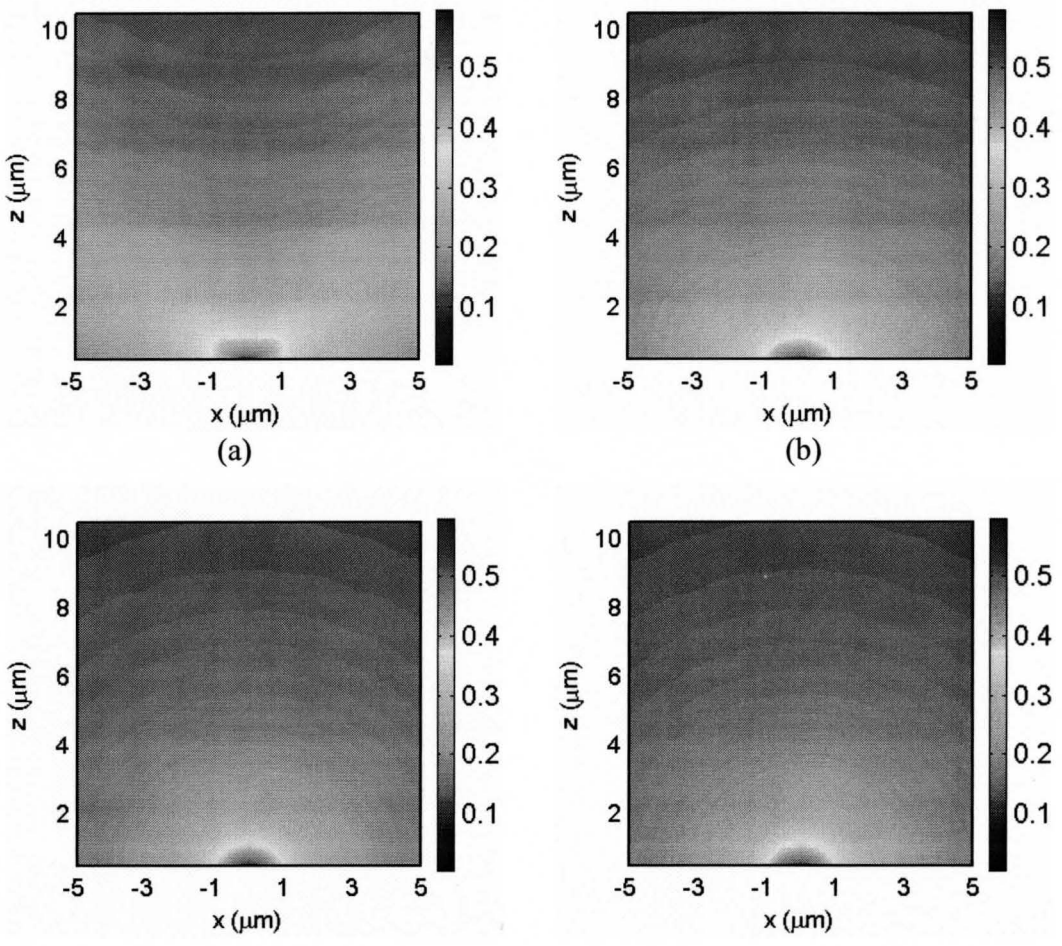

Figure 5.2 Field distributions of line source obtained by Padé (11,11) wide-angle BPM. (a) CD in coarse mesh; (b) FD4 in coarse mesh; (c) CD in fine mesh; (d) FD4 in fine mesh. The other parameters are the same as in Figure 5.1.

To gain some quantitative results for the comparison, we calculate the relative errors for the intensities and the phases of the radiation field as functions of Padé orders. The results obtained by the two differencing schemes are compared in Figure 5.3. It is observed that the relative errors decrease rapidly as the Padé order increases and become

stabilized at Padé (3,3). The conventional central differencing (CD) and the fourth-order differencing (FD4) produce similar results in the case of fine mesh ($\Delta x = 0.05$ μm). In contrast, the fourth-order difference scheme yields more accurate results than the central difference scheme when the relatively coarse mesh ($\Delta x = 0.4$ μm) is employed. This conclusion is consistent with the observation made for the field patterns in Figure 5.1 and 5.2.

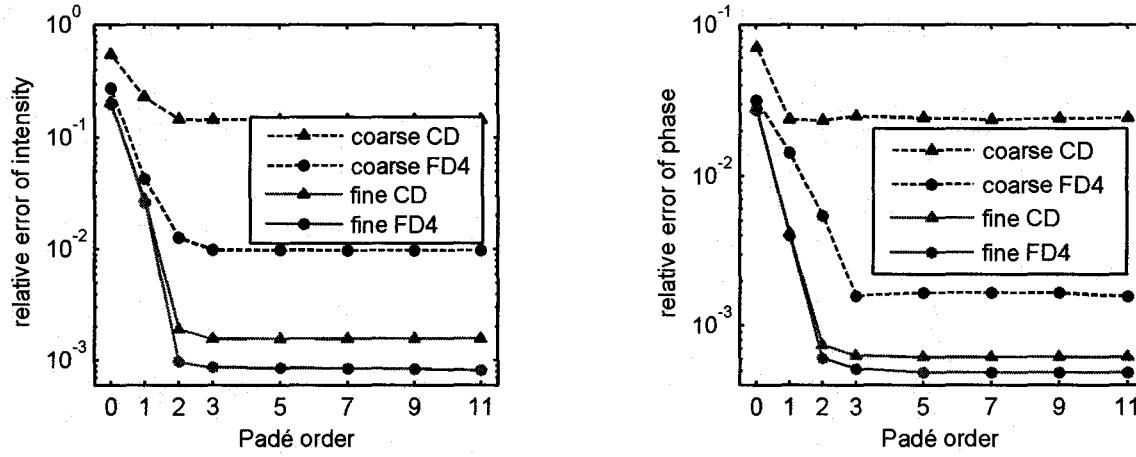

(a) (b)

Figure 5.3 The comparison of CD and FD4 for coarse and fine meshes, respectively. (a) The relative error for the intensity; (b) The relative error for the phase.

5.3.2 Step-Index Slab Waveguide with High Index Contrast

As the second example for the comparison, we consider a step-index slab waveguide. It is well known that the improper choice of reference refractive index causes severe errors in the paraxial beam propagation analysis, due to the fast phase variations in the complex field $\Psi(x,z)$. A wide-angle scheme based on Padé approximations can alleviate this problem to some degree since the second derivative of $\Psi(x,z)$ is included in

the governing equation. To assess various FD formulas, we calculate the relative errors in the propagation constants due to the fast oscillation in $\Psi(x,z)$ along z for both TE and TM polarizations by choosing n_0 to be different from the mode effective index. The relative error in the propagation constants is defined as

$$\varepsilon = \left| \frac{\beta_{calculated} - \beta_{exact}}{\beta_{exact}} \right| \tag{5.23}$$

where β_{exact} and $\beta_{calculated}$ are the exact and the numerically calculated propagation constants, respectively. $\beta_{calculated}$ can be found as follows:

$$\beta_{calculated} = k_0 n_0 + \frac{\Delta\phi}{\Delta L} \tag{5.24}$$

where $\Delta\phi$ is the phase shift and ΔL is the propagation distance. The phase shift is extracted from the overlap integral between the input and the output fields expressed as

$$\int \Psi_{output} \cdot \Psi^*_{input} dx \tag{5.25}$$

The refractive indices of the core and the cladding are $n_1 = 1.5$ and $n_2 = 1.0$, respectively. The wavelength is $\lambda = 1.0$ μm. The core width is chosen to be $D = 0.427$ μm so as to form a single-mode waveguide. The effective indices for TE and TM polarizations of this waveguide are $n_{eff} \approx 1.336$ and $n_{eff} \approx 1.2495$, respectively. The step sizes are chosen to be $\Delta x = 0.10675$ μm and $\Delta z = 0.1$ μm. The width of the computation window is $W = 5.978$ μm. The PML boundary condition is employed at the edges of the computation window. The electric fields of the fundamental mode are launched as the incident fields. Figure 5.4 shows the effects of the variation in the reference refractive index on the relative errors of

the propagation constants for the paraxial and wide-angle schemes. The results obtained using the CD scheme, vectorial second-order FD formula (FD2), and FD4 are presented in the same figure for comparison. Figure 5.4(a) and (b) are for the cases of TE and TM polarizations, respectively. For each polarization, it can be seen that the best results are obtained with the fourth-order FD formula for both paraxial and wide-angle schemes. As expected, the multi-step wide-angle scheme yields accurate results over a wider range of reference index values, compared to paraxial approximations. For each curve the best results are achieved when n_0 is chosen to be n_{eff}.

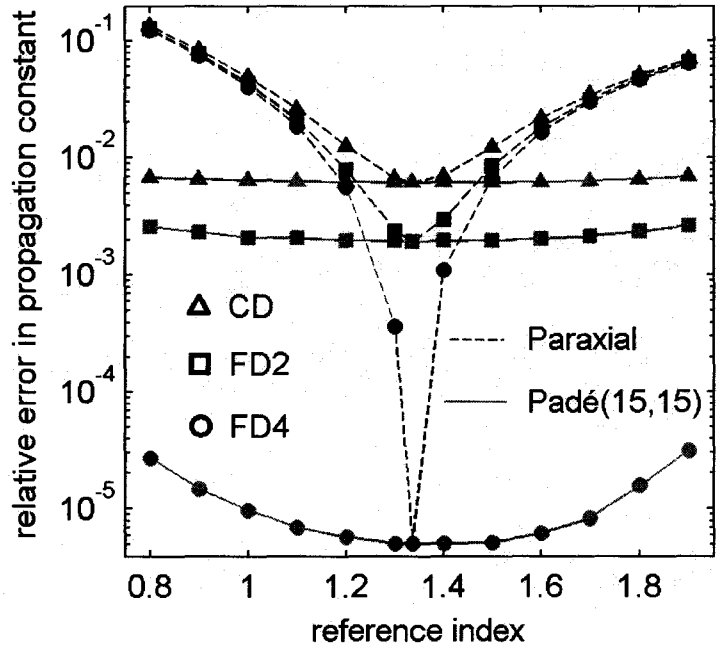

(a)

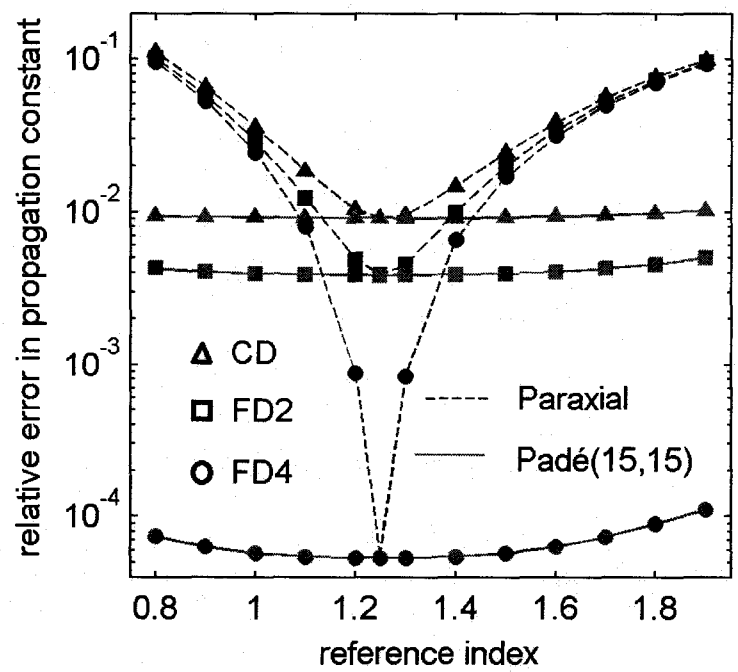

(b)

Figure 5.4 Effect of the variation in the reference index on the relative error of the propagation constant. (a) TE mode; (b) TM mode.

We now proceed to study the convergence of various FD formulas as a function of transverse step size Δx. The reference index is fixed at $n_0 = 1.8$ and other parameters are the same as in Figure 5.4. The relative errors of the propagation constant for TE and TM modes versus Δx are shown in Figure 5.5(a) and (b). In general, the discretization errors increases with the increase of Δx as illustrated in the curves corresponding to the wide-angle scheme based on CD and FD2. It should be noted that the wide-angle scheme based on FD4 maintains high accuracy even with very coarse grids. In paraxial cases, it is observed that the results obtained with various FD formulas are nearly superimposed. This indicates that the main source of error arises from the paraxial approximation.

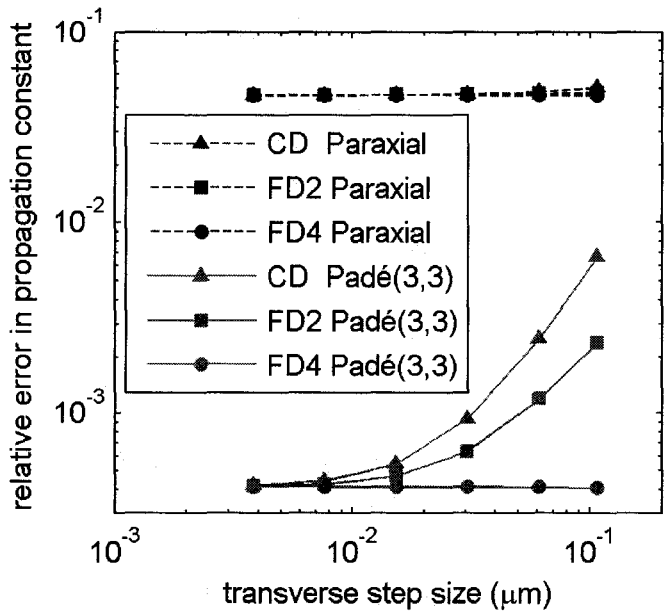

(a)

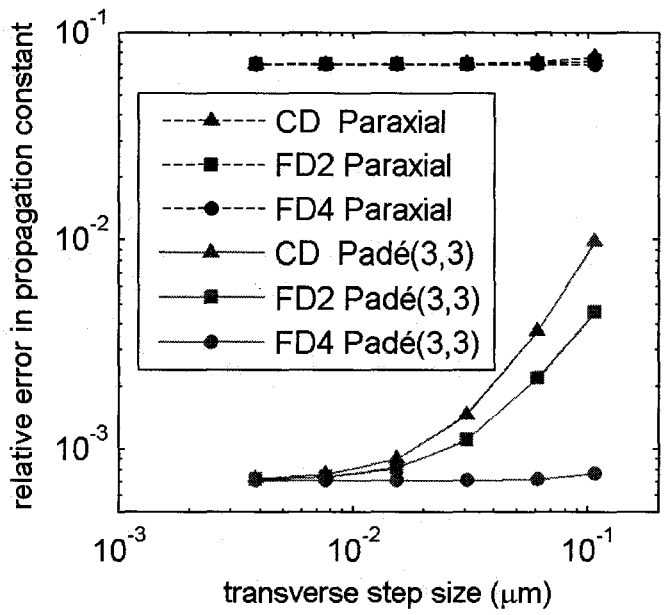

(b)

Figure 5.5 Relative error in the propagation constant as a function of the transverse step size (a) TE mode; (b) TM mode.

To emphasize the effectiveness of treatment of interface conditions, we compare the scalar fourth-order FD formula (quasi-FD4) and the true FD4 schemes based on Padé (3,3) approximation as shown in Figure 5.6 in a higher index contrast waveguide with a different core index $n_1 = 2.0$. The cladding index n_2 is fixed to be 1.0. We take $\lambda = 1.0$ μm and $D = 0.27566$ μm so that only the fundamental mode propagates. The longitudinal step size is $\Delta z = 0.1$ μm. The reference indices for TE and TM polarizations are chosen to be 1.9605 and 2.162, respectively, which are far different from their respective effective indices. For both TE and TM polarizations, the relative error of the propagation constants observed for FD4 is much smaller than that for quasi-FD4 when the coarse grids are employed. Since these two formulas are obtained from the same order Taylor series expansions, the improvement of FD4 in accuracy is contributed to the proper treatment of interface conditions.

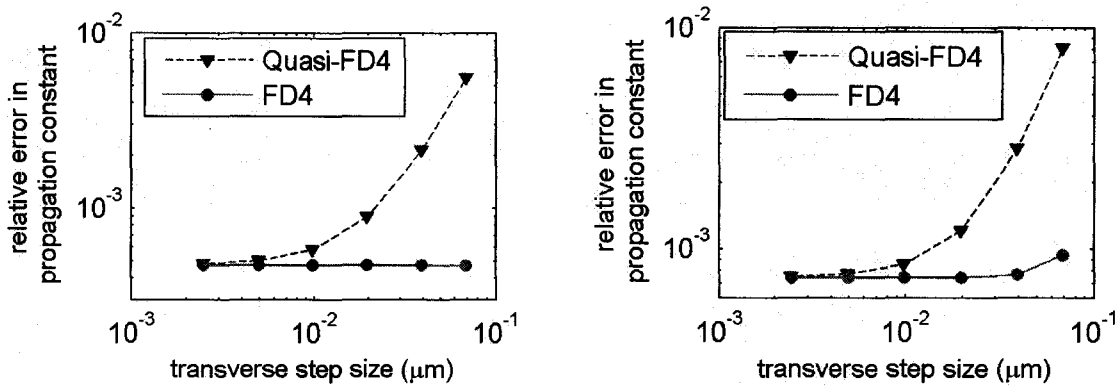

Figure 5.6 Relative error in the propagation constant as a function of the transverse step size for quasi-FD4 and true FD4. (a) TE mode; (b) TM mode.

Finally, the comparison of quasi-FD4 and true FD4 scheme is conducted by calculating the mode-mismatch loss as a function of the relative refractive index difference ($\Delta n / n_2$) between the core and cladding regions. The mode-mismatch loss is defined as

$$L_M = -10\log\left[\left|\int \Psi_0 \Psi^* dx\right|^2 \Big/ \left(\int |\Psi_0|^2 dx\right)^2\right] \tag{5.26}$$

where Ψ is the propagating field and Ψ_0 is the incident field of the fundamental mode. The wavelength is $\lambda = 1.0$ μm, the cladding index n_2 is 1.0, and the relative refractive index difference is set successively at $\Delta n / n_2$ = 0.002, 0.01, 0.1, and 1.0. The single-mode condition is guaranteed by choosing the waveguide width to fix the normalized frequency around 1.5. The mode-mismatch loss obtained with paraxial BPM is plotted versus $\Delta n / n_2$ in Figure 5.7 at the propagation distance of 100 μm with $\Delta z = 0.1$ μm for both coarse mesh ($\Delta x = 0.068915$ μm) and fine mesh ($\Delta x = 0.0068915$ μm). It is confirmed that the strongly guiding structures suffer larger mode-mismatch loss. In the case of fine mesh, the two FD schemes appear to converge as the guidance becomes weak. In the case of coarse mesh, big difference between the results obtained by the two schemes is observed from weak guidance to strong guidance, which indicates that the FD4 scheme is able to provide accurate results with high efficiency.

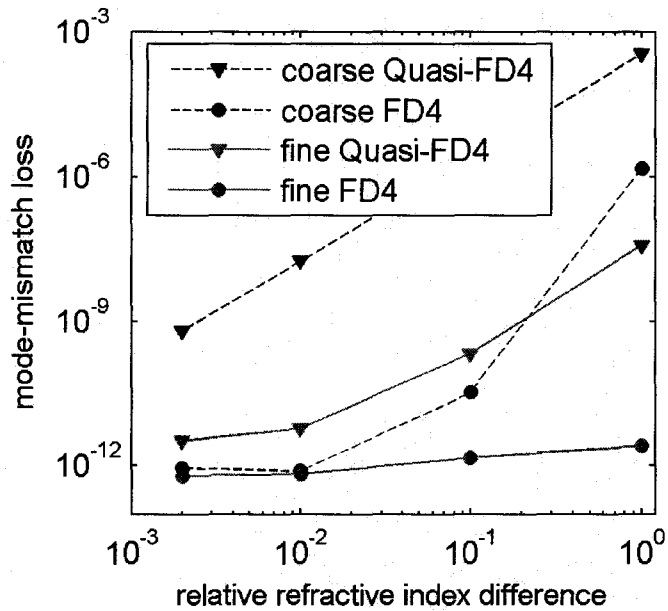

Figure 5.7 The mode-mismatch loss as a function of relative refractive index difference for quasi-FD4 and true FD4. (a) TE mode; (b) TM mode.

5.4 Summary

In this chapter, we have successfully applied the high-order finite-difference formulas to the paraxial scheme and an efficient ultra-wide-angle scheme based on Padé approximations, in which the Padé approximations can go to any higher order. For the 2D structures, the resulting FD equations are tridiagonal in the form of matrix and solvable by the standard solver such as Thomas algorithm. We have compared the accuracy of various FD formulas by simulating the propagation of a cylindrical wave in free space and a TE/TM mode in a step-index slab waveguide. It is demonstrated that the vectorial fourth-order formulation taking into account interface conditions offers highly accurate results, especially when simulating waveguide structures of high index contrast with relatively coarse grids.

Chapter 6
High-Order Reflective Operator Method (ROM)

6.1 Introduction

While wide-angle BPM is able to simulate the wave propagation in z-variant structures, it can never be extended to handle abrupt discontinuities in which the backward propagating fields appear. However, analysis of optical waveguide discontinuities is essential and important in designing integrated photonic devices such as waveguide facets and junctions, antireflection coatings and gratings. An accurate numerical method with high computational efficiency is needed for investigation of reflection and transmission at waveguide discontinuities. Many methods have been developed for analyzing waveguide discontinuities including the modal expansion technique [84]-[86], the finite-difference time-domain (FDTD) method [20][21] and the reflective operator method (ROM) based on the finite-difference (FD) scheme [32],[87]-[89]. The benefits and shortcomings of these methods will be briefly discussed below prior to the description of the main work in this chapter.

The modal expansion techniques expand the reflected and transmitted fields in terms of the guided and radiation modes in the two adjacent waveguides. According to different treatments of the continuous radiation modes, several techniques have been proposed such as the integral equation method [84], the free space radiation mode

(FSRM) method [85], and the complex mode-matching technique in combination with perfectly matched layer (PML) [86]. The integral equation and FSRM methods are highly effective for the analysis for waveguide discontinuity problems with weak and moderate index contrast along transverse direction. These methods, however, fail to yield high accuracy in case of strong guidance, especially for TM waves. The complex mode-matching technique represents the radiation field by a summation of quasi-leaky modes and PML modes, which is highly accurate and efficient when the radiation is relatively oblique to the waveguide axis. In the case of high index contrast and/or small waveguide feature size, the off-axis radiation field becomes more important. Under this circumstance, the complex mode-matching method becomes less accurate and/or efficient. The FDTD method is commonly used to analyze waveguide discontinuities for its flexibility and versatility and can achieve high accuracy. However, it is well known that this method is expensive in terms of computation time and memory consumption. In this respect, the reflective operator scheme provides a good alternative to the above methods as it solves the reduced partial-wave equations simpler than the full-wave Maxwell's equations and yet does not rely on mode expansion. The core idea of the reflective operator scheme is to solve the reflection and transmission formulas involving the square root operator of the characteristic matrix by a noniterative or iterative algorithm.

We may apply different discretization schemes such as the finite-difference (FD) and the finite-element (FE) schemes to the partial-wave reflective equations to reduce the problem into standard matrix equations. The finite difference (FD) scheme is the primary

interest of this chapter. So far, only the standard central-differencing scheme of second-order accuracy has been used in conjunction with the reflective operator scheme for the analysis of waveguide discontinuities. Similar to the other methods, the analysis of waveguide discontinuities using the reflective operator has mainly focused on the case of low index contrast waveguides, except for the recent publication [89] where high index contrast waveguides are treated only in TE polarization.

In this chapter, we apply the vectorial fourth-order FD formula to the reflective operator scheme for the solution of the partial-wave equations in the context of 2D waveguide discontinuities. It is demonstrated that such a scheme can yield remarkable improvement for the numerical accuracy/computation cost ratio for the reflective operator method. It is also found that these benefits become more pronounced with the increase of refractive index contrast. Moreover, the impact of refractive index variation and waveguide geometry on the accuracy of the solutions obtained by the fourth-order and the conventional FD schemes is investigated.

6.2 Iterative Scheme for Reflection and Transmission Formulas

For the sake of simplicity, we confine our discussions to a 2D waveguide discontinuity problem throughout this chapter. The transverse and propagation directions are supposed to be x and z, respectively. Assume that the discontinuity interface exists at

$z=0$ and there is no longitudinal index variation in $z<0$ and $z>0$. As we derived in chapter 2, the Helmholtz equation for both sides of the discontinuity can be written as

$$\frac{d^2\Psi}{dz^2}+L\Psi=0 \tag{6.1}$$

where Ψ represents E_y for TE case or H_y for TM case and the operator L is the defined as

$$L=\begin{cases}\dfrac{\partial^2}{\partial x^2}+k_0^2n^2 & \text{TE}\\ n^2\left[\dfrac{\partial}{\partial x}\left(\dfrac{1}{n^2}\dfrac{\partial}{\partial x}\right)\right]+k_0^2n^2 & \text{TM}\end{cases}. \tag{6.2}$$

The general solution of Eq.(6.1) in each side is

$$\Psi=\Psi^+\exp(-i\sqrt{L}z)+\Psi^-\exp(i\sqrt{L}z) \tag{6.3}$$

where Ψ^+ and Ψ^- are forward and backward propagating fields. If the incident field Ψ^{in} is launched onto the discontinuity interface, the reflected field Ψ^r and transmitted field Ψ^t are generated in the regions of $z<0$ and $z>0$, respectively. By imposing the field continuity condition

$$\Psi\big|_{z=0^-}=\Psi\big|_{z=0^+},\ p_0\frac{\partial\Psi}{\partial z}\bigg|_{z=0^-}=p_1\frac{\partial\Psi}{\partial z}\bigg|_{z=0^+} \tag{6.4}$$

where $p_j=1$, and $p_j=1/n_j^2$, $j=0,1$, for the TE and TM cases, respectively, we obtain the reflection and transmission formulas in terms of the incident field as

$$\Psi^r=\frac{p_0\sqrt{L_0}-p_1\sqrt{L_1}}{p_0\sqrt{L_0}+p_1\sqrt{L_1}}\Psi^{in} \tag{6.5}$$

$$\Psi^t = \frac{2p_0\sqrt{L_0}}{p_0\sqrt{L_0} + p_1\sqrt{L_1}}\Psi^{in} \tag{6.6}$$

In the following, we focus on the solution method for the reflected field. The transmitted field can be obtained similarly. To solve Eq.(6.5), the first step is the rationalization of the square root operators. This can be done by the eigenvalue decomposition method in which all the eigenvalues and eigenvectors of the characteristic matrix have to be found. However, such a process consumes much computation time and memory and therefore is unideal in terms of efficiency. Alternatively, the square root operators can be rationalized by the Padé approximants. Prior to that, the square root operator has to be rewritten as $\sqrt{L_j} = k_0 n_{0j}\sqrt{1+X_j}$ by introducing a reference index n_{0j} associated with the index profile. Consequently, the square root operator $\sqrt{1+X_j}$ can be expanded by the Padé approximation as

$$\sqrt{1+X_j} \approx \prod_{k=1}^{m} \frac{1+c_{k,m}X_j}{1+b_{k,m}X_j} \tag{6.7}$$

where

$$X_j = \frac{1}{k_0^2 n_{0j}^2}\left\{\frac{\partial^2}{\partial x^2} + k_0^2\left[n_j^2 - n_{0j}^2\right]\right\} \tag{6.8}$$

$$c_{k,m} = \sin^2\left(\frac{k\pi}{2m+1}\right),\ b_{k,m} = \cos^2\left(\frac{k\pi}{2m+1}\right) \tag{6.9}$$

It is noticed that the real Padé approximants fail to accommodate the evanescent modes excited at the discontinuity interface [90]. As a result, some errors are introduced to the

calculation of reflected and transmitted fields. To correctly model the evanescent modes, we adopt the rotated branch-cut Padé approximation [88] as follows

$$\sqrt{1+X_j} = e^{i\alpha/2}\sqrt{1+\left[\left(1+X_j\right)e^{-i\alpha}-1\right]} \approx e^{i\alpha/2}\prod_{k=1}^{m}\frac{1+c_{k,m}Y_j}{1+b_{k,m}Y_j} \square W\left(X_j\right) \qquad (6.10)$$

where α is the rotation angle and $Y_j = e^{-i\alpha}\left(1+X_j\right)-1$. With this approximation, Eq.(6.5) can be rationalized as

$$\left[p_0 n_{00} W(X_0) + p_1 n_{01} W(X_1)\right]\Psi^r = \left[p_0 n_{00} W(X_0) - p_1 n_{01} W(X_1)\right]\Psi^{in} \qquad (6.11)$$

where n_{00} and n_{01} are the reference indices of n_0 and n_1, respectively. Under the Padé approximation, the explicit matrix form of the operator $W(X_j)$ is never obtainable. Accordingly, we have to solve Eq.(6.11) by an iterative algorithm in which only the matrix-vector multiplication is required. The bi-conjugate gradient stabilized (Bi-CGSTAB) method [91] is chosen in this chapter to solve the linear system Eq.(6.11) due to its fast convergence rate. However, in the circumstance of large longitudinal discontinuity where higher order Padé approximation is needed to accurately account for the evanescent modes, the convergence rate of the Bi-CGSTAB scheme depends on the condition number of the coefficient matrix. To accelerate the convergence, several preconditioners have been proposed and their comprehensive study can be found in [89][41]. In this chapter, we choose $\left(p_0\sqrt{L_0}\right)^{-1}$ as the proconditioner and then obtain the preconditioned linear system

$$\left[1+W^{-1}(X_0)\left(\frac{p_1 n_{01}}{p_0 n_{00}}\right)W(X_1)\right]\Psi^r = \left[1-W^{-1}(X_0)\left(\frac{p_1 n_{01}}{p_0 n_{00}}\right)W(X_1)\right]\Psi^{in} \qquad (6.12)$$

The last numerical technique for solving the above linear system is the discretization of the differential operator X_j. Substituting the vectorial fourth-order FD formula Eq.(3.33) into the reflection equation (6.12), we finally obtain the finite-difference expression for the reflective operator scheme.

$$c_{i-1}^{r}\Psi_{i-1}^{r} + c_{i}^{r}\Psi_{i}^{r} + c_{i+1}^{r}\Psi_{i+1}^{r} = c_{i-1}^{in}\Psi_{i-1}^{in} + c_{i}^{in}\Psi_{i}^{in} + c_{i+1}^{in}\Psi_{i+1}^{in} \tag{6.13}$$

where the coefficients can be found in Appendix C.

6.3 Numerical Results and Discussion

In this section, the higher-order reflective operator scheme described in Section II will be applied to the analysis of waveguide discontinuity problems. As a measure of the numerical accuracy, we evaluate the power reflectivity of the fundamental mode launched on the discontinuity plane. The power reflectivity can be calculated as the overlap integral between the reflected field and the incident field

$$|R|^2 = \left| \frac{\int_{-\infty}^{\infty} \Psi^r \Psi^{in*} dx}{\int_{-\infty}^{\infty} |\Psi^{in}|^2 dx} \right|^2 \tag{6.14}$$

for TE mode, and

$$|R|^2 = \left| \frac{\int_{-\infty}^{\infty} n^{-2} \Psi^r \Psi^{in*} dx}{\int_{-\infty}^{\infty} n^{-2} |\Psi^{in}|^2 dx} \right|^2 \tag{6.15}$$

for TM mode, where Ψ^{in*} denotes the complex conjugate of the incident field and R is designated reflection coefficient. For comparison, we also calculate the power reflectivity in all examples using FDTD method with a fine mesh and consider it as the benchmark result.

Since our interest is in the accuracy of reflectivity associated with the FD scheme, the numerical errors caused by other factors such as Padé approximations have to be minimized. For this reason, we first examine the effect of Padé order on the accuracy of reflectivity. We analyze a widely used waveguide facet terminated by air, as shown in Figure 6.1(a).

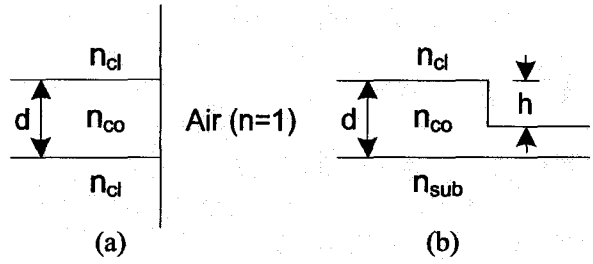

Figure 6.1 Schematic diagrams of waveguide facet (a) and partially etched waveguide (b).

The waveguide parameters are: the core index $n_{co} = 3.6$, the cladding index $n_{cl} = 3.24$, the core width $d = 0.12$ μm and the wavelength $\lambda = 0.86$ μm. We employ a 6.0 μm computation window discretized by 600 uniform meshes and terminated by a PML [26] of 0.6 μm width for the simulation. The rotation angle is set to be $\pi/2$. We calculate the reflectivities of the fundamental TE and TM modes using both the conventional central difference scheme (CD) and the vectorial fourth-order FD formula

(FD4). The variation of the reflectivity with the Padé order is shown in Figure 6.2. It is observed that the reflectivities for both the TE and TM modes become stabilized at Padé (4, 4), either for CD or for FD4 scheme, and they converge to the values of 0.3747 and 0.2559, respectively, which are obtained by the FDTD method. This indicates that the Padé order (4, 4) is sufficient to obtain an accurate reflectivity provided that the rotation angle is $\pi/2$.

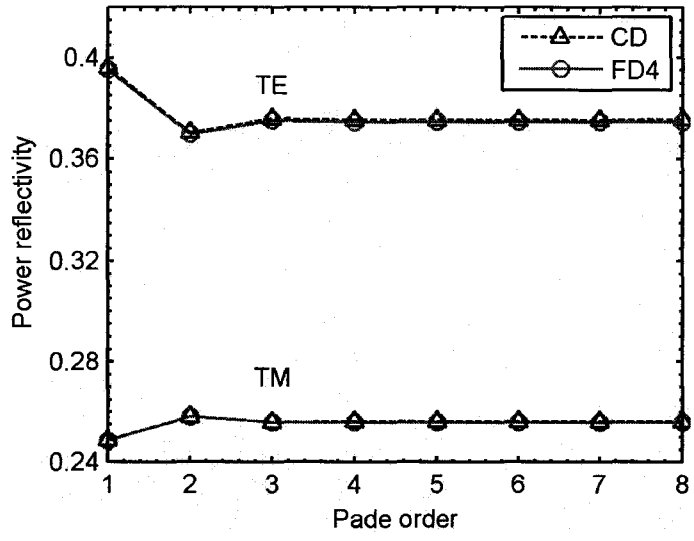

Figure 6.2 Variation of the power reflectivity with the Padé order using the CD and FD4 formulas for a waveguide facet.

We now study the convergence of the CD and FD4 schemes in calculating the power reflectivity at waveguide facets. For the sake of comparison, we consider two examples: low and high index contrast waveguides. The core index is 3.6 and the cladding index is $3.6(1-\Delta)$ with Δ taken to 10% and 58.3%, respectively. The Padé order (4, 4) is chosen to highlight the discretization errors. The other parameters are the

same as in Figure 6.2. It is shown that the Padé order (8, 8) is sufficient to achieve high degree accuracy and therefore is used for all the simulations in this chapter.

Figure 6.3 shows the power reflectivity as a function of mesh size for fundamental TE and TM modes, respectively. Generally speaking, the discretization error decreases as the mesh size reduces and goes to zero as the mesh size shrinks to zero. Therefore, the reflectivities calculated by both the CD and FD4 schemes become more accurate with the decrease of mesh size and converge to the benchmark values given by the FDTD method. With the same mesh size, however, the discretization error in the higher-order FD scheme is proportional to $(\Delta x)^4$ whereas the conventional scheme is $(\Delta x)^2$. For this reason, the FD4 scheme converges to the benchmark faster, compared to the CD scheme. It is worthwhile to mention that the FD4 formula yields far more accurate results than the CD scheme in the case of coarse mesh ($\Delta x = 0.06$ μm corresponding to two grid points in core), especially for the high index contrast waveguide in which the CD scheme fails.

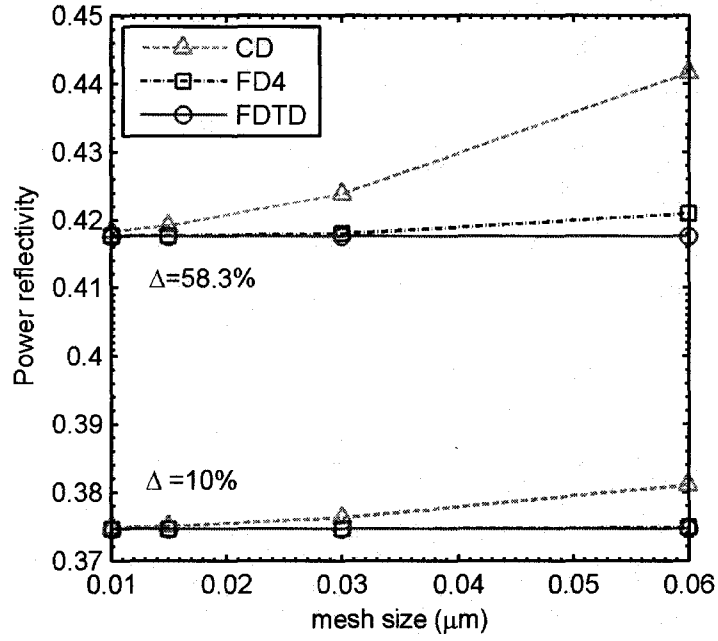

(a)

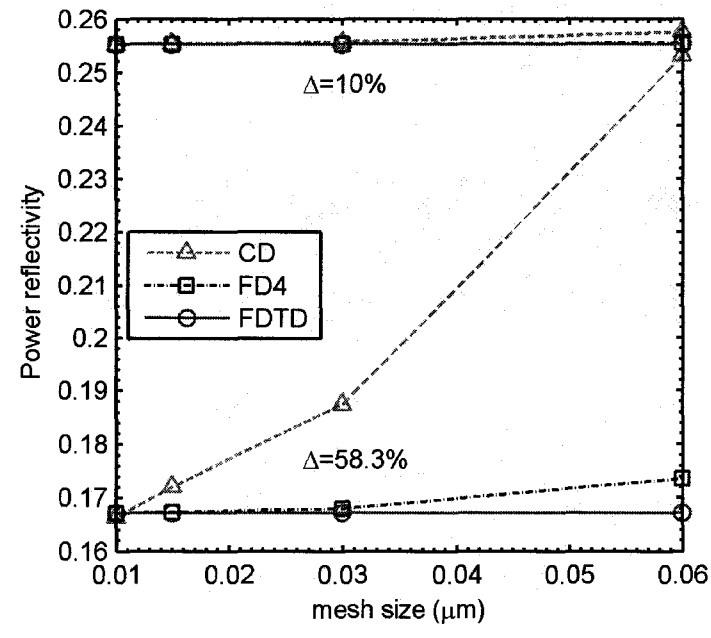

(b)

Figure 6.3 Power reflectivity as a function of mesh size Δx with CD and FD4 formulas for a waveguide facet. (a) TE mode; (b) TM mode.

In Table 6.1 and 6.2, we list the grid points that are needed by both the CD and FD4 schemes to achieve the same relative error of the reflectivity for the case of $\Delta = 58.3\%$. It is noted that, for a small allowed relative error (0.17% for TE and 0.52% for TM), the FD4 scheme requires only 200 grid points whereas 600 points are needed to achieve the same accuracy by using the CD scheme. This implies that we save roughly 67% in memory.

Relative error	Grid points with CD	Grid points with FD4
$< 0.17\%$	600	200
$< 0.80\%$	400	100

Table 6.1 Grid points for TE.

Relative error	Grid points with CD	Grid points with FD4
$< 0.52\%$	600	200
$< 3.86\%$	400	100

Table 6.2 Grid points for TM.

We also observed by examining Figure 6.3 that the advantage of FD4 formula is more pronounced for the high index contrast waveguides than for the low index contrast ones. To illustrate this point more clearly, we consider various symmetric slab waveguides with different index contrasts. The core index is fixed at 3.6 and the cladding index is $3.6(1-\Delta)$ with Δ successively varying from 5% to 58.3%. A coarse mesh ($\Delta x = 0.06\,\mu m$) is chosen such that there exist only two grid points in core. The other parameters are the same as in Figure 6.2. The power reflectivity of the fundamental TE

and TM modes as a function of index contrast is plotted in Figure 6.4. It can be seen that the FD4 scheme is capable of providing acceptable reflectivity over the whole range of index contrast. However, the accuracy of reflectivity calculated by the CD scheme deteriorates as the index contrast increases. The explanation of this behaviour is that, when the index contrast increases, the transverse fields become more confined to the core region. Therefore, the magnitude of the transverse derivatives of the fields and the discontinuity of the transverse derivatives of the magnetic fields for TM case increase. The coarse CD scheme fails to capture these fine features due to its poor treatment of the interface condition. The FD4 formula succeeds in mitigating this problem by its proper treatment of the interface and more accurate discretization.

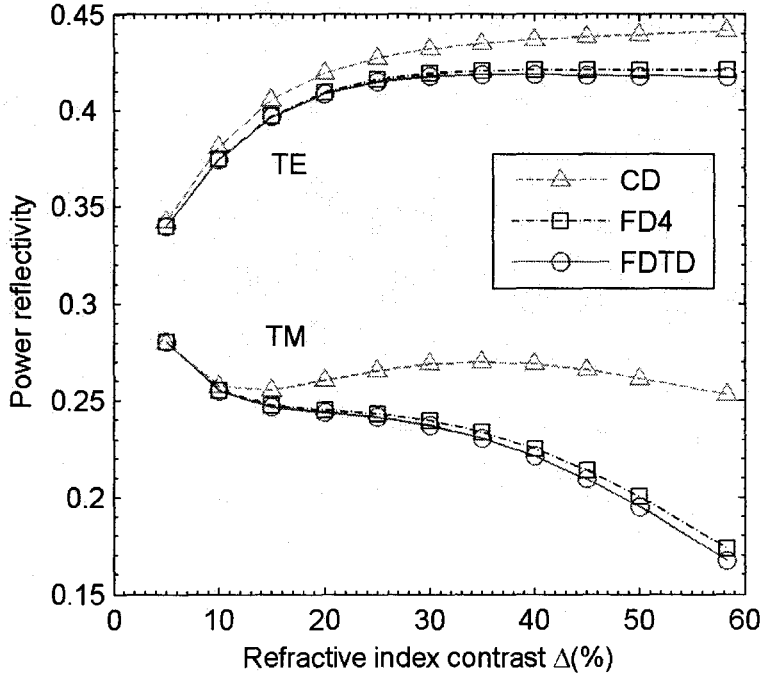

Figure 6.4 Power reflectivity as a function of refractive index contrast Δ with CD and FD4 formulas for a waveguide facet.

Further, we examine the performance of the higher-order reflective schemes by calculating the power reflectivity for different waveguide core widths. The mesh size is chosen to be $\Delta x = 0.06\,\mu m$. Figure 6.5 presents the power reflectivity of the fundamental TE and TM modes against the core width for both low and high index contrast waveguides. For the purpose of comparison, the results obtained by the CD scheme are shown in the same figure. It is observed that the superiority of the FD4 scheme is pronounced for small core widths and becomes less obvious as the core width increases. This can be explained by the relative smooth field variation occurring on the index interface of large-core waveguides where the accuracy of reflectivity is not very sensitive to the treatment of interface conditions. It is concluded that the higher-order FD4 is more suitable than the conventional CD for high index contrast waveguides with a small core layer.

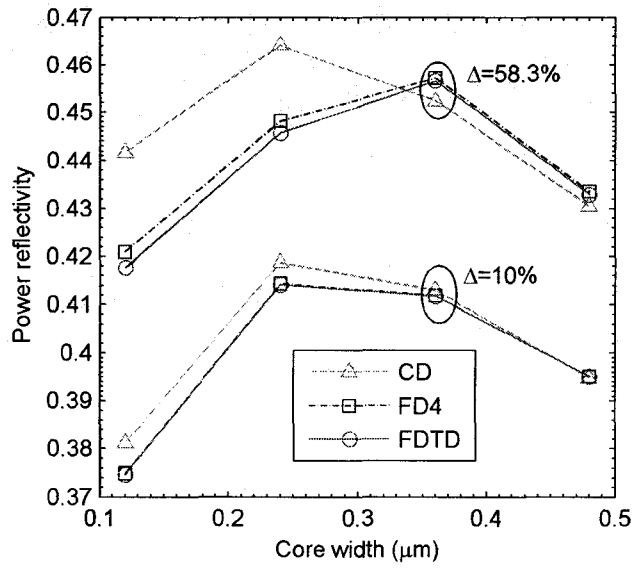

(a)

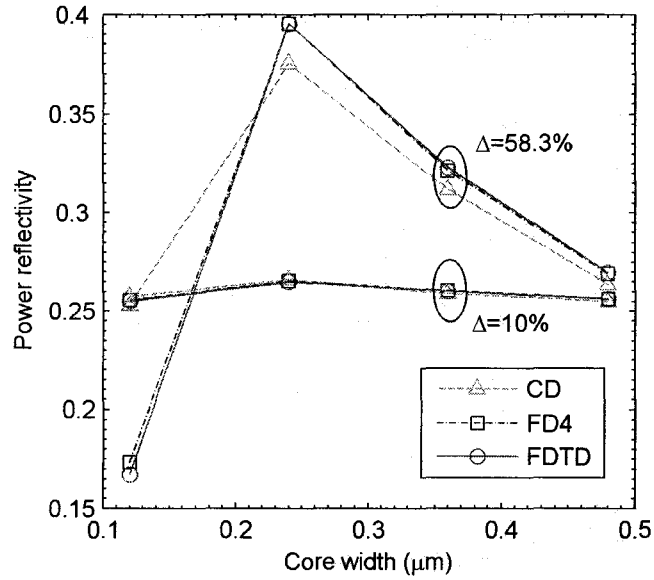

(b)

Figure 6.5 Power reflectivity versus core width d with CD and FD4 formulas for a waveguide facet. (a) TE mode; (b) TM mode.

Finally, we evaluate the accuracy of the higher-order reflective scheme through the analysis of a partially etched waveguide with high index contrast, as depicted in Figure 6.1(b). The structure parameters are: the core index $n_{co} = 3.6$, the cladding index $n_{cl} = 1.0$, the substrate index $n_{sub} = 1.5$, the core width $d = 0.2$ μm and the wavelength $\lambda = 1.55$ μm. In our calculation, a computation window of 8.0 μm enclosed by a PML region of 0.5 μm thickness on each side is used. The power reflectivity of the fundamental modes versus the etching depth is illustrated in Figure 6.6, where both the CD and FD4 schemes are employed with coarse mesh ($\Delta x = 0.1$ μm) and fine mesh ($\Delta x = 0.02$ μm), respectively. It is shown that the FD4 scheme is able to achieve a

comparable accuracy of the conventional CD scheme with 80% reduction in computational cost.

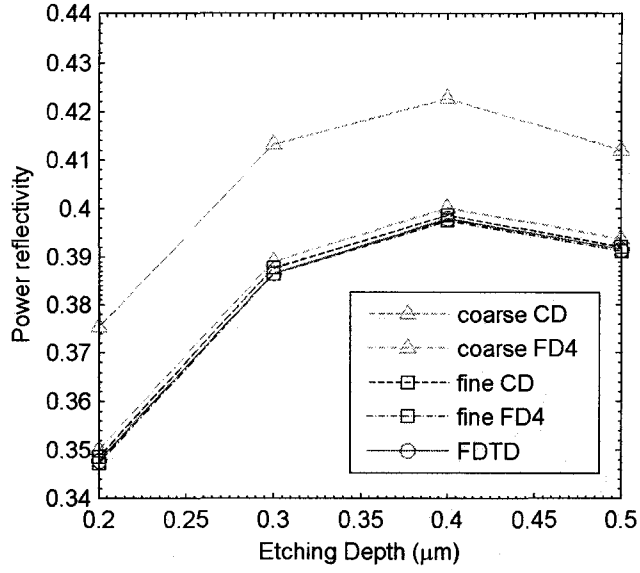

(a)

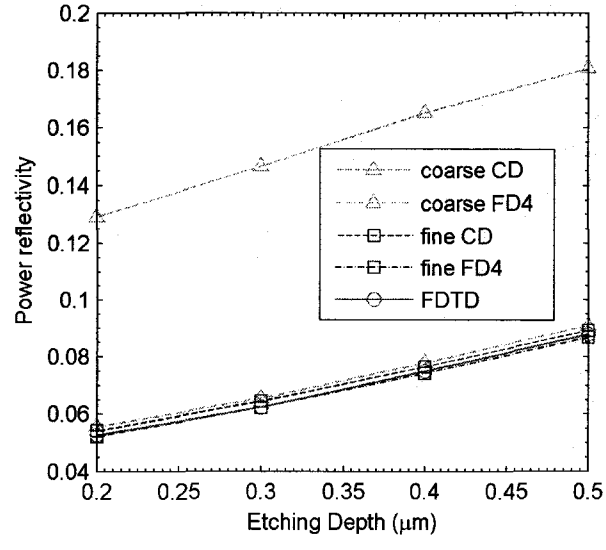

(b)

Figure 6.6 Power reflectivity versus etching depth h using CD and FD4 formulas with coarse and fine meshes, respectively, for a partially etched waveguide. (a) TE mode; (b) TM mode.

6.4 Summary

In this chapter, we have applied the vectorial fourth-order finite-difference formula to a reflective operator method in order to accurately and efficiently analyze waveguide discontinuities. Some of the salient features and distinct advantages of the new schemes are assessed by calculating the modal reflectivity of waveguide facets and partially etched waveguides against the full-wave FDTD solutions. It is revealed that the advantage of the higher-order reflective scheme lies in the significant improvement on the ratio of numerical accuracy vs computational cost. Furthermore, we have demonstrated that the present method is particularly useful for modeling and simulation of high index contrast structures with small feature sizes.

Chapter 7
High-Order Bidirectional Beam Propagation Method (BiBPM)

7.1 Introduction

In the previous chapter, we developed a high-order reflective operator method for handling reflections from waveguide discontinuities. Although demonstrated to be very accurate and efficient, it focuses on problems involving a single interface. Optical guided-wave structures consisting of multiple discontinuities along the propagation direction such as corrugated gratings are widely used in passive, functional and active photonic devices and integrated circuits for coupling, filtering, switching, optical feedback, etc. Modeling and analysis of these reflective structures are essential in design of integrated photonic circuits.

Several non-BPM approaches have been successfully employed to simulate bidirectional wave propagation. The coupled-mode theory (CMT) [11] is an approximate yet insightful method to describe the interaction of the counter-propagating modes in the structure. In general, the coupled-mode theory is accurate and most useful for optical waveguides with relatively weak index contrast in which the significant power exchange between the forward and backward guided modes occurs within a length of many wavelengths. Coupling to radiation modes due to the index discontinuities along the

waveguide axis may also be considered within the framework of the CMT in combination of Green's function approach [92][93] or using the continuous radiation modes [94]. As the index contrast over the waveguide cross-section and/or index discontinuities along the waveguide axis increase, the simple CMT analysis becomes less applicable. In practice, numerical techniques in both time and frequency domains are used to treat the reflective waveguide structures with high index contrast and/or large index discontinuities. Examples of such methods are the finite-difference time-domain (FDTD) method, the mode matching method (MMM) [86], method of lines (MoL) [15], and the bi-directional beam propagation method (BiBPM) [33]-[41]. A comprehensive review of these methods is given in [95][96]. Generally speaking, the purely numerical FDTD method is most rigorous, versatile, and time-consuming, whereas the analytical MMM is most efficient and accurate for certain structures. In this respect, the full-wave BiBPM offers a frequency-domain full-wave approach with a good balance among flexibility, accuracy and efficiency.

In the early development of BiBPMs, the main focus was on robust algorithms that can take into account of the multiple reflections and transmissions at the longitudinal discontinuities. A major challenge for the BiBPM is to correctly model the evanescent waves, which are excited at reflecting interfaces and decay in slowly varying or uniform sections. Incorrect treatment of these evanescent waves may cause degradation of accuracy and give rise to serious instability problems. This problem becomes particularly acute for strongly reflecting structures with high longitudinal refractive index contrast

[36]. Therefore, the correct modeling of evanescent waves is very important and hence received much attention in the research and development related to BiBPMs.

In BiBPM, one of the critical procedures is to perform a decomposition for the square root operator $\sqrt{1+X}$, which describes the partial waves incident, reflected and transmitted from the longitudinal discontinuities. This square root operator can be rigorously evaluated by the eigenvalue decomposition method, in which the evanescent mode spectrum is automatically included. However, the expensive computation arising from solving the eigensystem precludes its widespread use. Alternatively, rational approximations to the square root operator such as Padé approximation are frequently used. The standard Padé approximant is first applied to the wide-angle BPM [30] and is shown to be able to handle one-way propagation provided that the evanescent waves are not largely excited. Nevertheless, it fails to generate the evanescent modes corresponding to $X<-1$. A complex-valued rationalization to $\sqrt{1+X}$ has been proposed to correctly model the evanescent modes which are non-negligible in some structures. Two approaches have been developed to take into account the evanescent mode spectrum. The first one is the rotated branch cut method [97], where the complex-valued approximation can be obtained by rotating the original real axis branch cut by a rotation angle and then applying the standard Padé approximant to the new variable. The second approach is the complex coefficient Padé approximation [90], where the complex coefficients can be calculated by solving nonlinear equations with Newton's method.

For BiBPM, the correct modeling of evanescent waves includes its generation at discontinuities and proper decay in uniform regions. As a result, the complex-valued approximation to $\sqrt{1+X}$ is needed not only for the transition operator, but for the propagation operator. Among the existing BiBPMs, those based on the transfer matrix method have difficulty applying the complex-valued approximation to the propagator due to the stability issue. Although the complex propagators are employed in [34] by choosing a complex reference wave number, the normal propagating waves are affected simultaneously by spurious imaginary parts. The BiBPM based on a scattering operator formulation [37] allows the use of complex propagators without encountering the stability problem. This is due to the nature of scattering operators in which the backward propagation operator is avoided. We note that the example used in [37] is a weakly modulated grating where the evanescent modes only carry a small portion of the total energy. The requirement for the accurate simulation of evanescent mode spectrum is less demanding in that circumstance. In strongly reflecting structures, the correct modeling of the evanescent modes becomes critical, and it becomes necessary to systematically evaluate the effects of various rational approximations to the square root operator on the solution accuracy.

In this chapter, following the truly stable BiBPM [37], we first demonstrate the necessity and significance of using the complex representation of the propagation operator. We then investigate the effects of the rotation angle and the parameter β on the performances of the rotated Padé approximation and the complex coefficient Padé approximation, respectively. Subsequently, a comparative assessment of various rational

approximations is performed in terms of accuracy in different circumstances where the evanescent portions of the total energy differ. Useful guidelines are provided for accurate simulation of multiple reflecting structures in the context of BiBPM.

It is worth mentioning that another BiBPM based on iterative procedure [39] is able to handle evanescent modes and keeps numerical stability as well. But this iterative method requires a pre-conditioner at each reflection interface to improve the convergence and stability of the algorithm, especially for complex structures with large longitudinal discontinuities. The robustness and effectiveness of the pre-conditioners for these complex structures are not known a priori and somewhat problem dependent. The complexity and uncertainty imposed by the pre-conditioners make the iterative method less appealing than the one based on the scattering operators.

Efficiency is another critical issue for the BiBPM. Most of the reflective optical waveguide structures operate based on the principle of constructive or destructive interference between the forward and backward propagating waves. Therefore, it is extremely important that any numerical simulation methods must calculate not only the amplitudes but also the phases of the counter-propagating waves with sufficient accuracy. In the finite-difference solutions, the phase errors depend critically on the transverse discretization schemes. So far, all the BiBPMs reported employ the scalar second-order accurate finite-difference (FD) formula for the transverse discretizations. In order to reduce the phase error, a relatively fine mesh is needed which leads to an increase in computation time and memory storage. The mesh requirement becomes even more demanding when dealing with high index contrast structures with fine geometric features.

The resulting increase in the computational cost and memory requirement is significant for the scattering operator formulation, because the explicit evaluations of matrices representing the square root operators are involved therein. Consequently, mesh refinement is not an economical way to maintain phase accuracy. This chapter is also devoted to improving the accuracy and efficiency of the BiBPM based on the scattering operators by improving the discretization scheme.

In this chapter, we apply the vectorial fourth-order finite-difference scheme to the BiBPM based on the scattering operators. Comparing with the previous BiBPM employing the scalar second-order accurate FD formula, the present method offers significantly higher accuracy without significant increase in computation cost and memory requirements. In other words, the new method permits the use of much fewer sampling points to achieve comparable levels of accuracy, resulting in considerable saving in computational time and memory consumption. This advantage is particularly useful for structure of large transverse index contrast and/or longitudinal index discontinuities as demonstrated later in this chapter.

7.2 Scattering Operator Formulation

We consider the propagation of optical waves in a planar waveguide. The transverse and propagation directions are supposed to be x and z, respectively. Any piecewise uniform waveguide can be characterized by a series of z-invariant index profiles, i.e., $n(x,z) = n_j(x)$ for $z_{j-1} < z < z_j$, where $j = 1,2,\cdots,m$. We assume that the

waveguide is z-invariant for $z<0$ and $z>a$, where a is the length of region of interest. The fields at any z position are composed of forward ("+") and backward ("–") propagating fields: $\Psi=\Psi^{+}+\Psi^{-}$, where Ψ represents E_y for TE case or H_y for TM case. Considering the z-uniform section $z_{j-1}<z<z_j$, the well-known one-way Helmholtz equations are $\partial\Psi^{+}/\partial z=-iL_j\Psi^{+}$ and $\partial\Psi^{-}/\partial z=iL_j\Psi^{-}$, where $L_j=k_0n_0\sqrt{1+X_j}$. The operator X_j is defined as

$$X_j=\begin{cases}\left(k_0n_0\right)^{-2}\left[\dfrac{\partial^2}{\partial x^2}+k_0^2n_j^2(x)-k_0^2n_0^2\right] & \text{TE}\\ \left(k_0n_0\right)^{-2}\left[n_j^2\left[\dfrac{\partial}{\partial x}\left(\dfrac{1}{n_j^2}\dfrac{\partial}{\partial x}\right)\right]+k_0^2n_j^2(x)-k_0^2n_0^2\right] & \text{TM}\end{cases} \tag{7.1}$$

where n_0 refers to the reference refractive index.

The scattering operator formulation relies on the reflection operator $R(z)$ and transmission operator $T(z)$, defined as

$$R(z)\Psi^{+}(\cdot,z)=\Psi^{-}(\cdot,z) \tag{7.2}$$

$$T(z)\Psi^{+}(\cdot,z)=\Psi^{+}(\cdot,a+). \tag{7.3}$$

The reflection operator relates the forward field to the backward field corresponding to the same z position. The transmission operator relates the forward field at z to the forward field at $a+$. With these definitions, the reflected and transmitted fields can be found from the operators $R(0^{-})$ and $T(0^{-})$. Under the assumption that there is only outgoing wave for $z>a$, the two definitions give rise to the initial conditions: $R(a+)=0$ and $T(a+)=I$,

where I is the identity operator. The operators $R(0^-)$ and $T(0^-)$ can be calculated by a sweeping process from the output to the input of the structure involving transition step and propagation step. By using the continuity of Ψ and $\partial\Psi/\partial z$ at $z = z_j$, we obtain the transition step

$$C = \begin{cases} L_j^{-1} L_{j+1} \left[I - R(z_j+) \right] \left[I + R(z_j+) \right]^{-1} & \text{TE} \\ L_j^{-1} \dfrac{n_j^2}{n_{j+1}^2} L_{j+1} \left[I - R(z_j+) \right] \left[I + R(z_j+) \right]^{-1} & \text{TM} \end{cases} \tag{7.4}$$

$$R(z_j-) = (I + C)^{-1} (I - C) \tag{7.5}$$

$$T(z_j-) = T(z_j+) \left[I + R(z_j+) \right]^{-1} \left[I + R(z_j-) \right]. \tag{7.6}$$

For the propagation step in z-invariant section, we have

$$R(z_{j-1}+) = P_j R(z_j-) P_j \tag{7.7}$$

$$T(z_{j-1}+) = T(z_j-) P_j \tag{7.8}$$

where $P_j = \exp\left(-i(z_j - z_{j-1}) L_j\right)$ is the propagation operator. For periodic waveguides, the sweeping process over the entire structure is not needed. The operators $R(0^-)$ and $T(0^-)$ can be obtained from the scattering operators of a single period with the help of a period doubling process [38]. Thus, the computational time is significantly reduced.

As seen from Eqs.(7.4)-(7.8), both transition and propagation operators involve the square root of the transverse operator, i.e., $L_j = k_0 n_0 \sqrt{1 + X_j}$. In the mode-matching

method (MMM), this operator is approximated by a linear combination of the local guided and un-guided modes [86]. For BPM-related methods, a number of rational approximations of $\sqrt{1+X}$ have been proposed, such as Taylor-type [98] and Padé-type approximations. In particular, the latter is widely used due to its efficient numerical implementations. The Padé-type approximations include real-valued Padé, rotated branch cut Padé, and complex coefficient Padé approximations. The rationalized L_j using different type approximations can be written in a compact form

$$L_j = k_0 n_0 e^{i\alpha/2}\left(1+\sum_{k=1}^{p}\frac{a_k^{(p)}\tilde{X}_j}{1+b_k^{(p)}\tilde{X}_j}\right) = k_0 n_0 e^{i\alpha/2}\prod_{k=1}^{p}\frac{1+c_k^{(p)}\tilde{X}_j}{1+b_k^{(p)}\tilde{X}_j} \tag{7.9}$$

where $\tilde{X}_j = e^{-i\alpha}\left(1+X_j\right)-1$, α is the rotation angle, and the Padé coefficients $a_k^{(p)}$, $b_k^{(p)}$ and $c_k^{(p)}$ could be real or complex. The real-valued coefficients are given as

$$c_k^{(p)} = \sin^2\left(\frac{k\pi}{2p+1}\right),\ b_k^{(p)} = \cos^2\left(\frac{k\pi}{2p+1}\right),\ a_k^{(p)} = \frac{2c_k^{(p)}}{2p+1}. \tag{7.10}$$

The complex-valued coefficients $b_k^{(p)}$ and $c_k^{(p)}$ are solutions of the following nonlinear equations [90]

$$\begin{aligned}
&\sum_{k=1}^{p}\frac{\sin^2(2k\theta)}{t-\cos^2(k\theta)}+(2p+1)\left(1-\frac{2i}{\beta}\right)=0 \quad \text{for } b_k^{(p)}\\
&\sum_{k=1}^{p}\frac{\sin^2(2k\theta)}{t-\sin^2(k\theta)}+(2p+1)\left(1-\frac{2i}{\beta}\right)=0 \quad \text{for } c_k^{(p)}
\end{aligned} \tag{7.11}$$

where $\theta=\pi/(2p+1)$, i refers to the imaginary unit, and β is a negative constant. The complex coefficients $a_k^{(p)}$ can be calculated from $b_k^{(p)}$ and $c_k^{(p)}$ as follows:

$$a_k^{(p)} = \left(c_k^{(p)} - b_k^{(p)}\right)\prod_{j\neq k}\frac{c_j^{(p)} - b_j^{(p)}}{b_j^{(p)} - b_j^{(p)}}. \tag{7.12}$$

To make the propagation operator practically implementable, a [q/q] Padé approximation in the propagation direction is applied to the exponential function [83], i.e., $e^y = \prod_{l=1}^{q}\left(1-\bar{e}_l y\right)/\left(1+e_l y\right)$. The resulted P_j is expressed as

$$P_j = \exp(-ik_0 n_0 \Delta z e^{i\alpha/2})\prod_{k=1}^{p}\prod_{l=1}^{q}\frac{1+\gamma_{kl}\tilde{X}_j}{1+\beta_{kl}\tilde{X}_j} \tag{7.13}$$

where $\beta_{kl} = b_k^{(p)} - ik_0 n_0 \Delta z e^{i\alpha/2} a_k^{(p)} e_l$ and $\gamma_{kl} = b_k^{(p)} + ik_0 n_0 \Delta z e^{i\alpha/2} a_k^{(p)} \bar{e}_l$.

Finally, the explicit matrix forms of the transition and propagation operators can be obtained by approximating the spatial second derivative with a FD formula. Aiming at reducing the phase error in an efficient manner, we use the vectorial fourth-order FD formula (FD4), i.e., $\partial^2/\partial x^2 = D_x^2/\left(1+g_1 D_x + g_2 D_x^2\right)$. When this is applied to Eqs.(7.9) and (7.13), we obtain

$$L_j = k_0 n_0 e^{i\alpha/2}\prod_{k=1}^{p}\frac{Y + c_k^{(p)} Z_j}{Y + b_k^{(p)} Z_j} \tag{7.14}$$

$$P_j = \exp(-ik_0 n_0 \Delta z e^{i\alpha/2})\prod_{k=1}^{p}\prod_{l=1}^{q}\frac{Y + \gamma_{kl} Z_j}{Y + \beta_{kl} Z_j} \tag{7.15}$$

where $Y = 1 + g_1 D_x + g_2 D_x^2$, $Z_j = \left[e^{-i\alpha}/\left(k_0 n_0\right)^2\right]\left\{D_x^2 + \left[k_0^2 n_j^2(x) - k_0^2 n_0^2\right]Y\right\} + (e^{-i\alpha} - 1)Y$.

The definitions of g_1, g_2, D_x, and D_x^2 are detailed in Appendix A. Note that both D_x and D_x^2 are three-point FD operators. Thus, compared with the scalar second-order FD

formula (FD2) commonly used in previous BiBPMs, the FD4 does not increase the matrix bandwidth.

7.3 Assessment of Various Rational Approximations

In order to assess the performances of various rational approximations to $\sqrt{1+X}$ in modeling the evanescent waves, we consider a structure with large transverse index contrast and longitudinal discontinuities such that the evanescent mode spectrum is large and must be accurately simulated. The structure is schematically shown in Figure 7.1. The core index of the input and output sections is $n_{0g} = 3.4$. The core index of the gap region n_{1g} can be adjusted to construct reflecting interfaces with different intensity. All sections share the same cladding index $n_c = 1.45$. The core thickness is $h = 0.25$ μm. The width of the gap region is $w = 0.1$ μm. The wavelength is $\lambda = 1.55$ μm. We set $n_{1g} = n_c$ in the first stage of simulations, forming two strongly reflecting interfaces and a uniform gap section without guidance. Thus, we have constructed a good example to evaluate the "evanescent behaviours" of various Padé-type approximations.

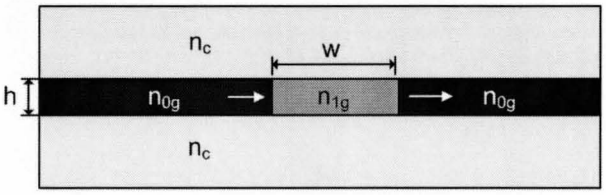

Figure 7.1 Schematic structure for assessment.

We first calculate the reflected field at the left interface and the transmitted field at the right interface by a rigorous mode matching method (MMM) based on the scattering matrix [86]. We use 100 modes for modal expansion to include the evanescent mode spectrum and therefore provide a reliable reference solution. The reflected and transmitted fields calculated by the BiBPM using different rational approximations are then compared with reference solutions. The evaluation criterion is established by calculating the relative error in L2 norm between the BiBPM solutions and reference solutions.

For all the simulations in this section, we discretize the transverse differential operator with a vectorial fourth-order accurate finite difference formula in a computational window of 12 μm containing two perfectly matched layers (PML) of 1 μm. The mesh size is set as $\Delta x = 0.025$ μm and $\Delta z = 0.01$ μm. The reference index is chosen to be the effective index of the corresponding section. The incident field is the fundamental mode of the input waveguide. The exponential function in the propagation operator P_j is approximated with Padé (2, 2) approximant. The high order discretization with a relatively fine mesh and the large computational window are employed in view of reducing the solution errors caused by discretization and boundary condition. Doing so allows us to assess various rational approximations on a more objective level. Several aspects important for the approximations of square root operators are systematically investigated in the context of BiBPM.

A. Effect of Complex Propagation Operators

To investigate how rational approximations of the propagation operator influence the solution accuracy in strongly reflecting structures, we have to properly model the generation of evanescent modes at longitudinal interfaces. Our latter simulations show that the Padé (8, 8) approximant with a rotation angle of $\pi/2$ can achieve a good approximation to transition operators. Therefore, this setting is fixed for all simulations in this part. We calculate the relative L2-norm errors of reflected and transmitted fields for both TE and TM polarizations. The results obtained using different approximations to the propagation operator are shown in Figure 7.2.

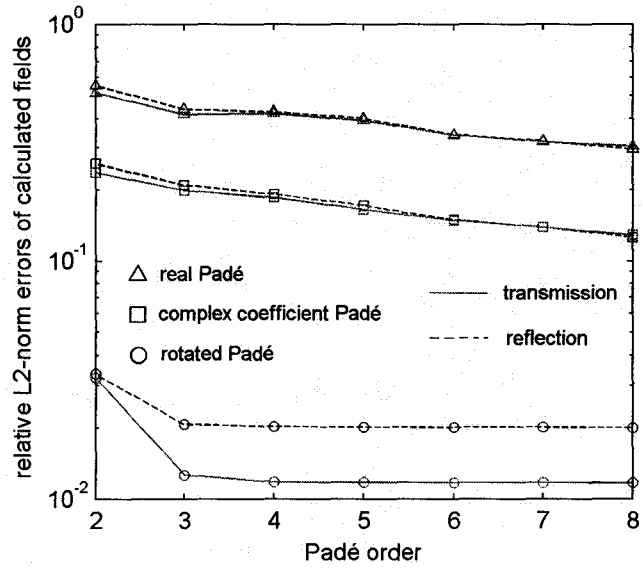

(a)

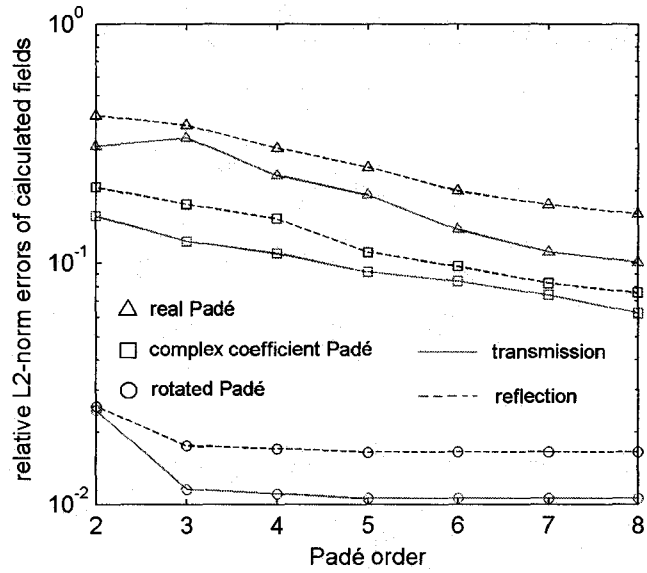

(b)

Figure 7.2 Relative L2-norm errors of the calculated fields obtained from different Padé approximations to the propagation operator. The transition operator is approximated by rotated branch cut Padé (8, 8) with $\alpha = \pi/2$ in all simulations. (a) TE; (b) TM.

It is clearly shown that the real Padé exhibits the worst performance. This is because the real Padé approximant is absent of imaginary parts for $X < -1$. As a result, it treats the evanescent modes which are supposed to decay exponentially as the propagating modes. In contrast, the complex-valued Padé approximants avoid this problem and therefore achieve higher accuracy. We notice that the rotated branch cut Padé exhibits better performance than the complex coefficient Padé in approximating the propagator. This behaviour can be understood as the less accurate decay rate of the complex coefficient Padé approximant. It is worth mentioning that complex propagator are also employed in [36] by choosing a complex reference wave number. However, this technique is not applicable to the normal propagating region. Otherwise, the instability may arise due to

its improper treatment of the propagating modes. In the present BiBPM algorithm, we do not encounter instability problems, as will be seen in section *E*, where the normal propagating region appears.

B. Effect of Parameter β

For the complex coefficient Padé approximation, it is pointed that the parameter β can be used to adjust the damping for the evanescent modes and the accuracy for approximating the propagating modes [90]. So far, no literature has investigated how this parameter affects the solution accuracy. This effect is investigated by numerical results in this part. The complex coefficients $a_k^{(p)}$, $b_k^{(p)}$, and $c_k^{(p)}$ are first calculated with different β and with fixed Padé order of (8, 8), then we calculate the relative L2-norm errors of the fields using those Padé approximants with different β values. In Figure 7.3, it is revealed that the complex coefficient Padé approximant with $\beta = -1$ can represent the square root operator most accurately, for both TE and TM polarizations.

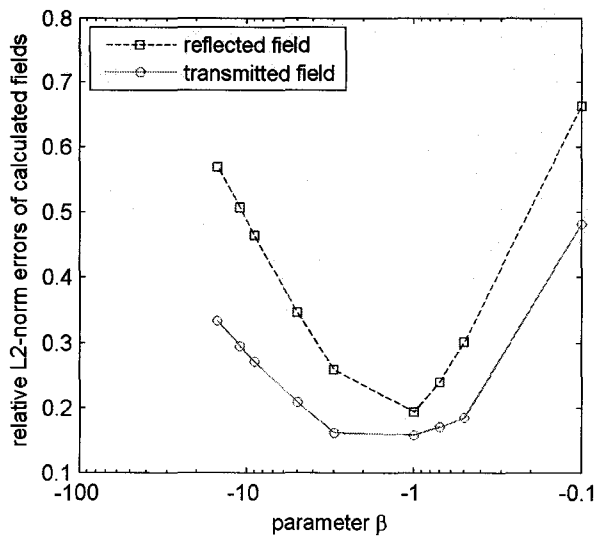

(a)

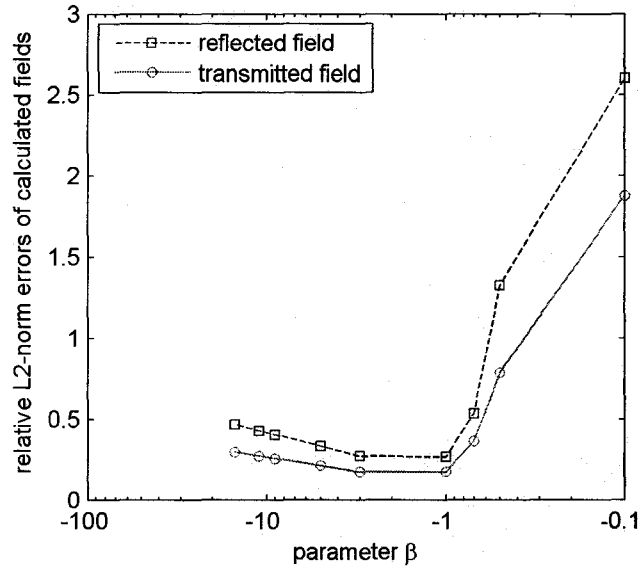

(b)

Figure 7.3 Relative L2-norm errors of the calculated fields obtained from complex coefficient Padé (8, 8) approximations with different β. (a) TE; (b) TM.

C. Effect of Rotation Angle α

The rotation angle α is a critical parameter for the rotated branch cut Padé approximations. Here we investigate the effect of the rotation angle on the solution accuracy. We set the Padé order as (8, 8) to suppress the associated error. The relative L2-norm errors of the fields are plotted in Figure 7.4 as a function of rotation angle. It is found that the field errors become stabilized at $\pi/4$. This conclusion is consistent with the finding in [88], where the rotated branch cut Padé approximation is applied to single reflecting interface only. Thus, we have demonstrated that a good approximation can be achieved for both the transition operator and propagation operator provided that the rotation angle is greater than $\pi/4$.

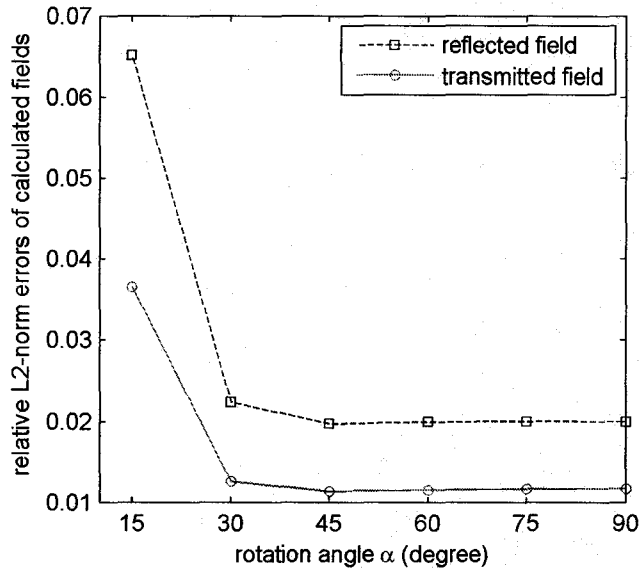

(a)

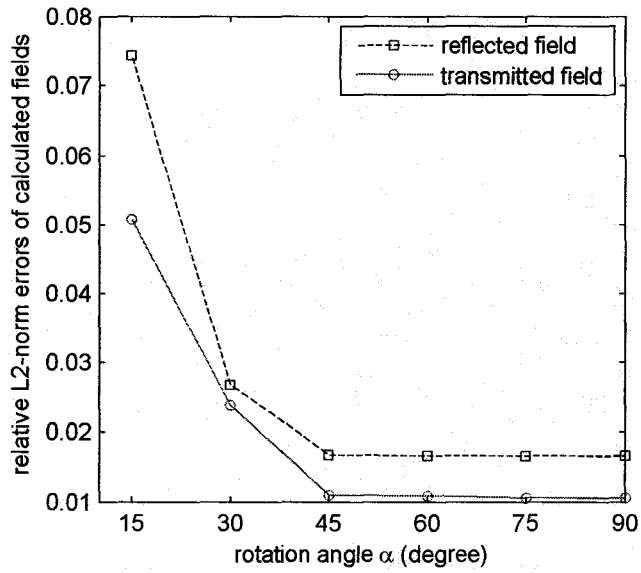

(b)

Figure 7.4 Relative L2-norm errors of the calculated fields obtained from rotated branch cut Padé (8, 8) approximations with different rotation angles α. (a) TE; (b) TM.

D. Comparison of Various Padé-Type Approximations

In this part, we compare four types of rational approximations, namely, real Padé, complex coefficient Padé, rotated branch cut Padé, and complex coefficient Padé with rotated branch cut, in order to examine their effectiveness in BiBPM for simulation of reflective optical waveguide structures. We set $\beta = -1$ and $\alpha = \pi/2$ for complex coefficient Padé and rotated branch cut Padé, respectively, such that each of them can achieve best performance for a certain Padé order. The field errors as a function of Padé order obtained from different approximations are shown in Figure 7.5. It is clearly demonstrated that all the complex-valued Padé approximations generate smaller errors than the real-valued Padé approximation. The ineffectiveness of the real-valued Padé approximation mainly arises from its failure to correctly model the excitation of evanescent modes. Again, it is observed that the complex coefficient Padé is less accurate than the rotated branch cut Padé. As we discussed in section *A*, its performance degradation could come from its less accurate simulation of the evanescent wave propagation. Another cause is related to its less accurate modeling of the evanescent wave excitation at strongly reflecting interfaces. This conclusion can be found from the Fig. 1 and Fig. 2 presented in [88], where the discussion is particularly for the single reflection problem. We also notice that the rotated branch cut Padé and the complex coefficient Padé with rotated branch cut exhibit very close performance. It is shown that the Padé order (6, 6) is sufficient to obtain a good accuracy for both of them. Therefore, in the simulation of multiple strongly reflecting structures, we prefer to use the rotated branch cut Padé to approximate the square root operator, as it offers good accuracy and avoids the computational load for calculating the complex coefficients.

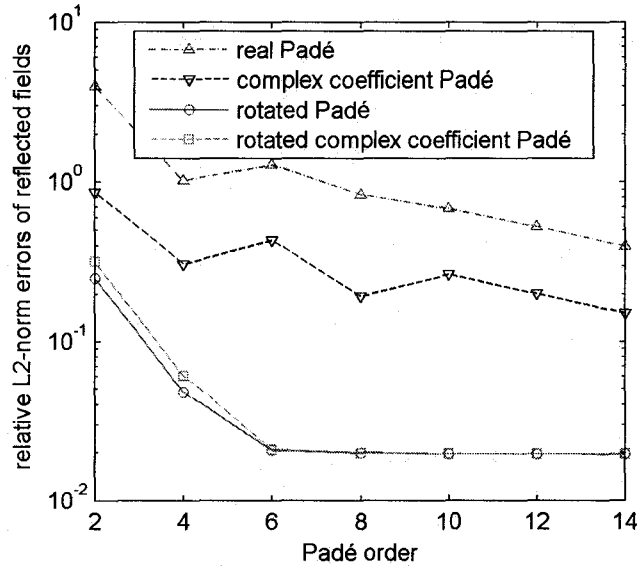
real Padé
complex coefficient Padé
rotated Padé
rotated complex coefficient Padé
relative L2-norm errors of reflected fields
Padé order
10^{1}
10^{0}
10^{-1}
10^{-2}
2
4
6
8
10
12
14

(a)

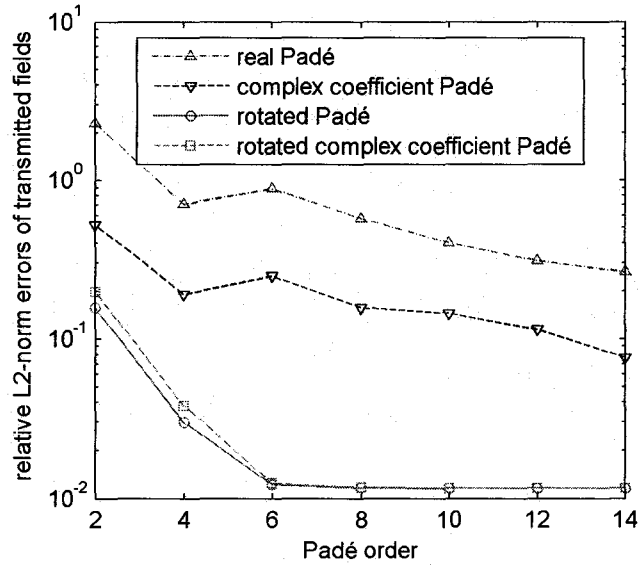
real Padé
complex coefficient Padé
rotated Padé
rotated complex coefficient Padé
relative L2-norm errors of transmitted fields
Padé order
10^{1}
10^{0}
10^{-1}
10^{-2}
2
4
6
8
10
12
14

(b)

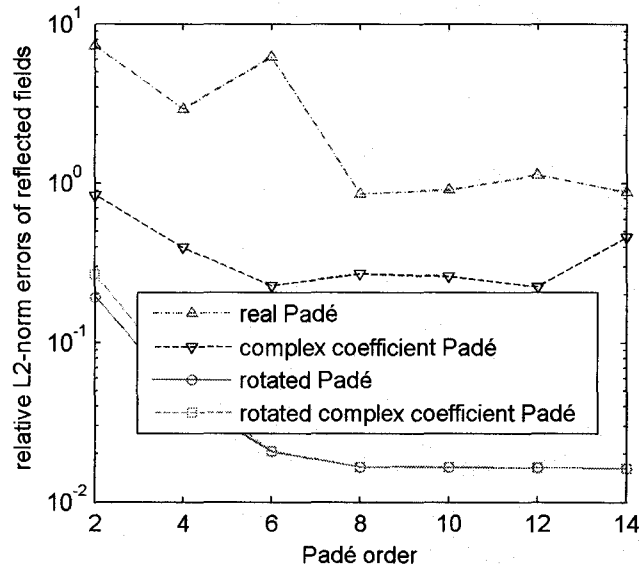

(c)

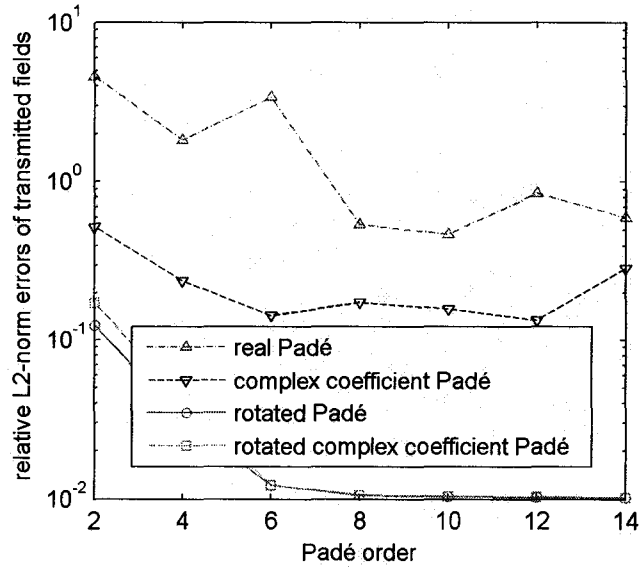

(d)

Figure 7.5 Relative L2-norm errors of the calculated fields obtained from various Padé-type approximations. (a) reflected field for TE; (b) transmitted field for TE; (c) reflected field for TM; (d) transmitted field for TM.

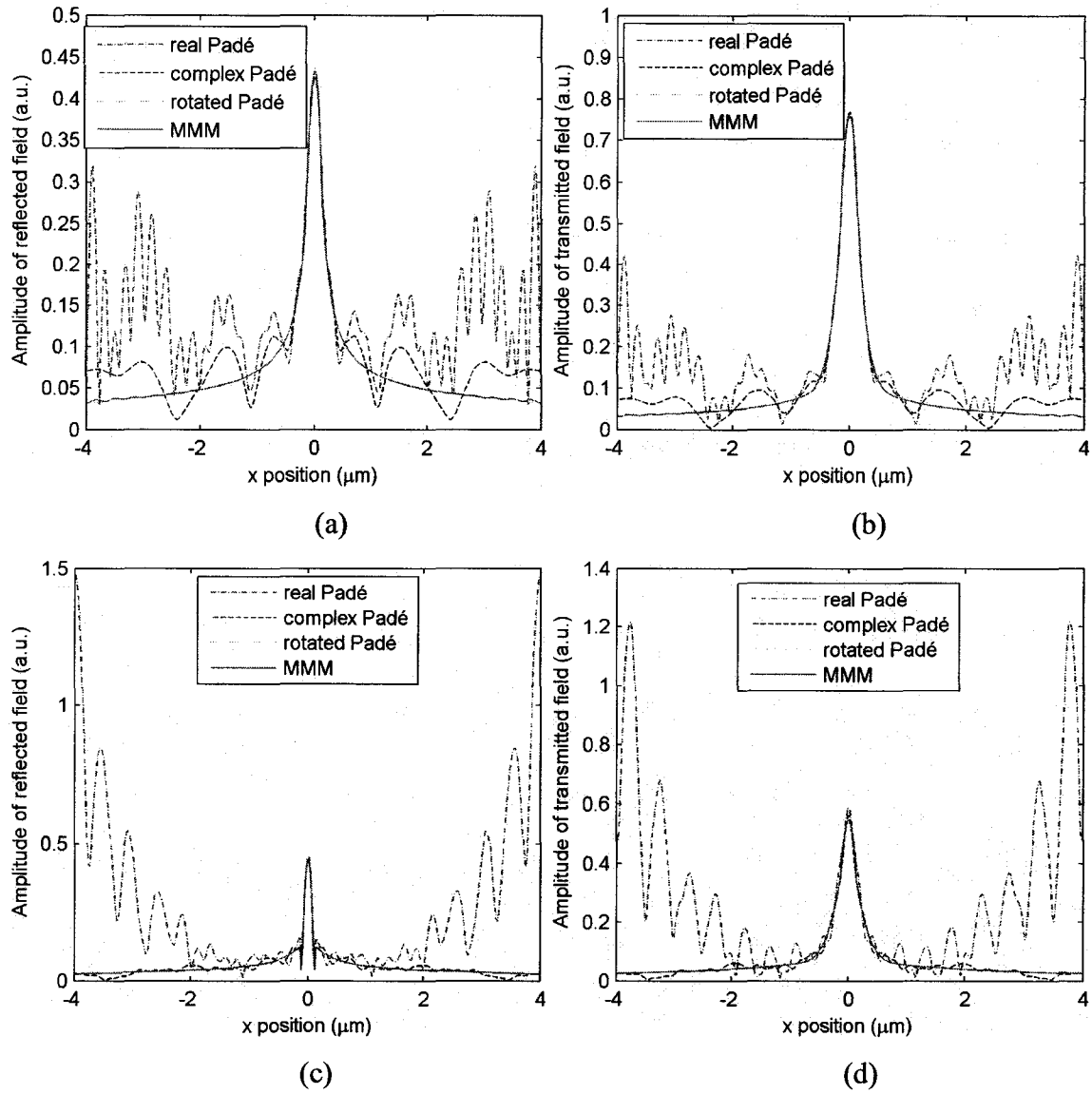

Figure 7.6 Field patterns obtained from various Padé-type approximations. (a) the reflected field for TE; (b) the transmitted field for TE; (c) the reflected field for TM; (d) the transmitted field for TM. "Complex Padé" and "MMM" represent complex coefficient Padé and the mode matching method, respectively. The Padé order (6, 6) is employed in all calculations. The field patterns obtained from the complex coefficient Padé with rotated branch cut coincide with that of the rotated branch cut Padé and are omitted here.

Finally, we evaluate various Padé approximations in an intuitive manner by comparing the field patterns. In Figure 7.6, strong oscillations are observed in the field pattern

obtained from the real Padé. In contrast, the oscillations in the field patterns produced by the complex coefficient Padé are greatly suppressed. In particular, the field pattern given by the rotated branch cut Padé has an excellent agreement with the reference solution. These observations are consistent with the conclusion drawn from the Figure 7.5.

E. Effect of Longitudinal Index Contrast

We now examine the behaviours of various Padé approximations in reflective structures with different longitudinal index contrast. The evanescent modes will be excited in different levels by adjusting the core index of the gap region n_{1g}. The higher the longitudinal index contrast, the more the evanescent modes will be excited. We calculate the relative L2-norm errors of the transmitted field for different core indexes of the gap region varying from 1.45 to 3.3. All the calculations are based on the optimal settings: Padé order is (8, 8), $\beta = -1$ for the complex coefficient Padé, and $\alpha = \pi/2$ for the rotated branch cut Padé. In Figure 7.7, for all the three types of Padé approximations, the field errors are observed to decrease gradually with decreasing the longitudinal index contrast (increasing n_{1g}). In the case of $n_{1g} = 3.3$, the real Padé can even achieve a fair accuracy, which is also verified by examining the field patterns. This observation indicates that the requirement for the complex-valued approximation to square root operators becomes less demanding in weakly reflecting structures. We particularly compare the field errors given by the real Padé and the rotated branch cut Padé in two extreme cases. For $n_{1g} = 3.3$, the former is 3.9 and 2.5 times greater than the latter for TE

and TM, respectively. In contrast, for $n_{1g}=1.45$, the corresponding values become 47.9 and 50.1. Therefore, we have clearly demonstrated the necessity and significance of accurately modeling the evanescent modes in strongly reflecting structures, and it is apparently revealed that the rotated branch cut Padé approximation has the best performance in doing so.

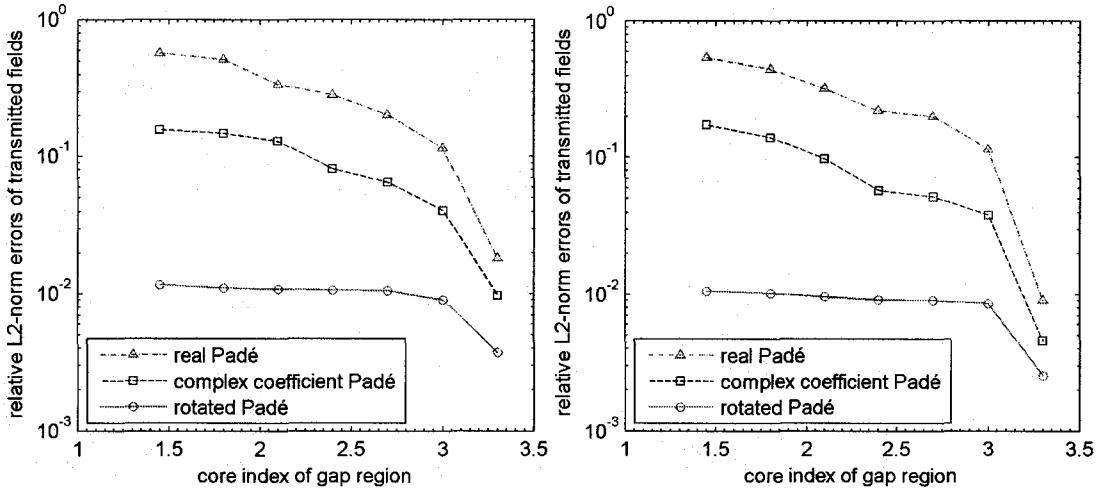

Figure 7.7 Relative L2-norm errors of transmitted fields obtained from various Padé-type approximations for different longitudinal index contrasts. (a) TE; (b) TM.

7.4 Assessment of High-Order BiBPM

In this section, to illustrate the improvement in accuracy and efficiency of the higher-order BiBPM, a one-dimensional (1D) photonic crystal slab (PCS) with a single defect (i.e., phase-shift) [99] is simulated. This structure consists of alternating layers of two different symmetric slab waveguide segments with high index contrast in transverse direction, as shown in Figure 7.8.

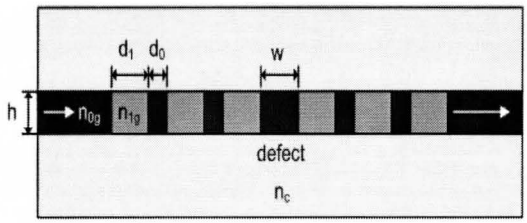

Figure 7.8 Schematic diagram of 1D photonic crystal slab waveguide (PCSW).

The two different waveguide segments have common cladding index $n_c = 1.45$, and different core indexes $n_{0g} = 3.4$ and $n_{1g} = 2.518$, respectively. The widths of the two quarter-wavelength segments are $d_0 = 0.1354$ μm and $d_1 = 0.1913$ μm, respectively. The width of the half-wavelength defect is $w = 2 \cdot d_0$. The core thickness is $h = 0.25$ μm. The transmission spectra of the fundamental TE mode of the input and output waveguides for the structure consisting of four periods on either side of the middle defect are calculated by the two finite-difference schemes (the conventional FD2 and the improved FD4) for different mesh sizes. Parameters used in the simulations are summarized as follows: the computational window size is 6.75 μm including a perfectly matched layer (PML) of 0.25 μm thickness on each side; the longitudinal step sizes in n_0 and n_1 regions are $\Delta z_0 = 0.01354$ μm and $\Delta z_1 = 0.01913$ μm, respectively; the reference index is chosen to be the effective index of the corresponding waveguide segment. The real Padé (4, 4) approximant is used in combination with a rotated angle $\alpha = \pi / 3$ for both the scattering operators $R(z)$ and $T(z)$ and the propagator P_j which is further approximated with $q = 2$.

In order to provide a benchmark for the comparison between the FD2- and FD4-based BiBPMs, the same calculation for each case is performed by a rigorous mode matching method (MMM) based on the scattering matrix. We employ 80 modes which are calculated by a mode solver based on the FD4 formula with a fine mesh ($\Delta x = 0.0125$ μm) and therefore offer highly accurate and reliable results as the benchmark.

To illustrate the improvement in accuracy for the FD4-based BiBPM over the FD2-based method, we first calculate the transmission spectra of the fundamental TE mode using both methods. We examine the position of the central wavelength at which the transmission is maximum, which is a good measure of accuracy in the simulated phases of the counter-propagation fields. Figure 7.9 presents the spectra covering the wavelength range from 1.45 μm to 1.65 μm with a resolution of 5 nm obtained by three different mesh sizes. It is observed that when a fine mesh $\Delta x = 0.025$ μm is used, both methods provide accurate prediction of the central wavelength. As the mesh size increases, considerable shift of the central wavelength from the correct value is observed for the FD2 scheme, whereas the value predicted by the FD4 method remains unchanged at 1.545 μm even in the case of a rather coarse mesh of $\Delta x = 0.125$ μm. Moreover, the spectra obtained by the FD4 method is found to be in good agreement with the MMM calculations in all cases.

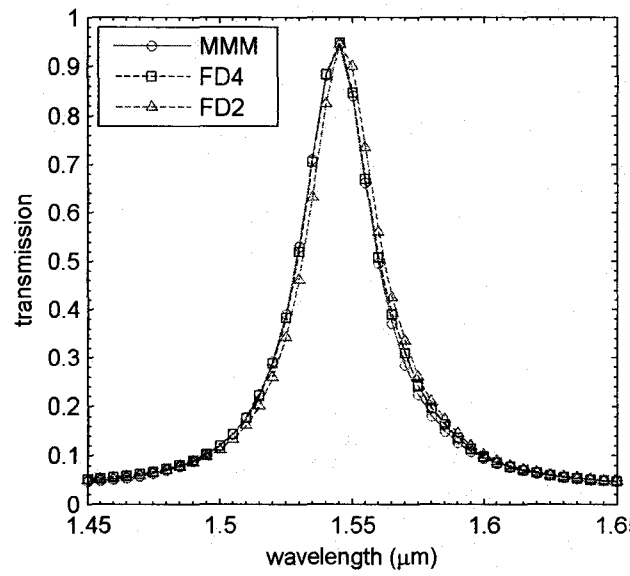
MMM
FD4
FD2
transmission
wavelength (μm)
0
0.1
0.2
0.3
0.4
0.5
0.6
0.7
0.8
0.9
1
1.45
1.5
1.55
1.6
1.65

(a)

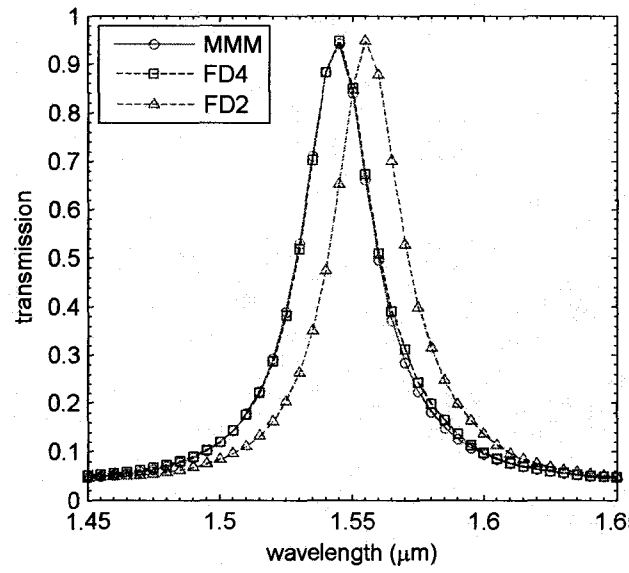
MMM
FD4
FD2
transmission
wavelength (μm)
0
0.1
0.2
0.3
0.4
0.5
0.6
0.7
0.8
0.9
1
1.45
1.5
1.55
1.6
1.65

(b)

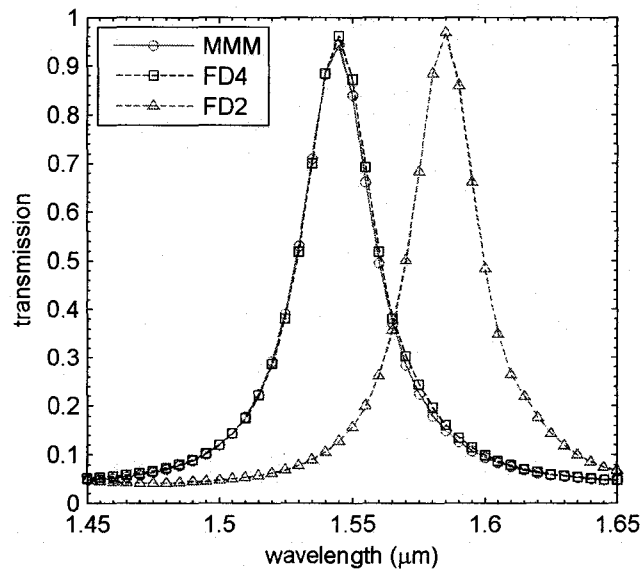

(c)

Figure 7.9 Transmission of the fundamental TE mode calculated by FD2- and FD4-BiBPMs employing different mesh sizes. (a) $\Delta x = 0.025$ μm; (b) $\Delta x = 0.0625$ μm; (c) $\Delta x = 0.125$ μm.

Furthermore, we calculate the central wavelength with a very fine wavelength resolution 1 nm as a function of mesh size using both the FD2 and the FD4 methods, as presented in Figure 7.10. It is clearly shown that, to obtain a converged solution, the FD4 only need a coarse mesh $\Delta x = 0.125$ μm, whereas the FD2 requires 10 times smaller mesh size $\Delta x = 0.0125$ μm. Therefore, we conclude from Figure 7.9 and 7.10 that the use of the FD4 scheme improves significantly the accuracy of the BiBPM, especially when a coarse mesh is employed in the high index contrast waveguides. The remarkable high accuracy in predicting the central wavelength is achieved by the FD4 results is due to its higher phase-accuracy warranted by the proper treatment of interface conditions and the inclusion of more terms in the Taylor series expansion of the spatial second derivatives.

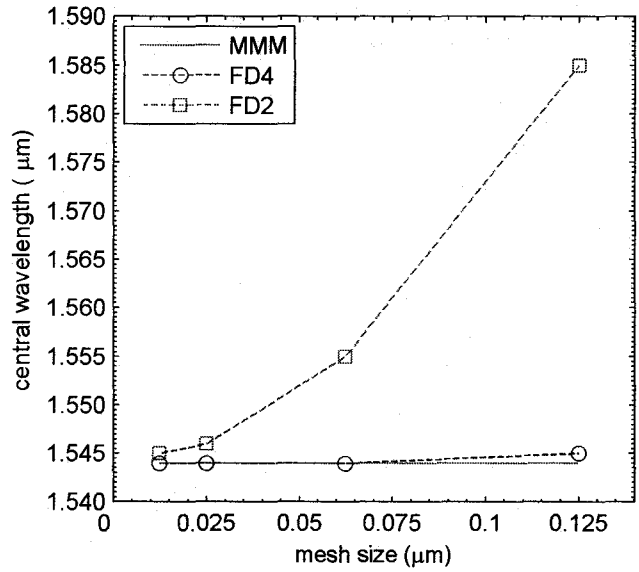

Figure 7.10 Central wavelengths calculated by FD2 and FD4 methods for TE as a function of mesh size.

In addition, we also examine the field distribution through the structure by following a procedure outlined in [100]. The total electric field distributions for the central wavelength 1.544 μm are plotted for both the FD2 and FD4 schemes employing $\Delta x = 0.125$ μm in Figure 7.11. For comparison, the field distribution by the FD4 scheme using a fine mesh $\Delta x = 0.025$ μm is also shown in Figure 7.11(c). The longitudinal standing-wave pattern obtained by the coarse FD2 is shown to concentrate in the input section of the grating, indicating a strong reflection [Figure 7.11(a)]. This is in contrast with the field distribution obtained by the FD4 with the same mesh which shows almost symmetric standing-wave patterns for the grating sections on the two sides of the defect region [Figure 7.11(b)]. As we know that the reflection should cancel with each other at the central wavelength, resulting a total transmission, the simulation results by FD2 with

the coarse mesh is therefore wrong. On the other hand, the FD4 does produce the correct field pattern, which is also verified by comparison with the calculation based on fine mesh FD4 in Figure 7.11(c).

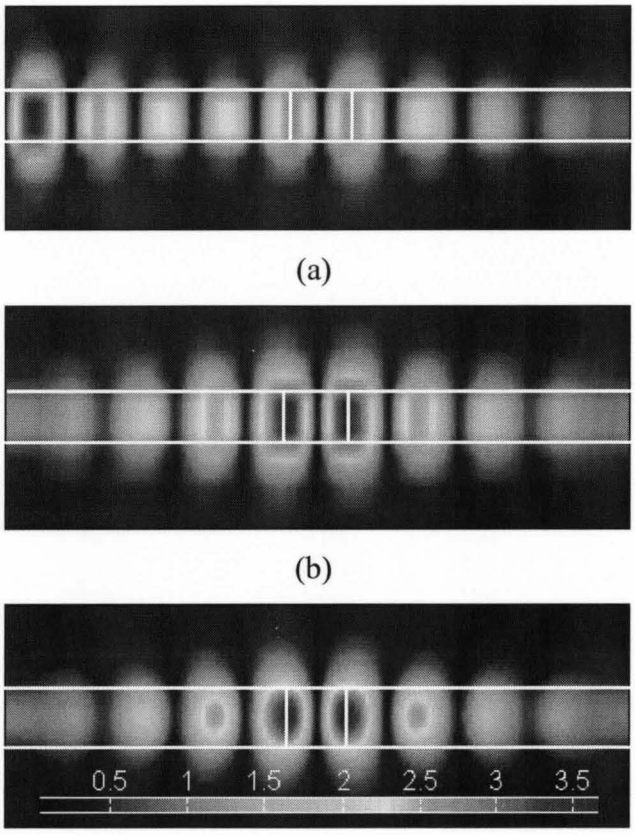

(a)

(b)

(c)

Figure 7.11 Total electric field distribution through the 1D PCS structure at central wavelength 1.544 μm. (a) FD2 with $\Delta x = 0.125$ μm; (b) FD4 with $\Delta x = 0.125$ μm; (c) FD4 with $\Delta x = 0.025$ μm. The horizontal and vertical white lines indicate cladding-core interfaces and edges of the middle defect, respectively. The color bar is the same for all the plots.

Further, we examined the computation efficiencies of the two FD BiBPMs. Table 7.1 summarizes the computation time and the number of grid points required for both FD2 and FD4 methods with different mesh sizes. All the calculations are performed on a

3.2 GHz Pentium PC. For the sake of comparison, the predicted central wavelength in each case is also listed in Table 7.1. We note that, for the same mesh size, the FD4 does not significantly increase the computation time in comparison with the FD2 as they both compute tri-diagonal matrices due to the three-point finite-difference formulas. The slight increase in the computation time of the FD4 is attributed to the increased complexity of generating the matrix elements. On the other hand, to achieve a comparable accuracy indicated by the central wavelength, the computation time and the number of grid points required for the FD4 are much less than those for the FD2. More specifically, the FD2 requires $\Delta x = 0.025$ μm to predict the central wavelength with a reasonable accuracy. In contrast, the FD4 only need a coarse mesh $\Delta x = 0.125$ μm, leading to 98% saving in computation time and 80% saving in memory. Considering the fact that the efficiency of the BiBPM based on scattering operators is more dependent on the number of grid points, the saving in computation time and memory is quite significant and highly desirable.

Mesh size (μm)	Number of grid points	Method	Computation time (s)	Calculated central wavelength (μm)
0.0125	540	FD2	189.547	1.545
		FD4	240.875	1.544
0.0250	270	FD2	27.907	1.546
		FD4	33.141	1.544
0.0625	108	FD2	2.079	1.555
		FD4	2.484	1.544
0.1250	54	FD2	0.360	1.585
		FD4	0.469	1.545

Table 7.1 Comparison of the computational cost for FD2- and FD4- BiBPM.

Finally, we investigate the performance of the FD4-BiBPM for the TM polarization. Note that the waveguide structure used in Figure 7.8 has a strong index contrast and is thus highly polarization sensitive. For this reason, we design a periodic grating reflector with 32 periods as the example for TM polarization. The lengths of the two grating sections of quarter-wavelength for the TM modes are chosen to be $d_0 = 0.1809$ μm and $d_1 = 0.2389$ μm, respectively and the other parameters are the same as those in Figure 7.8. We plot the reflection spectra of the fundamental TM mode using both FD2 and FD4 methods in Figure 7.12, where the longitudinal step sizes $\Delta z_0 = 0.01809$ μm and $\Delta z_1 = 0.02389$ μm are used and the other simulation parameters are the same as in TE case. A period doubling process [38] is used to speed up the calculation. Again, it is seen that the reflection spectra calculated by the FD2 are considerably shifted with the increase of mesh size and that the central wavelength calculated by FD4 is kept at 1.550 μm in all cases. We also observe a slight increase in the amplitude of reflection calculated by both methods with the increase of mesh size. This implies that the numerical dissipation is more acute to the mesh size for TM polarization.

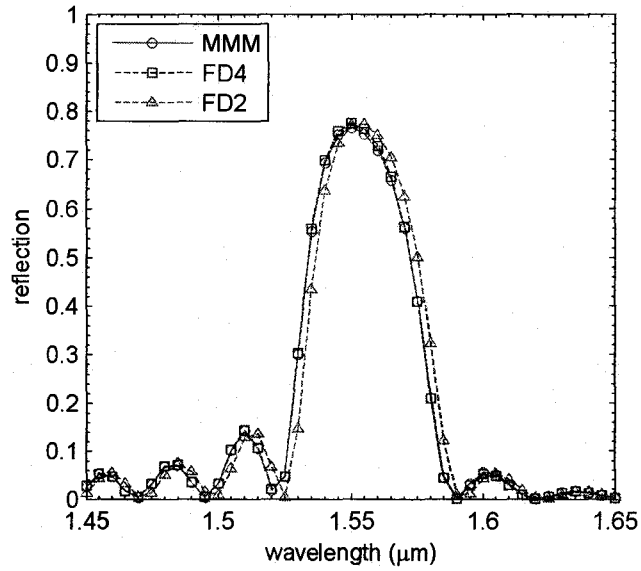
MMM
FD4
FD2
reflection
wavelength (μm)
1
0.9
0.8
0.7
0.6
0.5
0.4
0.3
0.2
0.1
0
1.45
1.5
1.55
1.6
1.65

(a)

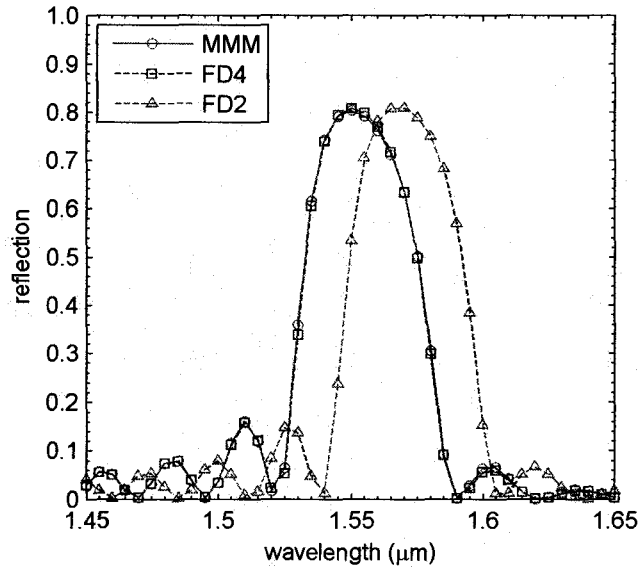
MMM
FD4
FD2
reflection
wavelength (μm)
1.0
0.9
0.8
0.7
0.6
0.5
0.4
0.3
0.2
0.1
0
1.45
1.5
1.55
1.6
1.65

(b)

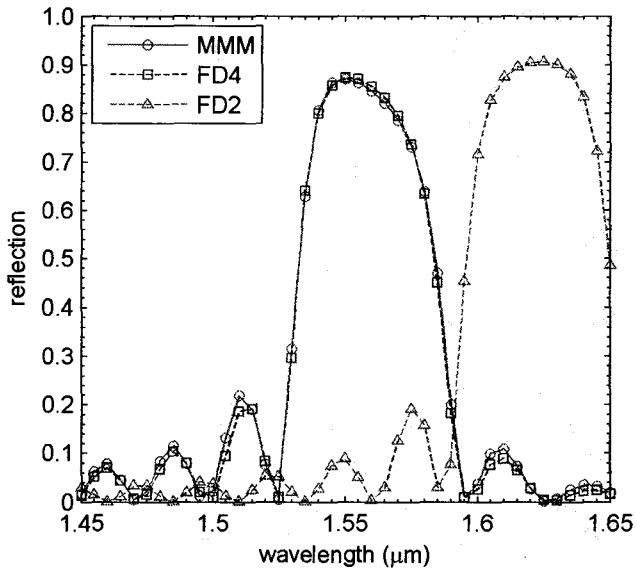

(c)

Figure 7.12 Reflection of the fundamental TM mode calculated by FD2- and FD4-BiBPMs employing different mesh sizes. (a) $\Delta x = 0.025$ μm; (b) $\Delta x = 0.0625$ μm and MMM using the same mesh size; (c) $\Delta x = 0.125$ μm and MMM using the same mesh size.

The central wavelengths determined by 1nm wavelength resolution as a function of mesh size for the TM polarization are plotted in Figure 7.13. A similar conclusion to the TE case can be drawn. Moreover, the central wavelength shift observed for the TM polarization is more pronounced than that for the TE polarization when the FD2 is used. Therefore, the advantage of the FD4 is more pronounced for TM polarizations. We also examine the field distribution and compare the computational costs of FD2 and FD4 methods for the TM polarization, reaching a similar conclusion to the TE case.

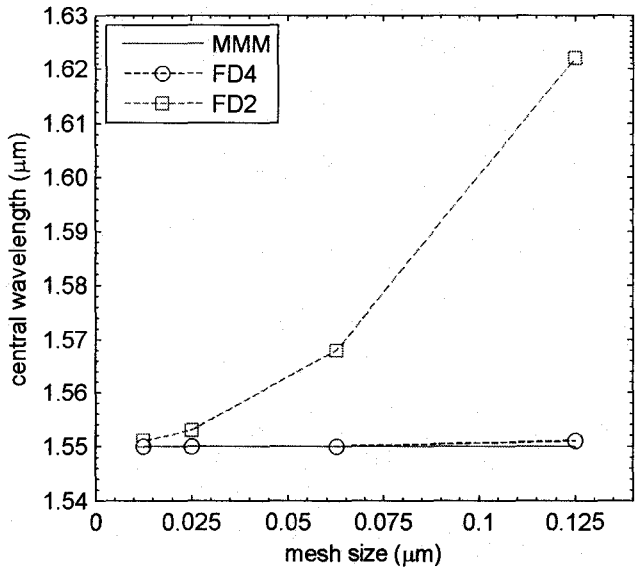

Figure 7.13 Central wavelengths calculated by FD2 and FD4 methods for TM as a function of mesh size.

7.5 Summary

In this chapter, we have developed a highly accurate and efficient bidirectional beam propagation method by using the fourth-order accurate finite-difference formula. The method is demonstrated to be able to save considerable computational cost without sacrificing accuracy in the analysis of high index contrast segmented waveguides.

With the help of the high-order BiBPM, we have demonstrated the insufficiency of the real-valued Padé approximant for approximating square root operators and the much better performance achieved by the complex-valued Padé approximants. Some salient features of the complex-valued Padé approximants are illustrated. It is demonstrated that the performance of the rotated branch cut Padé approximant becomes stable when the rotation angle is greater than $\pi/4$. It is found that the complex

coefficient Padé approximant with $\beta = -1$ can represent square root operator most accurately. A comparative assessment of various Padé approximants is carried out by calculating the relative L2-norm errors of the reflected and transmitted fields for both TE and TM waves. It is concluded that the rotated branch cut Padé approximant is preferred for both the transition and propagation operators to accurately model the evanescent and propagating waves in strongly reflective structures. The Padé order (6, 6) is sufficient to offer a good accuracy. It is also revealed that the requirement for the complex representation of square root operators becomes less demanding with decreasing the longitudinal index contrast.

Chapter 8

Design of Bragg Gratings on High Index Contrast and Surface Plasmonic Waveguides by High-Order BiBPM

8.1 Introduction

Bragg gratings are important building blocks for many optical devices. They have found broad applications in distributed feedback and distributed Bragg reflection lasers, grating-assisted frequency selective waveguide filters, sensors, etc. Bragg gratings are typically formed by introducing periodic index corrugations in the waveguide axis. Light confinement is ensured in the transverse direction by the index contrast provided by guided and cladding layers. The mode propagating along the axis experiences the periodic variation of the dielectric properties, giving rise to the band structure that governs device operation in both transmission and reflection. The conventional Bragg gratings are usually etched shallowly, leading to weak index corrugations. Such gratings can be accurately analyzed by the standard coupled-mode theory (CMT) [10][11], because significant power exchange occurs between the forward and backward guided modes. For Bragg gratings with strong index corrugations, the CMT based on the coupling of two counter-propagating modes becomes less applicable, and more rigorous methods have to

be used, such as the bidirectional beam propagation method (BiBPM) [34], the mode-matching method (MMM) [101] and the finite-difference time-domain (FDTD) method.

In the design of Bragg gratings, one critical step is to determine the lengths of the "tooth" and "groove" sections so as to reach the Bragg wavelength at which the constructive interference between the forward and the backward propagating waves occurs. Originally it is believed that the lengths should be chosen as quarter-wavelength sections, leading to a phase shift of $\pi/4$ for the propagating modes in each section. The design based on the above rule shows, however, that the maximum reflectivity can be reached for wavelength slightly shorter than the desired Bragg wavelength [101]. It is also found that the blue shift of the peak wavelength from the desired Bragg wavelength becomes more pronounced with increasing the index corrugation. This phenomenon precludes the accurate design of Bragg gratings with strong index corrugations. In this chapter, we develop an efficient iteration method in the context of BiBPM for achieving the desired peak wavelength to a large degree of accuracy.

Another interest of this chapter is the Bragg gratings based on surface plasmonic waveguides which have attracted much attention recently. The extensive study of plasmonic waveguides is driven by the increasing demand for highly integrated photonic circuits. Surface plasmonic waveguides consisting of metal-dielectric interfaces exhibit promising potentials in nanophotonic applications [102]. As an appealing feature, surface plasmonic waveguides can propagate the optical signals and carry electrical signals by using the same metal stripe. In fact, surface plasmonic polaritons (SPPs) were known in the field of surface science in the 1950s [103]. The study of SPPs has attracted much

interest in recent years in the field of photonics due to the advances of the technology that allows metals to be structured and characterized on the nanometer scale.

Different from conventional optical waveguides where the optical fields concentrate on the dielectric medium sandwiched between two dielectric layers of lower refractive index, surface plasmonic waveguides guide surface polaritons along metal-dielectric interfaces. The excitation mechanism forces free electrons of the metal to fluctuate collectively in resonance with the electromagnetic wave. The interaction between the surface charge fluctuations and the electromagnetic fields forms the SPPs. Another consequence of this interaction is the metal absorption loss. For a semi-infinite metal, the SPP is strongly bounded to the single metal-dielectric interface, leading to a strong absorption in metals. Therefore, the propagation length of the SPP is limited. For thin metal films embedded in two identical dielectric layers, there exist two modes, namely, symmetric mode and anti-symmetric mode, arising from the coupling between the surface polaritons waves traveling on each interface. The symmetric mode is the solution in which the transverse magnetic field does not exhibit a zero inside the metal film [71]. The symmetric field distribution results in a small field concentration inside the metal film, and therefore achieves low metal absorption. It has been verified that the attenuation of the symmetric mode decreases with decreasing the film thickness. The symmetric mode can propagate the SPP in a useful distance and is called long-range SPP (LR-SPP) [104].

The thin metal films embedded in dielectric supporting LR-SPP offers a unique alternative for guiding the light over long propagation distances. A number of photonic

components, such as straight and bend waveguide, splitters, and directional couplers, have been realized experimentally by utilizing the LR-SPP waveguides. More recently, much attention has been paid to the theoretical and experimental studies of Bragg gratings based on LR-SPP [105]-[107]. So far, the theoretical method used to study the LR-SPP based Bragg gratings is the Lippmann-Schwinger integral equation method [107], which is less straightforward for designers. In this chapter, with the help of the high-order BiBPM developed in the previous chapter, we study the propagation characteristics of the LR-SPP in the Bragg gratings consisting of a thin metal film embedded in dielectric medium and an array of equidistant metal ridges on each side of the film.

8.2 Design of Bragg Gratings with Strong Index Corrugations

8.2.1 Conventional Design Method

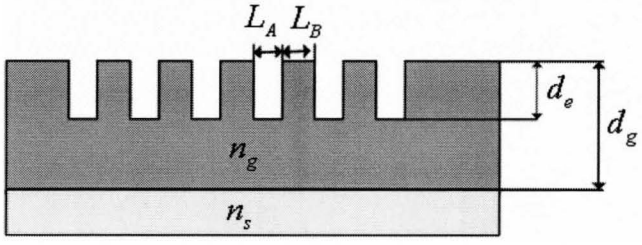

Figure 8.1 A typical Bragg grating structure consisting of two-element unit cells.

A typical Bragg grating structure is schematically depicted in Figure 8.1. The lengths of groove and tooth sections are denoted by L_A and L_B, respectively. In the design of such a grating, one critical procedure is to determine L_A and L_B such that the

grating acts as a filter or reflector at the desired peak wavelength λ_B. The lengths of L_A and L_B are given as

$$\begin{aligned} L_A &= \lambda_B / 4N_A \\ L_B &= \lambda_B / 4N_B \end{aligned} \tag{8.1}$$

where N_A and N_B refer to the effective indices of groove and tooth sections, respectively. As we mentioned before, the design based on Eq.(8.1) leads to a peak wavelength slightly shorter than the desired Bragg wavelength. To illustrate this effect, we consider a very deeply etched grating with a rectangular profile created on a single mode planar waveguide [101], as shown in Figure 8.1. The refractive indices for the guiding and substrate layers are n_g=1.53 and n_s=1.52, respectively. The cladding and groove regions are filled with air. The thickness of the guiding layer is $d_g = 2.4$ μm. The etching depth is $d_e = 0.5$ μm. The desired Bragg wavelength is $\lambda_B = 0.65$ μm. The lengths of groove and tooth sections are designed as $L_A = 0.106553$ μm and $L_B = 0.106456$ μm, respectively. The number of periods is 1793.

The reflection and transmission spectra of the fundamental TE mode are calculated by the high-order BiBPM and illustrated in Figure 8.2. Simulation parameters are summarized as follows: the computational window size is 15 μm including a perfectly matched layer (PML) of 1 μm thickness in cladding and a PML of 4 μm thickness in substrate; the mesh size is $\Delta x = 0.1$ μm; the Padé (4, 4) approximation with a rotation angle of $\pi/3$ is used in the BiBPM. As can be seen in Figure 8.2, both the reflection peak

and transmission valley are reached at the wavelength of 0.6498 μm instead of the desired wavelength of 0.65 μm.

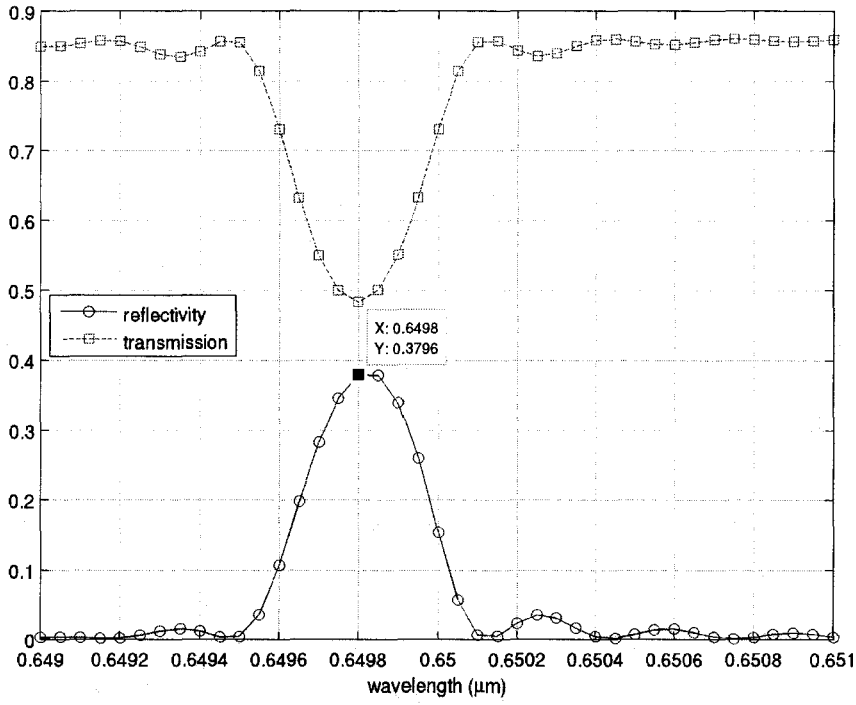

Figure 8.2 Reflection and transmission spectra of the fundamental TE mode.

This behaviour can be qualitatively explained by the following consideration [101]. In a single-mode waveguide with an effective refractive index N, the relation $\lambda_B = 2N\Lambda$ holds between the Bragg wavelength and the grating period length Λ. If the groove of the grating is deep, higher-order (in fact, radiation) modes also participate in the energy transfer. As their refractive indices are lower than N, it leads to an effective shortening of the Bragg wavelength.

8.2.2 Iteration Method

The above analysis has clearly demonstrated that the peak wavelength of the strongly corrugated gratings is shifted from the conventional Bragg wavelength based on the fundamental local modes of the waveguide. However, it is still not clear how to design the grating period for a given index corrugation so that we can realize the reflection peak at a given wavelength. In this subsection, we develop an efficient iteration method in the context of high-order BiBPM to resolve that problem.

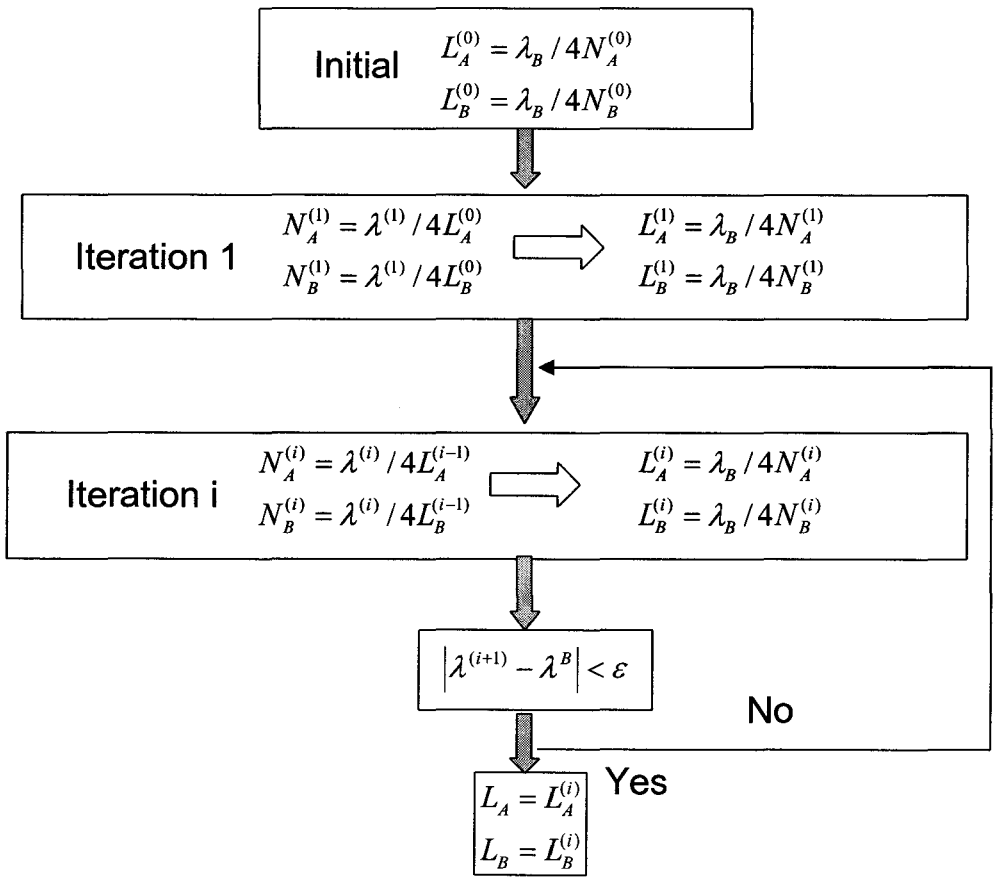

Figure 8.3 A flow chart for the iteration method in design of deep gratings.

A flow chart for the iteration method is shown in Figure 8.3. The basic idea of this iteration method is to find the overall effective indices of the groove and tooth sections. The initial values are chosen as the effective indices of the fundamental mode in each section. More accurate values can be obtained from the observed peak wavelength by using Eq.(8.1). Subsequently, we start a new design based on the updated effective indices. This procedure is repeated until the desired peak wavelength is reached.

In order to demonstrate the effectiveness of this iteration method, we determine the lengths L_A and L_B for the previous example following the procedure shown in Figure 8.3. Figure 8.4 shows the reflection and transmission spectra of the fundamental TE mode after two iteration with $L_A = 0.106586$ μm and $L_B = 0.106489$ μm. It is clearly shown that both the reflection peak and transmission valley occur at the wavelength of 0.65 μm. Therefore, the new iteration method can achieve the desired design in two iterations.

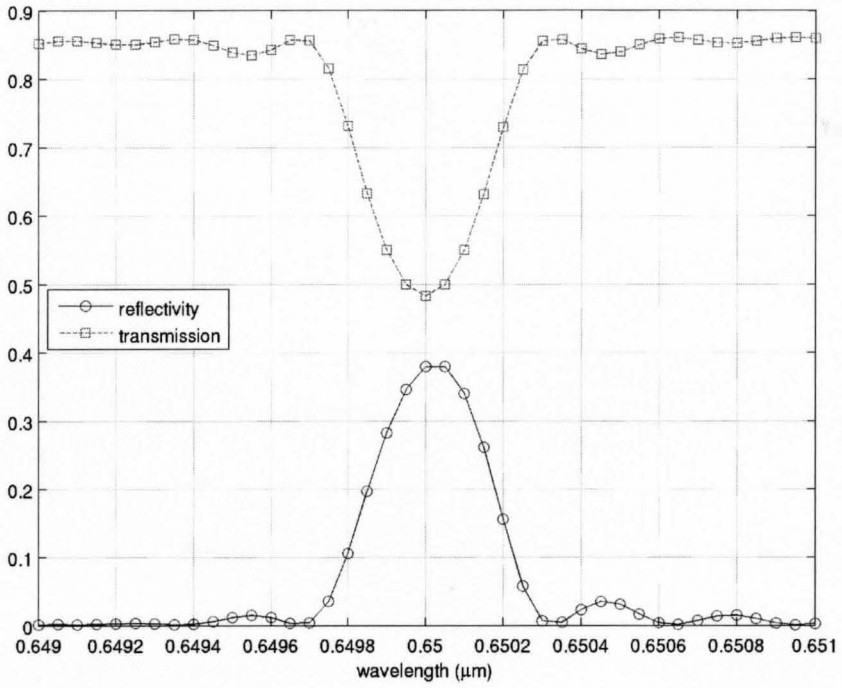

Figure 8.4 Reflection and transmission spectra of the fundamental TE mode.

To validate the iteration method for TM polarizations, we illustrate the design process for the 1D photonic crystal slab waveguide used in Figure 7.12. Its structure is shown in Figure 8.5, where $n_c = 1.45$, $n_{0g} = 3.4$ and $n_{1g} = 2.518$; the core thickness is $h = 0.25$ μm and the number of periods is 32. The desired peak wavelength is 1.55 μm.

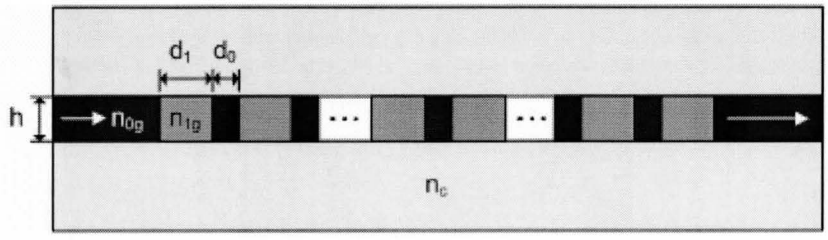

Figure 8.5 Schematic diagram of 1D photonic crystal slab waveguide.

Figure 8.6 illustrates the design process using the iteration method. If we determine the lengths of d_0 and d_1 sections following the conventional method, i.e., $d_0 = 0.17392$ μm and $d_1 = 0.22972$ μm, the resulting peak wavelength is found to be 1.51 μm [Figure 8.6(a)], which is considerably shifted from the desired wavelength of 1.55 μm. By using the iteration method, the section lengths converge at $d_0 = 0.1809$ μm and $d_1 = 0.2389$ μm after four iterations, resulting in the desired peak wavelength of 1.55 μm [Figure 8.6(d)].

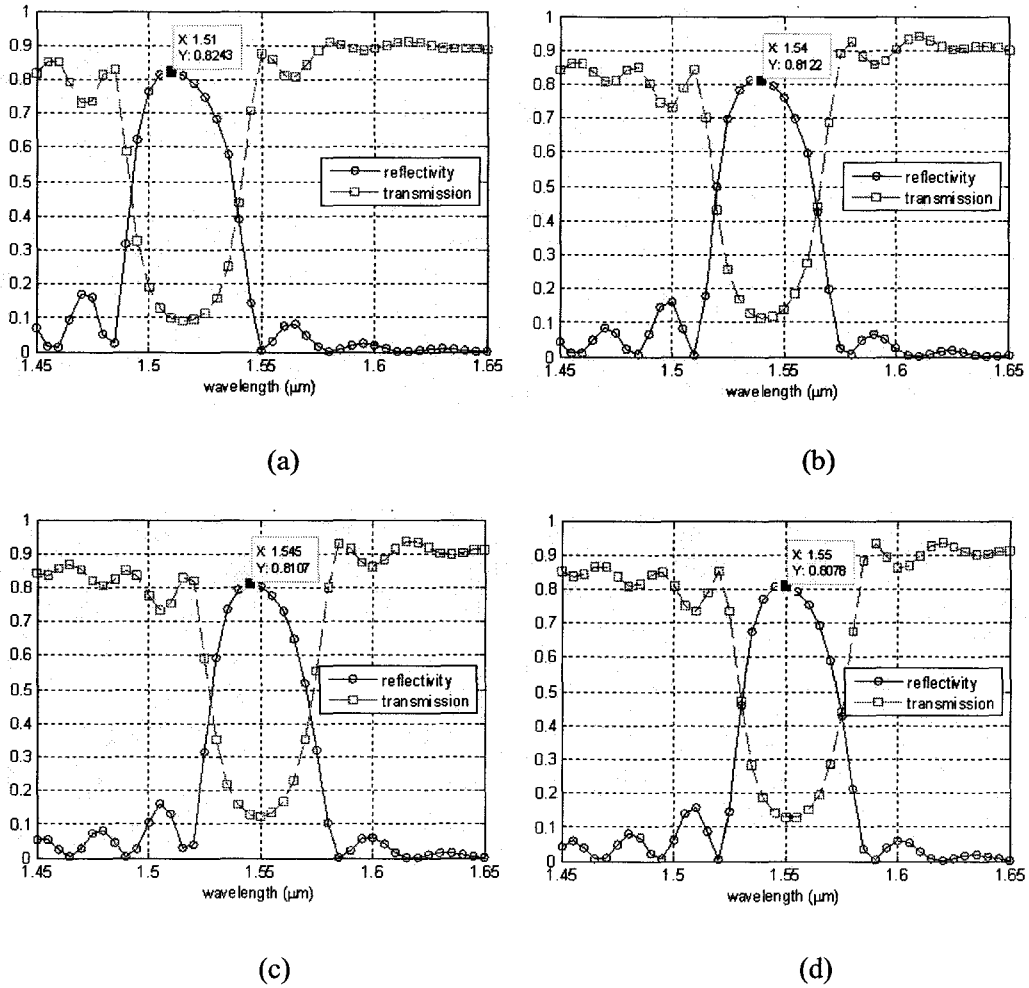

Figure 8.6 Reflection and transmission spectra of the fundamental TM mode. (a) iteration 1; (b) iteration 2; (c) iteration 3; (d) iteration 4.

8.3 Design of Bragg Grating on Surface Plasmonic Waveguides

8.3.1 Characteristics of LR-SPP Mode

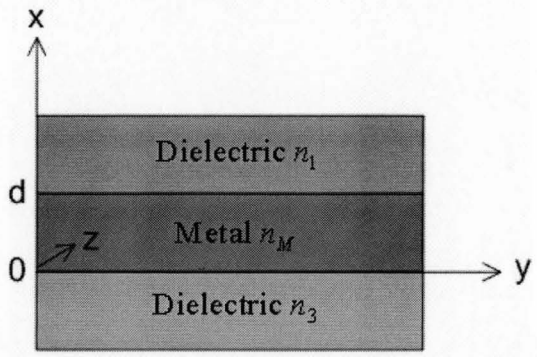

Figure 8.7 Schematic diagram of thin metal film embedded in dielectric.

We first study the characteristics of LR-SPP mode supported by the gold film surrounded by two identical dielectric layers with refractive index $n_1 = n_3 = 1.543$, as shown in Figure 8.7. The complex refractive index of gold is $n_M = 0.55 - 11.5j$ at the wavelength of 1.55 μm. The reason for utilizing the symmetric structure is to support the LR-SPP mode. By using the analytical method presented in chapter 4, the effective index of the LR-SPP mode at the wavelength of 1.55 μm as functions of gold film thickness d is shown in Figure 8.8.

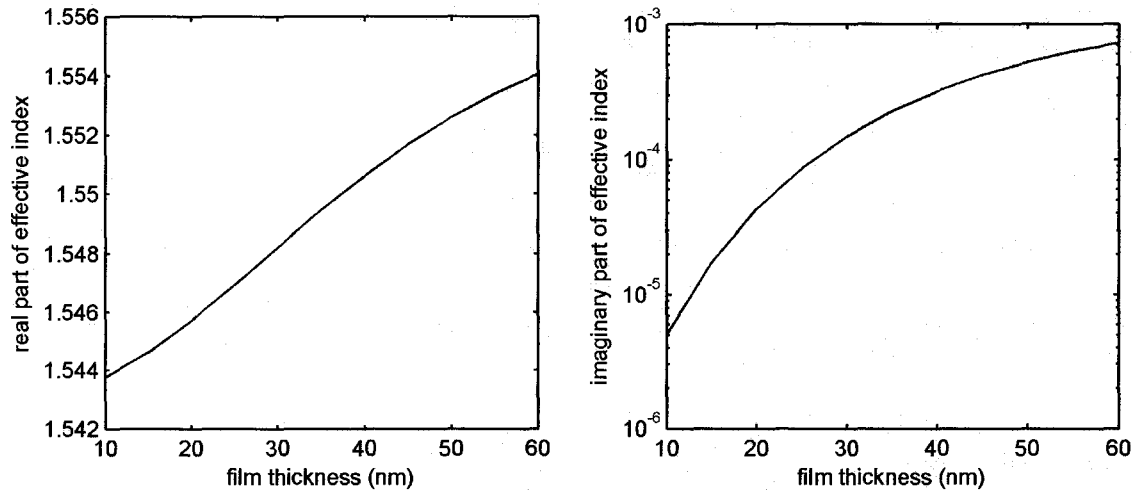

(a) (b)

Figure 8.8 Complex effective index of the LR-SPP mode as a function of film thickness for symmetric structure with $n_1 = n_3 = 1.543$ and $n_M = 0.55 - 11.5j$ at wavelength of 1.55 μm. (a) real part; (b) imaginary part.

It can be seen that both the real and imaginary parts of the effective index decrease with decreasing the film thickness. As we discussed previously, the imaginary part of the effective index determines the absorption loss. The drastic decrease of the imaginary part with shrinking the film thickness observed in Figure 8.8(b) implies that the propagation length of the LR-SPP mode can reach a practically useful scale when the film thickness is small enough. We also plot the LR-SPP mode profile for two different film thickness, i. e., $d = 15$ nm and $d = 60$ nm in Figure 8.9. It is observed that the LR-SPP field associated with $d = 15$ nm penetrates into the dielectric cladding with longer tails in comparison with the one associated with $d = 60$ nm. This reflects that the LR-SPP mode of a thinner metal film is more loosely bound to the metal, leading to the smaller absorption loss and hence longer propagation length.

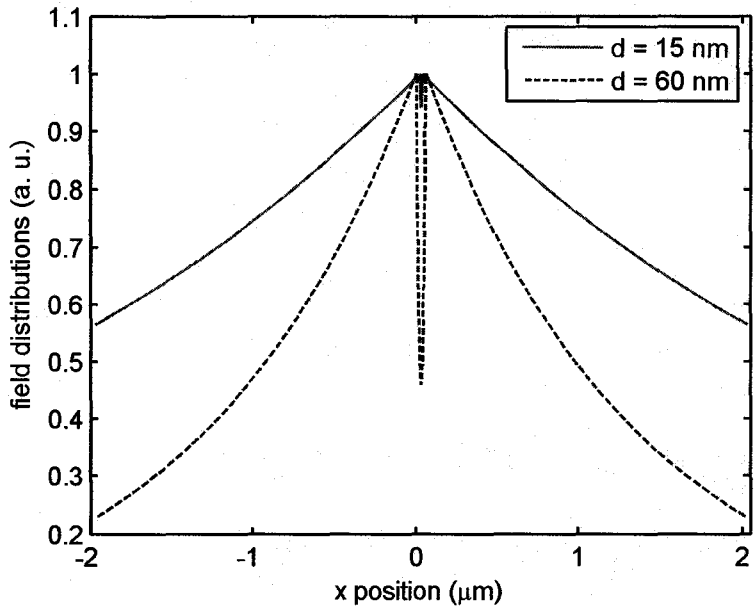

Figure 8.9 Field distributions of the LR-SPP mode supported by the gold film with $d = 15$ nm and $d = 60$ nm.

8.3.2 Analysis of LR-SPP Based Bragg Gratings

In this subsection, we analyze the optical properties of LR-SPP based Bragg gratings by the high-order BiBPM. The LR-SPP grating [107] is composed of a thin gold film embedded in dielectric medium and an array of equidistant gold ridges on each side of the film, as shown in Figure 8.10. The gold thickness is $d = 15$ nm. The grating period is $\Lambda = 500$ nm and the ridge width is $W = 230$ nm. The ridge height is $h = 10$ nm. The refractive index of the gold and the dielectric are $n_M = 0.55 - 11.5j$ and $n_1 = n_3 = 1.543$, respectively.

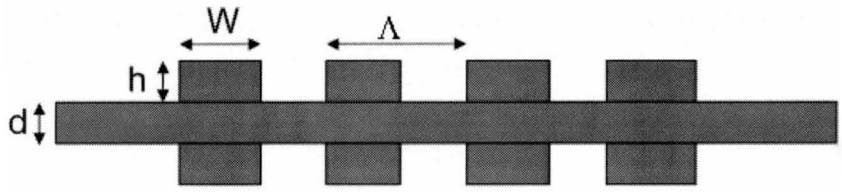

Figure 8.10 Schematic diagram of Bragg grating based on LR-SPP.

As the LR-SPP mode is launched on the input section of the Bragg grating, there will exist reflection into the backward traveling LR-SPP wave and transmission through the grating into the LR-SPP wave. We use the high-order BiBPM to calculate the reflection and transmission spectra of the LR-SPP mode. Parameters used in the simulations are summarized as follows: the transverse mesh size is set as $\Delta x = 0.005$ μm; the longitudinal step sizes in ridge section and non-ridge section are $\Delta z_1 = 0.046$ μm and $\Delta z_0 = 0.054$ μm, respectively; the reference index is chosen to be the effective index of the corresponding waveguide segment. The complex coefficient Padé (8, 8) approximant is used in combination with a rotated angle $\alpha = \pi/2$ for both the scattering operators $R(z)$ and $T(z)$ and the propagator P_j which is further approximated with $q = 2$.

Figure 8.11 shows the reflection and transmission as a function of the wavelength for two LR-SPP gratings with different number of periods $N = 160$ and $N = 256$. The two gratings have the same ridge height $h = 10$ nm. It can be seen from Figure 8.11(a) that both the reflection peak and the transmission valley are around the wavelength of 1.545 μm. This observation is in accordance with the estimation from the well-know Bragg condition. For a weak grating, the Bragg wavelength can be determined by $\lambda_B = 2\Lambda n_{eff}$,

where n_{eff} is the effective index of one period. The mode analysis in the previous subsection shows that the real part of effective index for non-ridge section varies from 1.5447 to 1.5445 in the wavelength range of 1.5-1.6 μm. Thus, the real part of effective index for one grating period is approximately 1.545, leading to an approximate Bragg wavelength of 1.545 μm. Consequently, the Bragg condition verifies the central wavelength calculated by the present high-order BiBPM. The reflection and transmission spectra obtained by our method are close to the earlier results reported in [107]. The same central wavelength is observed for a longer grating, as shown in Figure 8.11(b). It is also shown that the reflection peak and transmission valley are more pronounced in comparison with the shorter grating, which is consistent with the well-know fact.

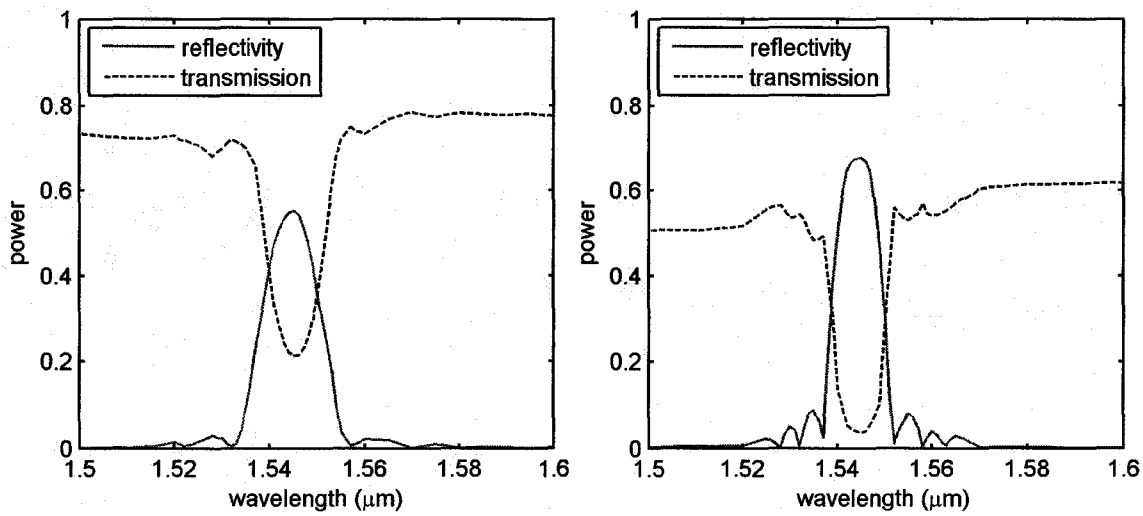

(a) (b)

Figure 8.11 Reflection and transmission spectra of the LR-SPP grating. (a) $N = 160$; (b) $N = 256$.

Figure 8.12 shows the field distributions through the first ten periods for the grating with ridge height $h = 10$ nm and $N = 160$ periods. The field distributions are

shown for three wavelengths: the central wavelength of 1.545 μm, the wavelength of 1.53 μm shorter than the band gap, and the wavelength of 1.57 μm longer than the band gap. As shown in Figure 8.12(b), much stronger reflection is clearly observed for the central wavelength. In contrast, the reflection is very weak for wavelengths out of the band gap (1.53 μm and 1.57 μm). Therefore, the consistency between the field distributions and the reflections quantitatively shown in Figure 8.11 validates the effectiveness of the high-order BiBPM in the simulation of LR-SPP gratings.

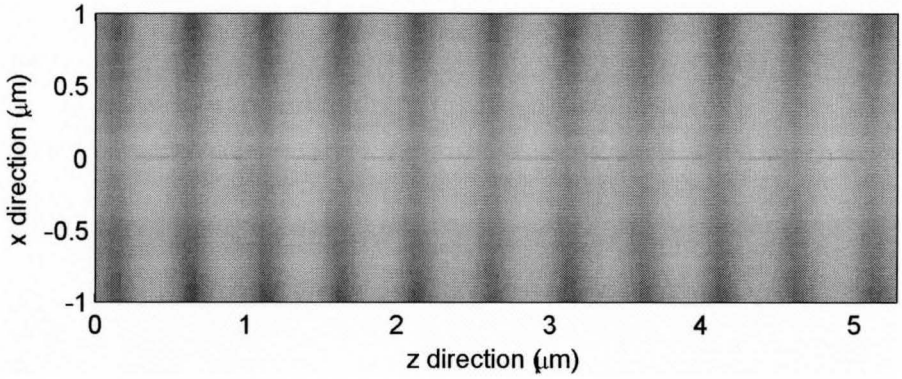

(a)

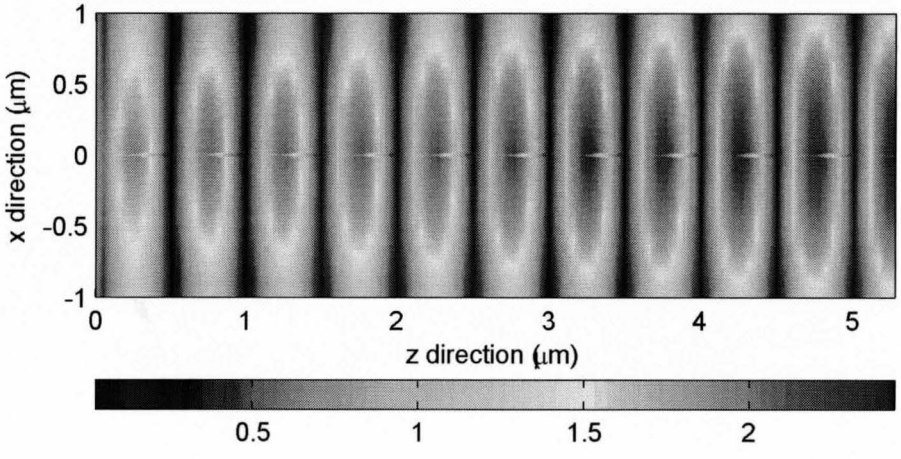

(b)

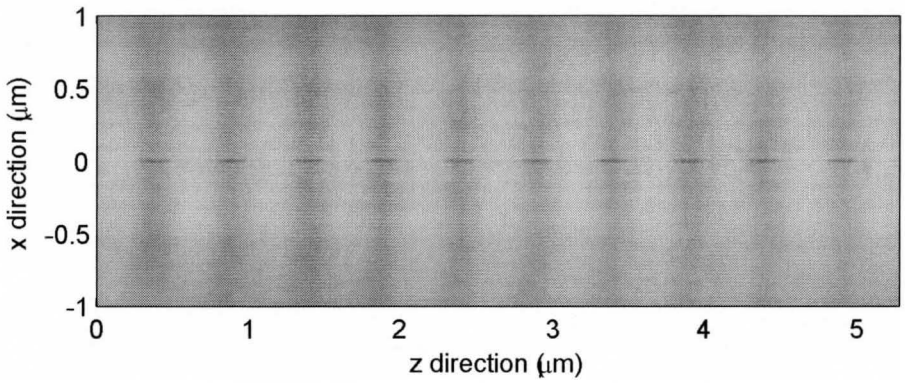

(c)

Figure 8.12 Field distributions through the first ten periods for the grating with ridge height $h = 10$ nm and $N = 160$ periods. (a) $\lambda = 1.53$ μm; (b) $\lambda = 1.545$ μm; (c) $\lambda = 1.57$ μm. The color bar is the same for all the plots.

8.4 Summary

As the application of the high-order BiBPM developed in the previous chapter, we propose an iteration method for the design of Bragg gratings with strong index corrugations. The conventional design method leads to a blue shift of peak wavelength from the desired Bragg wavelength. The proposed iteration method can achieve the desired peak wavelength in a few iterations even for deep Bragg gratings.

The high-order BiBPM is also applied to the analysis of Bragg gratings for long-range surface plasmon polaritons. Numerical results have demonstrated the potential of our method in the analysis and design of surface plasmonic structures.

Chapter 9
Conclusions and Suggestions for Future Research

9.1 Summary of Contributions

The objective of this thesis was to develop accurate and efficient modeling techniques in frequency domain for the simulation of light propagation in various optical waveguides. All the proposed numerical approaches have been used primarily for the analysis of high index contrast waveguides with fine feature sizes. The improvement in accuracy and efficiency of these approaches has been clearly demonstrated by simulating a number of microstructured waveguides. At last, Bragg gratings on high index contrast and plasmonic waveguides are designed by the newly developed propagation algorithms.

The major contributions of this thesis are summarized as follows and corresponding publications can be found in Appendix D.

1. The vectorial fourth-order finite-difference scheme is incorporated into an ultra wide-angle beam propagation method (BPM) based on Padé series expansion (P.6 and P.9) A comprehensive study for the accuracy of various finite-difference (FD) formulas in literature for the wide-angle beam propagation method is presented. It is demonstrated that the new high-order FD wide-angle BPM is highly accurate for efficient simulation of wide-angle field propagation and is superior to the

other FD schemes in the case of high index contrast and/or ultra wide-angle propagation.

2. A highly accurate reflective scheme is developed for analysis of two-dimensional waveguide discontinuities (P.5). It is demonstrated that the new method achieves significantly higher accuracy/computation cost ratio in comparison with the conventional finite-difference method. Further, the advantage of the new method is more pronounced in the case of high index contrast structures with small feature sizes.

3. Accurate rational approximations to the square root operators are crucial for the bi-directional beam propagation method in simulation of strongly reflective structures. An assessment and comparison of various commonly used rational approximations is performed for both TE and TM waves (P.1). The range of validity and level of accuracy for the different approximations are studied by investigating the structures with varying reflection intensities. Guidelines for accurately modeling of evanescent and propagating modes are provided.

4. A vectorial fourth-order finite-difference formula is applied to the bi-directional beam propagation method based on scattering operators (P.4). The method is shown to provide significant improvement in accuracy and efficiency, especially for waveguide structures of high index contrast.

5. An efficient iteration method is proposed for the design of Bragg gratings with strong index corrugations (P.3). In conjugation with the high-order BiBPM, the

iteration method is able to efficiently design deep Bragg gratings with a desired peak wavelength.

6. The high-order BiBPM has been applied to the analysis of Bragg gratings based on long-range surface plasmon polaritons (P.7). The good agreement with other methods validated the effectiveness of our method in the simulation and design of surface plasmonic waveguides.

9.2 Suggestions for Future Research

Although the usefulness of modeling techniques for wave propagation presented in this thesis has been clearly demonstrated, there still remain some topics worth further study. Accordingly, I suggest the following recommendations for future work:

1. **High-order BiBPM for 3D structures.** In this thesis, we developed high-order propagation algorithms mainly for the 2D structures. Since 3D waveguides are the fundamental building blocks of integrated photonic circuits, the extension of high-order finite-difference methods to 3D propagation algorithms are highly desirable for efficient simulations. However, such extension is never straightforward because the high-order finite-difference formulas are derived by making use of the 1D Helmholtz equation. One possible solution is to utilize the alternating-direction implicit method to split the propagation into two steps, such that the transverse directions can be treated separately by the high-order formulations.

2. **Slanted wall propagation in high index contrast structures.** Wide-angle BPM has been developed to deal with optical waveguides with slanted dielectric interfaces. In this method, the structure is discretized along the propagation direction by the "stair-case" approximation. As a result, the discretized structure deviates from its original configuration and artificial numerical loss is generated at each transition plane. This spurious effect is generally tolerable for low index contrast structures, but can become severe for high index contrast structures as to render it useless [108]. Although some efforts have been paid to address this problem by employing coordinate transformations, they are limited to structures with sufficient regularity. Accordingly, it is necessary to develop a general wide-angle propagation algorithm for accurate modeling of high index contrast structures with irregular dielectric interfaces along propagation direction.

Bibliography

[1] S. E. Miller, "Integrated optics: An introduction," *Bell Sys. Tech. Journal*, pp.2059-2069, Sept. 1969.

[2] E. A. J. Marcatili, "Dielectric rectangular waveguide and directional coupler for integrated optics," *Bell Sys. Tech. Journal*, pp.2071-2102, Sept. 1969.

[3] Kumar, D. F. Clark, and B. Culshaw, "Explanation of errors inherent in effective-index method for analyzing rectangular-core waveguides," *Opt. Lett.*, vol.13, pp.1129-1131, 1988.

[4] P. C. Kendal, P. W. A. Mcllroy, and M. S. Stern, "Spectral index method for rib waveguide analysis," *Electron. Lett.*, vol.25, pp.107-108, 1989.

[5] P. W. A. Mcllroy, M. S. Stern, and P. C. Kendall, "Spectral index method for polarized modes in semiconductor rib waveguides," *IEEE J. Lightwave Technol.*, vol.8, pp.113-117, 1990.

[6] W. P. Huang, H. A. Haus, and H. N. Yoon, "Analysis of buried channel waveguides and couplers: scalar solution and polarization correction," *IEEE J. Lightwave Technol.*, vol.8, pp.642-648, May 1990.

[7] W. P. Huang and H. A. Haus, "A simple variational approach to optical rib waveguides," *IEEE J. Lightwave Technol.*, vol.9, pp.56-61, 1991.

[8] M. S. Stern, "Semivectorial polarized finite difference method for optical waveguides with arbitrary index profiles," *IEE Proc.-J*, vol.135, no.5, pp.56-63, 1988.

[9] C. L. Xu, W. P. Huang, M. S. Stern and S. K. Chaudhuri, "Full-vectorial mode calculations by finite difference method," *IEE Proc.-J*, vol.141, no.5, pp.281-286, 1994.

[10] H. A. Haus, W. P. Huang, S. Kawakami, and N. A. Whitaker, "Coupled-mode theory of optical waveguides," *J. Lightwave. Technol.*, vol. LT-5, no.1, pp. 16–23, Jan. 1987.

[11] W.-P. Huang, "Coupled-mode theory for optical waveguides: An overview," *J. Opt. Soc. Amer. A, Opt. Image Sci.*, vol. 11, no. 3, pp. 963–983,Mar. 1994.

[12] T. E. Rozzi, "Rigorous analysis of the step discontinuity in a planar dielectric waveguide," *IEEE Trans. Microw. Theory Technol.*, vol.26, pp.738-746, Oct. 1978.

[13] M. D. Feit and J. A. Fleck, Jr., "Light propagation in graded-index optical fibers," *Applied Optics*, vol.17, no.24, pp.3990-3998, 1978.

[14] W. P. Huang, C. L. Xu, S. T. Cu, and S. K. Chaudhuri, "A finite difference vector beam propagation method: analysis and assessment," *IEEE J. Lightwave Technol.*, vol.10, pp.295-305, Mar. 1992.

[15] J. Gerdes and R. Pregla, "Beam-propagation algorithm based on the method of lines," *J. Opt. Soc. Amer. B*, vol. 8, pp. 389–394, Feb. 1991.

[16] U. Rogge and P. Pregla, "Method of lines for the analysis of dielectric waveguides," *J. Lightwave. Technol.*, vol. 11, no.12, pp. 2015–2020, Dec. 1993.

[17] K. S. Yee, "Numerical solution of initial boundary value problems involving Maxwell's equations in isotropic media," *IEEE Trans. Antennas Propagat.*, vol.14, pp.302-307, 1966.

[18] S. T. Chu and S. K. Chaudhuri, "A finite-difference time-domain method for the design and analysis of guided-wave optical structures," *IEEE J. Lightwave Technol.*, vol.7, pp.2033-2038, Dec. 1989.

[19] W. P. Huang, S. T. Chu, A. Goss, and. S. K. Chaudhuri, "A scalar finite-difference time-domain approach to guided wave optics," *IEEE Photonics Technol. Lett.*, vol.3, pp.524-526, June 1991.

[20] W. P. Huang, S. T. Chu, and S. K. Chaudhuri, "A semivectorial finite-difference time domain method," *IEEE Photonics Technol. Lett.*, vol.3, no.9, pp.803-806, Sept. 1991.

[21] J. Yamauchi, M. Mita, S. Aoki, and H. Nakano, "Analysis of antireflection coatings using the FDTD method with the PML absorbing boundary condition," *IEEE Photon. Technol. Lett.*, vol.8, pp.239-241, Feb. 1996.

[22] D.Yevick and B. Hermansson, "Efficient beam propagation techniques," *J. Quantum Electron.*, vol. 26, pp. 109–112, 1990.

[23] Y. Chung and N. Dagli, "An assessment of finite difference beam propagation method," *J. Quantum Electron.*, vol. 26, pp. 1335–1339, 1990.

[24] R. Scarmozzino and R. M. Osgood Jr., "Comparison of finite-difference and Fourier-transform solutions of the parabolic wave equation with emphasis on integrated-optics applications," *J. Opt. Soc. Amer. A*, vol. 8, pp. 724, 1991.

[25] G. R. Hadley, "Transparent boundary condition for the beam propagation method," *Opt. Lett.*, vol. 28, p. 624, 1992.

[26] W. P. Huang, C. L. Xu, W. Lui, and K. Yokoyama, "The perfectly matched layer (PML) boundary condition for the beam propagation method," *Photon. Technol. Lett.*, vol. 8, pp. 649–651, 1996.

[27] R. Clauberg and P. Von Allmen, "Vectorial beam propagation method for integrated optics," *Electron. Lett.*, vol. 27, p. 654, 1991.

[28] W. P. Huang and C. L. Xu, "Simulation of three-dimensional optical waveguides by a full-vector beam propagation method," *J. Quantum Electron.*, vol. 29, p. 2639, 1993.

[29] D. Yevick and M. Glasner, "Analysis of forward wide-angle light propagation in semiconductor ribwaveguides and integrated-optic structures," *Electron. Lett.*, vol. 25, pp. 1611–1613, 1989.

[30] G. R. Hadley, "Wide-angle beam propagation using Pade approximant operators," *Opt. Lett.*, vol. 17, p. 1426, 1992.

[31] G. R. Hadley, "Multistep method for wide-angle beam propagation," *Opt. Lett.*, vol. 17, p. 1743, 1992.

[32] Y. Chiou and H. Chang, "Analysis of optical waveguide discontinuities using the Pade approximants," *Photon. Technol. Lett.*, vol. 9, pp. 964–966, 1997.

[33] P. Kaczmarski and P. E. Lagasse, "Bidirectional beam propagation method," *Electron. Lett.*, vol. 24, pp. 675–676, 1988.

[34] H. Rao, R. Scarmozzino, and R. M. Osgood Jr., "A bidirectional beam propagation method for multiple dielectric interfaces," *Photon. Technol. Lett.*, vol. 11, pp. 830–832, 1999.

[35] H. El-Refaei, D. Yevick, and I. Betty, "Stable and noniterative bidirectional beam propagation method," *IEEE Photon. Technol. Lett.*, vol. 12, pp. 389–391, Apr. 2000.

[36] H. Rao, M. J. Steal, R. Scarmozzino, and R. M. Osgood, "Complex propagator for evanescent waves in bidirectional beam propagation method," *J. Lightwave Technol.*, vol. 18, pp. 1155–1160, Aug. 2000.

[37] P. L. Ho and Y. Y. Lu, "A stable bidirectional propagation method based on scattering operators," *IEEE Photon. Technol. Lett.*, vol. 13, no. 12, pp. 1316-1318, Dec. 2001.

[38] P. L. Ho and Y. Y. Lu, "A bidirectional beam propagation method for periodic waveguides," *IEEE Photon. Technol. Lett.*, Vol. 14, No. 3, pp. 325-327, 2002.

[39] Y. Y. Lu and S. H. Wei, "A new iterative bidirectional beam propagation method," *IEEE Photon. Technol. Lett.*, vol. 14, no. 11, pp. 1533–1535, Nov. 2002.

[40] Lijun Yuan and Y.Y. Lu, "An efficient bidirectional beam propagation method based on Dirichlet-to-Neumann maps," *IEEE Photon. Technol. Lett.*, vol. 18, no. 18, pp. 1967–1969, Sept. 2006.

[41] N. N. Feng, C. L. Xu, W. P. Huang and D. G. Fang, "A new preconditioner based on paraxial approximation for stable and efficient reflective beam propagation method," *J. Lightwave Technol.*, vol. 21, no. 9, pp. 1996-2001, 2003.

[42] B. M. A. Rahman, F. A. Fernandez, and J. B. Davies, "Review of finite element methods for microwave and optical waveguides," *P. IEEE*, vol. 79, pp. 1442-1448, 1991.

[43] Koshiba M., K. Hayata, and M. Suzuki, "Finite-element formulation in terms of the electric field vector for electromagnetic waveguide problems," *IEEE Trans. Microwave Theory Tech.*, vol. MTT-33, 900-905, Oct. 1985.

[44] R. D. Richtmeyer and K. W. Morton, *Difference Methods for Initial Value Problems*, 2nd ed. New York: Interscience-Wiley.

[45] C. Manolatou, S. G. Johnson, S. Fan. P. R. Villeneuve, H. A. Haus, and J. D. Joannopoulos, "High-density integrated optics," *IEEE J. Lightwave Technol.*, vol.17, pp.1682-1692, Sept. 1999.

[46] C. Manolatou and H. A. Haus, *Passive Components for Dense Optical Integration*, Kluwer Academic Publishers, Norwell, MA, 2002.

[47] H. A. Haus, "High density optical integration," IEEE/LEOS, Nov. 2002, WC1 (Tutorial), pp.389-390.

[48] T. Tsuchizawa, K. Yamada, H. Fukuda, T. Watanabe, J. Takahashi, M. Takahashi, T. Shoji, E. Tamechika, S. Itabashi, and H. Morita, "Microphotonics devices based on silicon microfabrication technology," *IEEE J. Selected Topics in Quantum Electron.*, vol. 11, no.1, pp. 232-240, 2005.

[49] C. Vassallo, "Improvement of finite difference methods for step-index optical waveguides," *Inst. Elect. Eng. Proc.-J.*, vol.139, pp. 137-142, 1992.

[50] Y. –C. Chiang, Y. –P. Chiou, H. –C. Chang, "Improved full-vectorial finite-difference mode slover for optical waveguides with step-index profiles," *J. Lightwave Technol.*, vol.20, pp. 1609-1618, Aug. 2002.

[51] G. R. Hadley, "High-accuracy finite-difference equations for dielectric waveguide analysis I: Uniform regions and dielectric interfaces," *J. Lightwave Technol.*, vol.20, pp. 1210-1218, Jul. 2002.

[52] G. R. Hadley, "High-accuracy finite-difference equations for dielectric waveguide analysis II: Dielectric corners," *J. Lightwave Technol.*, vol.20, pp. 1219-1231, Jul. 2002.

[53] J. Yamauchi, M. Sekiguchi, O. Uchiyama, J. Shibayama, and H. Nakano, "Modified finite-difference formula for the analysis of semivectorial modes in step-index optical waveguides," *IEEE Photon. Technol. Lett.*, vol. 9, no. 7, pp. 961–963, 1997.

[54] A. R. Mitchell, *Computation methods in partial differential equations* (Wiley, New York, 1969), Chap. 2.

[55] L. Sun and G. L. Yip, "Modified finite-difference beam-propagation method based on Douglas scheme," *Opt. Lett.*, vol. 18, no. 15, pp. 1229-1231, 1993.

[56] J. Yamauchi, J. Shibayama, and H. Nakano, "Modified finite-difference beam propagation method based on the generalized Douglas scheme for variable coefficients," IEEE Photon. Technol. Lett., vol. 7, pp. 661-663, June 1995.

[57] G. R. Hadley, "Low-truncation-error finite difference equations for photonics simulation I: Beam propagation," *J. Lightwave Technol.*, vol. 16, pp. 134-141, 1998.

[58] Y. –P. Chiou, Y. –C. Chiang, H. –C. Chang, "Improved three-point formulas considering the interface conditions in the finite-difference analysis of step-index optical devices," *J. Lightwave Technol.*, vol.18, pp. 243-251, Feb. 2000.

[59] D. Marcuse, *Theory of dielectric optical waveguides* (Academic press, San Diego, CA, 1991), Chap. 1.

[60] W. L. Barnes, A. Dereux, and T. W. Ebbesen, "Surface plasmon sub-wavelength optics," *Nature*, vol. 424, no. 6950, pp. 824–830, Aug. 2003.

[61] I. I. Smolyaninov, D. L. Mazzoni, and C. C. Davis, "Imaging of surface plasmon scattering by lithographically created individual surface defects," *Phys. Rev. Lett.*, vol. 77, no. 18, pp. 3877–3880, Oct. 1996.

[62] S. I. Bozhevolnyi and F. A. Pudonin, "Two-dimensional micro-optics of surface plasmons," *Phys. Rev. Lett.*, vol. 78, no. 14, pp. 2823–2826, Apr. 1997.

[63] H. Ditlbacher, J. R. Krenn, G. Schider, A. Leitner, and F. R. Aussenegg, "Two-dimensional optics with surface plasmon polaritons," *Appl. Phys. Lett.*, vol. 81, no. 10, pp. 1762–1764, Sep. 2002.

[64] S. I. Bozhevolnyi, J. Erland, K. Leosson, P. M. W. Skovgaard, and J. M. Hvam, "Waveguiding in surface plasmon polariton band gap structures," *Phys. Rev. Lett.*, vol. 86, no. 14, pp. 3008–3011, Apr. 2001.

[65] D. Sarid, "Long-range surface-plasma waves on very thin metal films," *Phys. Rev. Lett.*, vol. 47, no. 26, pp. 1927–1930, Dec. 1981.

[66] P. Berini, "Plasmon-polariton waves guided by thin lossy metal films of finite width: Bound modes of symmetric structures," *Phys. Rev. B, Condens. Matter*, vol. 61, no. 15, pp. 10484–10503, Apr. 2000.

[67] L. H. Spiekman, Y. S. Oei, E. G. Metaal, F. H. Groen, P. Demeester, and M. K. Smit, "Ultrasmall waveguide bends: The corner mirrors of the future?," *Inst. Elect. Eng. Proc. Optoelectron.*, vol. 142, pp. 61–65, 1995.

[68] M. Heiblum and J. H. Harris, "Analysis of curved optical waveguides by conformal transformation," *IEEE J. Quantum Electron.*, vol.11, no. 2, pp.75-83, 1975.

[69] M. Rivera, "A finite difference BPM analysis of bent dielectric waveguide," *J. Lightwave Technol.*, vol. 13, pp. 233–238, Feb. 1995.

[70] N.-N. Feng, G.-R. Zhou, C. Xu and W.-P. Huang, "Computation of full-vector modes for bending waveguide using cylindrical perfectly matched layers," *IEEE J. Lightwave Technol.*, vol.20, pp.1976-1980, Nov. 2002.

[71] J. J. Burke and G. I. Stegeman, "Surface-polariton-like waves guided by thin, lossy metal films," *Phys. Rev. B,* vol. 33, no. 8, pp. 5186–5201, Apr. 1986.

[72] A. Jennings, Matrix computation for engineers and scientists. New York: Wiley, 1977.

[73] M. Koshiba, Y. Tsuji, "A wide-angle finite-element beam propagation method," *IEEE Photon. Technol. Lett.* vol. 8, pp. 1208-1210, 1996.

[74] J. Yamauchi, J. Shibayama, and H. Nakano, "Wide-angle propagating beam analysis based on the generalized Douglas scheme for variable coefficients," *Opt. Lett.*, vol. 20, no. 1, pp. 7-9, 1995.

[75] J. Yamauchi, J. Shibayama, M. Sekiguchi, and H. Nakano, "Improved multistep method for wide-angle beam propagation," *IEEE Photon. Technol. Lett.*, vol. 8, pp. 1361-1363, Oct. 1996.

[76] C. Vassallo, "Limitations of the wide-angle beam propagation method in nonuniform systems," *J. Opt. Soc. Amer.* vol. 13, 761-770, 1996.

[77] C. Vassallo, "Interest of improved three-point formulas for finite-difference modeling of optical devices," *J. Opt. Soc. Amer.* vol. 14, pp. 3273-3284, 1997.

[78] M. D. Collins, "Benchmark calculations for higher-order parabolic equations," *J. Acoust. Soc. Amer.*, vol. 87, pp. 1535-1538, 1990.

[79] M. D. Collins, "A split-step Padé solution for the parabolic equation method," *J. Acoust. Soc. Amer.*, vol. 93, pp. 1736-1742, 1993.

[80] D. Yevick, "The application of complex Padé approximants to vector field propagation," *IEEE Photon. Technol. Lett.*, vol. 12, pp. 1636-1638, Dec. 2000.

[81] Y. Y. Lu and P. L. Ho, "Beam propagation method using a [(p-1)/p] Padé approximant of the propagator," *Opt. Lett.*, vol. 27, no. 9, pp. 683-685, 2002.

[82] A. Bamberger, B. Engquist, L. Halpern, and P. Joly, "Higher order paraxial wave equation approximations in heterogeneous media," *SIAM J. Appl. Math.*, vol. 48, pp. 129-154, 1988.

[83] Y. –P. Chiou and H. –C. Chang, "Efficient beam-propagation method based on Padé approximants in the propagation direction," *Opt. Lett.*, vol. 22, no. 13, pp. 949-951, 1997.

[84] C. Vassallo, "Reflectivity of multidielectric coatings deposited on the end facet of a weakly guiding dielectric slab waveguide," *J. Opt. Soc. Amer. A*, vol. 5, no. 11, pp. 1918-1928, 1988.

[85] M. Reed, T. M. Benson, P. C. Kendall, and P. Sewell, "Antireflection-coated angled facet design," *IEE Proc. –Optoelectron.*, vol. 143, no. 4, pp. 214-220, 1996.

[86] H. Derudder, F. Olyslager, D. De Zutter, and S. Van den Berghe, "Efficient mode-matching analysis of discontinuities in finite planar substrates using perfectly matched layers," *IEEE Trans. Antennas Propag.*, vol. 49, no. 2, pp. 185-195, Feb. 2001.

[87] C. Yu and D. Yevick, "Application of the bidirectional parabolic equation method to optical waveguide facets," *J. Opt. Soc. Amer. A*, vol. 14, no. 7, pp. 1448-1450, 1997.

[88] H. El-Refaei, I. Betty and D. Yevick, "The application of complex Padé approximants to reflection at optical waveguide facets," *IEEE Photon. Technol. Lett.*, vol. 12, no. 2, pp. 158-160, 2000.

[89] S. H. Wei and Y. Y. Lu, "Application of Bi-CGSTAB to waveguide discontinuity problems," *IEEE Photon. Technol. Lett.*, vol. 14, no. 5, pp. 645-647, 2002.

[90] Y. Y. Lu, "A complex coefficient rational approximation of $\sqrt{1+x}$," *Applied Numerical Mathematics*, vol. 27, no. 2, pp. 141-154, 1998.

[91] H. Van der Vorst, "Bi-CGSTAB: A fast and smoothly converging variant of Bi-CG for the solution of nonsymmetric linear systems," *SIAM J. Sci. Statist. Comput.*, vol. 13, pp. 631-644, 1992.

[92] W. Streifer, D.R. Scifres, and R.D. Burnham, "Coupled wave analysis of DFB and DBR lasers," *IEEE J. Quantum Electron.*, vol. QE-13, no. 4, pp. 134-141, 1977.

[93] A. M. Shams-Zadeh-Amiri, J. Hong, X. Li, and W. P. Huang, "Second and higher resonat gratings with gain or loss—Part I: Green's function analysis," *IEEE J. Quantum Electron.*, vol. 36, no. 12, pp. 1421–1430, Dec. 2000.

[94] S. M. Norton, T. Erdogan, and G. M. Morris, "Coupled-mode theory of resonant-grating filters," *J. Opt. Soc. Amer. A*, vol. 14, no. 3, pp. 629–639, 1997.

[95] R. Scarmozzino, A. Gopinath, R Pregla and S. Helfert, "Numerical techniques for modeling guided-wave photonic devices," *IEEE Journal of Selected Topics in Quantum Electronics*, vol. 6, pp. 150-162, 2000.

[96] Y. Y. Lu, "Some techniques for computing wave propagation in optical waveguides," *Communications in Computational Physics,* Vol. 1, No. 6, pp.1056-1075, Dec. 2006.

[97] F. A. Milinazzo, C. A. Zala, and G. H. Brooke, "Rational square-root approximations for parabolic equation algorithms," *J. Acoust. Soc. Amer.*, vol. 101, no. 2, pp. 760-766, 1997.

[98] S. S. A. Obayya, "Novel finite element analysis of optical waveguide discontinuity problems," *J. Lightwave Technol.*, vol. 22, no. 5, pp. 1420-1425, 2004.

[99] S. Blair and J. Goeckeritz, "Effect of vertical mode matching on defect resonances in one-dimensional photonic crystal slabs," *J. Lightwave Technol.*, vol.24, no. 3, pp. 1456-1461, 2006.

[100] A. Locatelli, D. Modotto, C. De Angelis, F. M. Pigozzo, and A. D. Capobianco, "Nonlinear bidirectional beam propagation method based on scattering operators for periodic microstructured waveguides," *J. Opt. Soc. Amer., B, Opt. Phys.*, vol. 20, no. 8, pp. 1724–1731, Aug. 2003.

[101] J. Ctyroky, "Analysis of a deep waveguide Bragg gratings," *Opt. Quant. Electron.*, vol. 30, pp. 343-358, 1998.

[102] H. Raether, *Surface Plasmons*, Berlin, Germany: Springer-Verlag, 1988.

[103] R. H. Ritchie, "Plasma losses by fast electrons in thin films," *Phys. Rev.* 106, 874-881, 1957.

[104] J. C. Quail, J. G. Rabo, and H. J. Simon, "Long-range surface-plasmon modes in silver and aluminum films,", *Opt. Lett.* vol. 8, 377-379, 1983.

[105] A. Boltasseva, S. I. Bozhevolnyi, T. Nikolajsen, and K. Leosson, "Compact Bragg gratings for long-range surface plasmon polaritons," *IEEE J. Lightw. Technol.* vol. 24, no. 2, 912-918, 2006.

[106] S. Charbonneau, R. Charbonneau, N. Lahoud, G. Mattiussi, and P. Berini, "Demonstration of Bragg gratings based on long-ranging surface plasmon polaritons waveguides," *Opt. Express*, vol. 13, no. 12, 4674-4682, 2005.

[107] T. Sondergaard, S. I. Bozhevolnyi, and A. Boltasseva, "Theoretical analysis of ridge gratings for long-range surface plasmon polaritons," *Phys. Rev. B*, vol. 73, 45320, 2006.

[108] G. R. Hadley, "Slanted-wall beam propagation," *IEEE J. Lightw. Technol.* vol. 25, no. 9, pp. 2367-2375, Sept. 2007.

Appendix A

Coefficients Used in Finite-Difference Formulas

The coefficients used in Eq.(3.28) are as follows:

$$f_0 = \theta\left(1+\frac{q^2\eta}{2}+\frac{q^4\eta^2}{24}\right)+O(h^6) \tag{A.1}$$

$$f_1 = \theta\left(p+\frac{pq^2\eta}{2}+\frac{pq^4\eta^2}{24}\right)+q+\frac{q^3\eta}{6}+\frac{q^5\eta^2}{120}+O(h^6) \tag{A.2}$$

$$f_2 = \theta\left(\frac{p^2}{2}+\frac{q^2}{2}+\frac{p^2q^2\eta}{4}+\frac{q^4\eta}{12}\right)+pq+\frac{pq^3\eta}{6}+O(h^6) \tag{A.3}$$

$$f_3 = \theta\left(\frac{p^3}{6}+\frac{pq^2}{2}+\frac{p^3q^2\eta}{12}+\frac{pq^4\eta}{12}\right)+\frac{p^2q}{2}+\frac{q^3}{6}+\frac{p^2q^3\eta}{12}+\frac{q^5\eta}{60}+O(h^6) \tag{A.4}$$

$$f_4 = \theta\left(\frac{p^4}{24}+\frac{p^2q^2}{4}+\frac{q^4}{24}\right)+\frac{p^3q}{6}+\frac{pq^3}{6}+O(h^6) \tag{A.5}$$

$$f_5 = \theta\left(\frac{p^5}{120}+\frac{p^3q^2}{12}+\frac{pq^4}{24}\right)+\frac{p^4q}{24}+\frac{p^2q^3}{12}+\frac{q^5}{120}+O(h^6) \tag{A.6}$$

The coefficients used in Eq.(3.29) can be obtained by replacing p, q and n_{i+1} with $-c$, $-d$ and n_{i-1}, respectively.

The coefficients used in Eq.(3.32) are expressed as

$$g_1 = \frac{e_3f_1 - f_3e_1}{e_2f_1 - f_2e_1} \tag{A.7}$$

$$g_2 = \frac{e_4 f_1 - f_4 e_1}{e_2 f_1 - f_2 e_1} \tag{A.8}$$

The coefficients b_j's used in Eq.(3.34) are given by

$$b_0 = \theta\left(1 + \frac{q^2\eta}{2}\right) + O(h^4) \tag{A.9}$$

$$b_1 = \theta\left(p + \frac{pq^2\eta}{2}\right) + q + \frac{q^3\eta}{6} + O(h^4) \tag{A.10}$$

$$b_2 = \theta\left(\frac{p^2}{2} + \frac{q^2}{2}\right) + pq + O(h^4) \tag{A.11}$$

$$b_3 = \theta\left(\frac{p^3}{6} + \frac{pq^2}{2}\right) + \frac{p^2 q}{2} + \frac{q^3}{6} + O(h^4) \tag{A.12}$$

The coefficients a_j's used in Eq.(3.34) can be obtained by replacing p, q and n_{i+1} with $-c$, $-d$ and n_{i-1}, respectively.

Appendix B

Finite-Difference Form of One-Way Wave Equations

The coefficients for the finite-difference form of paraxial and wide-angle wave equations are listed here for reference.

B.1 Paraxial Wave Equation

The finite-difference form of the paraxial wave equation is

$$c_{i-1}^{l+1}\Psi_{i-1}^{l+1}+c_{i}^{l+1}\Psi_{i}^{l+1}+c_{i+1}^{l+1}\Psi_{i+1}^{l+1}=c_{i-1}^{l}\Psi_{i-1}^{l}+c_{i}^{l}\Psi_{i}^{l}+c_{i+1}^{l}\Psi_{i+1}^{l} \tag{B.1}$$

where

$$c_{i\text{-}1}^{l+1}=-\frac{\Delta z t_{-}}{2}+\left[2jk_0n_0-\frac{k_0^2\left(n_{i-1}^2-n_0^2\right)\Delta z}{2}\right]\left(g_1s_{-}+g_2t_{-}\right) \tag{B.2}$$

$$c_{i}^{l+1}=-\frac{\Delta z t_{0}}{2}+\left[2jk_0n_0-\frac{k_0^2\left(n_{i}^2-n_0^2\right)\Delta z}{2}\right]\left(1+g_1s_0+g_2t_0\right) \tag{B.3}$$

$$c_{i+1}^{l+1}=-\frac{\Delta z t_{+}}{2}+\left[2jk_0n_0-\frac{k_0^2\left(n_{i+1}^2-n_0^2\right)\Delta z}{2}\right]\left(g_1s_{+}+g_2t_{+}\right) \tag{B.4}$$

$$c_{i\text{-}1}^{l}=\frac{\Delta z t_{-}}{2}+\left[2jk_0n_0+\frac{k_0^2\left(n_{i-1}^2-n_0^2\right)\Delta z}{2}\right]\left(g_1s_{-}+g_2t_{-}\right) \tag{B.5}$$

$$c_i^l = \frac{\Delta z t_0}{2} + \left[2jk_0 n_0 + \frac{k_0^2 \left(n_i^2 - n_0^2 \right) \Delta z}{2} \right] \left(1 + g_1 s_0 + g_2 t_0 \right) \tag{B.6}$$

$$c_{i+1}^l = \frac{\Delta z t_+}{2} + \left[2jk_0 n_0 + \frac{k_0^2 \left(n_{i+1}^2 - n_0^2 \right) \Delta z}{2} \right] \left(g_1 s_+ + g_2 t_+ \right) \tag{B.7}$$

B.2 Wide-Angle Wave Equation

The finite-difference form for the k^{th} step of wide-angle wave equation is

$$\begin{aligned} & c_{i-1}^{l+k/m} \Psi_{i-1}^{l+k/m} + c_i^{l+k/m} \Psi_i^{l+k/m} + c_{i+1}^{l+k/m} \Psi_{i+1}^{l+k/m} \\ & = c_{i-1}^{l+(k-1)/m} \Psi_{i-1}^{l+(k-1)/m} + c_i^{l+(k-1)/m} \Psi_i^{l+(k-1)/m} + c_{i+1}^{l+(k-1)/m} \Psi_{i+1}^{l+(k-1)/m} \end{aligned} \tag{B.8}$$

where

$$c_{i-1}^{l+k/m} = \frac{\left(b_{k,m} + a_{k,m} jk_0 n_0 \Delta z/2 \right) t_-}{k_0^2 n_0^2} + \left[1 + \frac{\left(b_{k,m} + a_{k,m} jk_0 n_0 \Delta z/2 \right) \left(n_{i-1}^2 - n_0^2 \right)}{n_0^2} \right] \left(g_1 s_- + g_2 t_- \right) \tag{B.9}$$

$$c_i^{l+k/m} = \frac{\left(b_{k,m} + a_{k,m} jk_0 n_0 \Delta z/2 \right) t_0}{k_0^2 n_0^2} + \left[1 + \frac{\left(b_{k,m} + a_{k,m} jk_0 n_0 \Delta z/2 \right) \left(n_i^2 - n_0^2 \right)}{n_0^2} \right] \left(1 + g_1 s_0 + g_2 t_0 \right) \tag{B.10}$$

$$c_{i+1}^{l+k/m} = \frac{\left(b_{k,m} + a_{k,m} jk_0 n_0 \Delta z/2 \right) t_+}{k_0^2 n_0^2} + \left[1 + \frac{\left(b_{k,m} + a_{k,m} jk_0 n_0 \Delta z/2 \right) \left(n_{i+1}^2 - n_0^2 \right)}{n_0^2} \right] \left(g_1 s_+ + g_2 t_+ \right) \tag{B.11}$$

$$c_{i-1}^{l+(k-1)/m} = \frac{\left(b_{k,m} - a_{k,m} jk_0 n_0 \Delta z/2 \right) t_-}{k_0^2 n_0^2} + \left[1 + \frac{\left(b_{k,m} - a_{k,m} jk_0 n_0 \Delta z/2 \right) \left(n_{i-1}^2 - n_0^2 \right)}{n_0^2} \right] \left(g_1 s_- + g_2 t_- \right) \tag{B.12}$$

$$c_i^{l+(k-1)/m} = \frac{\left(b_{k,m} - a_{k,m} jk_0 n_0 \Delta z/2 \right) t_0}{k_0^2 n_0^2} + \left[1 + \frac{\left(b_{k,m} - a_{k,m} jk_0 n_0 \Delta z/2 \right) \left(n_i^2 - n_0^2 \right)}{n_0^2} \right] \left(1 + g_1 s_0 + g_2 t_0 \right) \tag{B.13}$$

$$c_{i+1}^{l+(k-1)/m} = \frac{\left(b_{k,m} - a_{k,m} jk_0 n_0 \Delta z/2 \right) t_+}{k_0^2 n_0^2} + \left[1 + \frac{\left(b_{k,m} - a_{k,m} jk_0 n_0 \Delta z/2 \right) \left(n_{i+1}^2 - n_0^2 \right)}{n_0^2} \right] \left(g_1 s_+ + g_2 t_+ \right) \tag{B.14}$$

Appendix C

Finite-Difference Form of Reflective Operator Scheme

The finite-difference expression for the reflective operator scheme is

$$c_{i-1}^{r}\Psi_{i-1}^{r}+c_{i}^{r}\Psi_{i}^{r}+c_{i+1}^{r}\Psi_{i+1}^{r}=c_{i-1}^{in}\Psi_{i-1}^{in}+c_{i}^{in}\Psi_{i}^{in}+c_{i+1}^{in}\Psi_{i+1}^{in} \tag{C.1}$$

where

$$c_{i\text{-}1}^{r}=\frac{e^{-i\alpha}b_{k,m}t_{-}}{k_0^2n_0^2}+\left[1-b_{k,m}+e^{-i\alpha}b_{k,m}+\frac{e^{-i\alpha}b_{k,m}\left(n_{i-1}^2-n_0^2\right)}{n_0^2}\right]\left(g_1s_{-}+g_2t_{-}\right) \tag{C.2}$$

$$c_{i}^{r}=\frac{e^{-i\alpha}b_{k,m}t_{0}}{k_0^2n_0^2}+\left[1-b_{k,m}+e^{-i\alpha}b_{k,m}+\frac{e^{-i\alpha}b_{k,m}\left(n_{i}^2-n_0^2\right)}{n_0^2}\right]\left(1+g_1s_0+g_2t_0\right) \tag{C.3}$$

$$c_{i+1}^{r}=\frac{e^{-i\alpha}b_{k,m}t_{+}}{k_0^2n_0^2}+\left[1-b_{k,m}+e^{-i\alpha}b_{k,m}+\frac{e^{-i\alpha}b_{k,m}\left(n_{i+1}^2-n_0^2\right)}{n_0^2}\right]\left(g_1s_{+}+g_2t_{+}\right) \tag{C.4}$$

$$c_{i\text{-}1}^{in}=\frac{e^{-i\alpha}c_{k,m}t_{-}}{k_0^2n_0^2}+\left[1-c_{k,m}+e^{-i\alpha}c_{k,m}+\frac{e^{-i\alpha}c_{k,m}\left(n_{i-1}^2-n_0^2\right)}{n_0^2}\right]\left(g_1s_{-}+g_2t_{-}\right) \tag{C.5}$$

$$c_{i}^{in}=\frac{e^{-i\alpha}c_{k,m}t_{0}}{k_0^2n_0^2}+\left[1-c_{k,m}+e^{-i\alpha}c_{k,m}+\frac{e^{-i\alpha}c_{k,m}\left(n_{i}^2-n_0^2\right)}{n_0^2}\right]\left(1+g_1s_0+g_2t_0\right) \tag{C.6}$$

$$c_{i+1}^{in}=\frac{e^{-i\alpha}c_{k,m}t_{+}}{k_0^2n_0^2}+\left[1-c_{k,m}+e^{-i\alpha}c_{k,m}+\frac{e^{-i\alpha}c_{k,m}\left(n_{i+1}^2-n_0^2\right)}{n_0^2}\right]\left(g_1s_{+}+g_2t_{+}\right) \tag{C.7}$$

Appendix D

List of Publications

D.1 International Journals

P.1. **Hua Zhang,** Jianwei Mu and Wei-Ping Huang, "Assessment of Rational Approximation for Square Root Operator in Bidirectional Beam Propagation Method," to appear in *IEEE/OSA J. Lightwave Technol.*, 2008.

P.2. Jianwei Mu, **Hua Zhang** and Wei-Ping Huang, "A Theoretical Investigation of Slot Waveguide Bragg Gratings," submitted to *IEEE J. of Quantum Electron.*, 2007

P.3. Jianwei Mu, **Hua Zhang** and Wei-Ping Huang, "Design of Waveguide Bragg Gratings with Strong Index Corrugations," submitted to *IEEE/OSA J. Lightwave Technol.*, 2007.

P.4. **Hua Zhang,** Jianwei Mu and Wei-Ping Huang, "Improved Bidirectional Beam Propagation Method by a Fourth-Order Finite-Difference Scheme," *IEEE/OSA J. Lightwave Technol.*, vol. 25, no. 9, pp. 2807-2813, September 2007.

P.5. **Hua Zhang**, Qingyi Guo and Wei-Ping Huang, "Analysis of Waveguide Discontinuities by a Fourth-Order Finite-Difference Reflective Scheme," *IEEE/OSA J. Lightwave Technol.*, vol. 25, no. 2, pp. 556-561, February 2007.

P.6. **Hua Zhang**, Wei-Ping Huang and Ning-Ning Feng, "Ultra-Wide-Angle Beam Propagation Method Based on High-Order Finite-Difference," *International Journal*

of Microwave and Optical Technology, vol. 1, no. 1, pp. 192-203, June 2006 (Invited paper)

D.2 International Conference Papers

P.7. **Hua Zhang**, Jianwei Mu and Wei-Ping Huang, "Analysis of Bragg Gratings for Long-Range Surface Plasmon Polaritons Using the Bidirectional Beam Propagation Method," *Optics & Photonics,SPIE,* paper number 6641-76, August 2007, San Diego, CA, USA.

P.8. Jianwei Mu, **Hua Zhang** and Wei-Ping Huang, "Analysis of a Long-Range Surface Plasmon Polariton Gratings Using One Dimensional Finite-Difference Mode Matching Method," *Optics & Photonics, SPIE* paper number 6642-42, August 2007, San Diego, CA, USA.

P.9. **Hua Zhang**, Ning-Ning Feng and Wei-Ping Huang, "Wide-Angle Beam Propagation Method Based on High-Accuracy Finite-Difference Formulas," *Integrated Photonics Research*, ITuA2, April 2006, Uncasville, CT, USA.